Multi-functional imaging of posterior eye with optical coherence tomography

Young-Joo Hong
Doctoral Program in Applied Physics

Submitted to the Graduate School of
Pure and Applied Sciences
in Partial Fullfillment of the Requirements
for the Degree of Doctor of Philosophy in
Engineering

at the
University of Tsukuba

Acknowledgement

I want to thank to all of the co-workers who assisted and supported my work during Ph.D. course. And it was indeed great chance for me to work with memebers of Computational Optics Group (COG) in the University of Tsukuba.

First, I would like to express my gratitude to Prof. Yoshiaki Yasuno for his devoted teaching and directing of research. And he is also good model as a researcher, he always try to learn and accept new things by himself, aggressively. His aggressiveness in research sometimes acted as pressure, but at the same time, it was good trigger to motivate me and reflect on myself. Actually, I owed many things to Prof. Yasuno indeed, while I am doing research work in COG.

I would like to thank Dr. Masahiro Miura for his advice and disscussion about ophthalmic disease and imaging and his devoted recruiting of patients. I would like to express my gratitude to the patients who volunteered to our OCT measurement. It was really thankfull that all of the patients were cooperative to the measurement. And it was possible to add values to this research owing to their cooperation. I would like to thank Dr. Shuichi Makita for his advice, support and fruitful discussion. Actually, he is one of mentors who guide me to ophthalmic vasculature imaging.

I would like to thank Prof. Masahide Itoh, who is an official advisor, for guiding me to focus on my research. Actually, it was possible to restart my Ph.D. course in the University of Tsukuba owing to his help and kind consideration. I would like to thank the committee members, Prof. Beop-min Kim and Prof. Toshiaki Hattori, for their discussion and advise to polish my dissertation.

I would like to thank all of COG members, ex-members and temporal members: Dr. Kazuhiro Kurokawa, Dr. Lian Duan, Arata Miyazawa, Kazuhiro Sasaki, Dr Masahiro Yamanari, Dr. Franck Jaillon, Dr Janne Lauri, Eun-Jung Min, and Jae-Hwi Lee. All of colleagues were enthusiastic and kind. Owing to work with them, I have learned many things and sometimes could be relieved from stress. Especially, I would like to express my gratitude to Myoeng-Jin Ju and Yiheng Lim for their excellent cooperation. I may be not able to finish my researh, if they were not with me. I would like to thank Lab. secretary Ran Nakamura and Chie Yoshinaga for their kind support of official administration.

I would like to thank reviewers who carefully review my papers to add more values. and I would like to thank researcher who shared discussion and gave question, sugestion and encouragement. Actually, they helped my research to be progressed into valuable way.

Finally, I would like to express special thanks to my family and friends.

Abstract of dissertation

Exudative macular diseases threaten vision ability of humans. When the disease progressed, they are frequently appear with abnormal choroidal neovascularization (CNV). For normal visual function, eye acquires nutrition and excretes metabolic end products through blood circulation. And retinal pigment epithelium (RPE) layer, located between retina and choroid, plays significant role in metabolism and regulation of the retina. Hence, abnormalities of the vasculature or RPE are important indicators of ocular malfunction.

Optical coherence tomography (OCT) is a noninvasive imaging modality which provides cross-sectional images at a micrometer scale. OCT has been successfully utilized in ophthalmic diagnosis owing to the optical biopsy images of anterior and posterior of eye, which was not available before the OCT appearance. It became possible to observe the pathologic progress in cross-section, OCT changed paradigm of ophthalmic diagnosis dramatically. Even though the structural OCT has been well utilized in ophthalmology, there was limitation for blood flow or vasculature and RPE imaging. Hence, in the case of diseased eye, pathologic changes make it difficult to interpret structural OCT image. In order to supplement the limitation, functional extension was tried in OCT technology.

Penetration into posterior eye is dependent on the probe band. And 1-μm probing beam is promising for the deep posterior, choroid and sclera, imaging due to its low absorption in RPE and low scattering in tissue. Swept-source OCT (SS-OCT) became common for the 1-μm probe band and robust against motion artifacts. Multi-functional imaging of posterior eye was implemented with 1-μm SS-OCT, in order to detect abnormal vasculature and retinal pigment epithelium (RPE). For the vasculature imaging, Doppler shift induced by motion of red blood cell was calculated and flow of blood is contrasted to the static tissue. Software-based phase stabilization algorithm was introduced for the phase-stability of system. For the imaging of blood flow and vasculature, bidirectional Doppler mode and high-sensitive Doppler mode were imployed, with different scanning protocol. Vasculature imaging was applied to ten cases of diseased eye and abnormal vessels are identified from all cases. And obtained vasculature pattern was similar with that of current angiographic method which use dye injection. Noninvasive vasculature imaging with OCT might be useful in ophthalmic diagnosis as an alternative of dye based angiography. For the RPE imaging, degree of polarization uniformity (DOPU) was utilized from data obtained with Jones-matrix polarization-sensitive OCT. Multi-functional imaging was done by simultaneous measurement of vasculature and RPE, and it was applied to six cases of diseased eye with single measurement. Abnormal RPE was detected from six cases and abnormal vessel was detected from five cases. Clinical utility of the

multi-functional imaging of posterior eye has been shown.

Contents

List of Figures

List of Tables

Chapter 1

Introduction

1.1 Exudative macular disease

Human eye is unique optical organ which plays role for vision sensing, however, ocular degeneration, occurred by the genetic background, food intake, living habits and getting age, threaten the vision ability of human. Pathological or degenerative myopia (excess -6D) is a leading cause of blindness worldwide and it is particularly common in Asian countries [1, 2, 3]. Age-related macular degeneration (AMD) is the leading cause of irreversible legal blindness in persons older than 60 years in the developed countries [4, 5]. When the degeneration is progressed more severely, the above diseases result in the generation of choroidal neovascularization (CNV) in the sub-retinal pigment epithelium (sub-RPE) or intra-neurosensory retinal layer. The CNVs are classified into two pathologic types: type I (or occult) CNV and type II (or classic) CNV. Type I CNV originates from choroid and extends under RPE and subsequent detachments of RPE and choroid eventually occur, whereas type II CNV penetrates RPE to expand in the intra-neurosensory retinal layer [6]. Polypoidal choroidal vasculopathy (PCV) is a form of type I CNV and it is characterized by a branching vascular network (BVN) terminating in polypoidal lesions [7, 8] In Asia, polypoidal CNV represents between 56 % and 72% of all neovascular AMD patients [1].

1.2 Ocular blood circulation

Eye acuqires nutrition and excretes metabolic end products through blood circulation, and thus the abnormality of the vasculature is an important indicator of malfunction in the eye [9, 10, 11]. Therefore, the examination of ocular vascular integrity is important in ophthalmic diagnosis. Fluorescein angiography (FA) and indocyanine green angiography (ICGA) are currently commonly used angiographic methods used in ophthalmology [12]. With FA, which is a standard modality, retinal structure is satisfactorily visualized; however it is often difficulto to visualize choroidal vasculature because of the short excitation wavelength (520 nm) of the sodium fluorescein dye. In contrast, the choroidal vasculature is adequately visualized with ICGA because of the longer excitation wavelength (830 nm) of the indocyanine green dye. In those reason, the two angiogaphies are associatively used for the diagnosis. However, these two methods require dye injection to enhance the

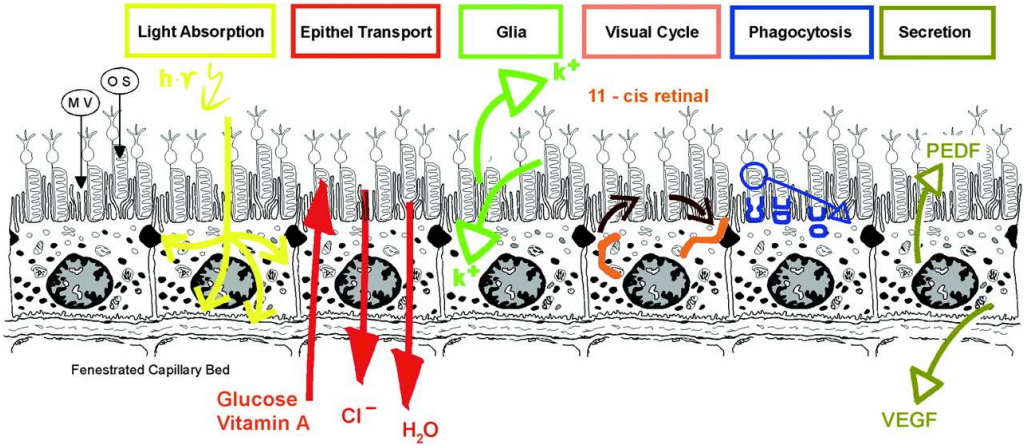

Figure 1.1: Summary of retinal pigment epithelium (RPE) functions. PEDF: pigment epithelium-derived growth factor, VEGF: vascular epithelium growth factor, Epithel: epithelium. Reprinted from Ref. [16]

contrast of the vessels, the dye injection process is uncomfortable for patients, and some adverse allergic reactions may be induced they are uncomfortable for the patients, and they are sometimes associated with severe adverse reactions [13, 14, 15].

1.3 Retinal pigment epithelium

Retinal pigment epithelium (RPE) is a monolayer of pigmented cells and located between retina and choroid. RPE plays significant role in metabolism and regulation of the retina. Fig. 1.1 summarizes several functions of RPE; RPE transports nutritients and metabolic end product between photorecetpors and choriocapillaries, absorbs excess light to protect retina against photo-oxidation, maintains the excitability of photoreceptor outer segment (POS), helps the regeneration of POS by phagocyte the end of POS [16].

In those reason, any disturbance of the RPE can lead to severe visual impairment. FA and fundus auto-flurorescence are utilized for the diagnosis of RPE integrity. Leakage of dye in the late-phase of FA and low auto-fluorescence in fundus auto-fluorescence (FAF) represent RPE damage [17, 18], however the observation is sometimes struggled by severe hemorrhage. Hence, a direct visualization of the RPE would be considerable diagnostic value.

1.4 Optical coherence tomography

Optical coherence tomography (OCT) is a noninvasive imaging modality that produces cross-sectional images at a micrometer scale based on the principle of low-coherence interferometry [19, 20, 21]. Rapid imaging with High-resolution was available with Fourier-domain OCT method [22, 23]. And OCT has been widely applied for ophthalmology, dermatology, dentistry, gastroenterology, and cardiology. Among them, ophthalmic OCT

has been a successful application owing to the optical biopsy images of anterior or posterior of eye. Because human eye is optical organ, there is limitation for taking biopsy. However after the appearance of OCT, it became possible to observe the pathologic progress in cross-section, and OCT changed the paradigm of ophthalmic diagnosis dramatically. Posterior eye is layered structure which is composed of several types of neurons and high-resolution depth-resolved OCT image characterizes the retinal structure even with three-dimensional imaging. Abnormality of posterior eye is able to be detected by a morphological change in cross-sectional OCT image.

Even though the structural OCT was successfully utilized in ophthalmology, there was limitation for blood flow or vasculature and RPE imaging. Athougth the vessels and RPE are distinguishable with other tissue with different scattering property, it is limited for normal eye. In the cases of diseased eye, pathologic changes make it difficult to interpret structural OCT image. In order to supplement the limitation, functional extension was tried in OCT technology.

Doppler OCT was introduced for the blood flow velocity measurement [24,25,26,27,28], for that, Doppler shift frequency induced by flowing red blood cells in the sample was measured. In the begining of Doppler OCT, research was focused on the measurement of blood flow dynamics, and recently, vasculature imaging also attract researcher's attention. For the vessel contrast imaging, variations of Doppler OCT were introduced [29, 30, 31].

Polarization-sensitive OCT (PS-OCT) is an another functional extension, which is capable of measuring the polarization properties of sample, such as birefringence, diattenuation, and optic-aixs orientation [32,33,34,35,36,37,38,39,40]. As ophthalmic applications of PS-OCT, contrast to fibrosis tissues [41, 42, 43, 44, 45], RPE segmentation [46, 47], and quantitative assessment of nerve fibers [48, 49, 50] were demonstrated.

1.5 Aim of this thesis

Recently, 1-μm band swept-source OCT (SS-OCT) became a common OCT for ophthalmic application, because it has advantage of deep-penetration into choroid [51], robustness to the sample motion [52], long measurement range in depth [53], and fast imaging speed [54]. However, there is challenging issue in 1-μm SS-OCT for the implementation of Doppler OCT and PS-OCT, it is phase stabilization.

In this dissertation, clinically applicable functional-extensions of SS-OCT were discussed. First, blood flow and vasculature imaging was implemented with 1-μm SS-OCT based on fully numerical phase stabilization [55] as discussed in Chapter 2, and its clinical utility was examined with 10-cases of exudative macular diseased eye as discussed in Chapter 3 [56]. Simultaneous imaging of vasculature and polarization properties was implemented with passive-component Jones matrix SS-OCT [57] and its clinical utility was examined with 6 cases of diseased eye as discussed in Chapter 4.

Chapter 2

High-penetation Doppler Optical Coherence Angiography (HP-OCA)*

2.1 Introduction

Human tissues, including those in the eye, are fed and they excrete waste through blood circulation, and thus, the abnormality of the vasculature is an important indicator of malfunction in the eye [9,10,11]. Therefore, the examination of ocular vessels is important in ophthalmic diagnosis. Fluorescein angiography (FA) and indocyanine green angiography (ICGA) are current angiographic methods used in ophthalmology. However, they require dye injection to enhance the contrast of the vessels, they are uncomfortable for the patients, and are sometimes associated with severe adverse reactions [15].

OCT is a noninvasive imaging modality that produces cross-sectional images at a micrometer scale [19]. Doppler OCT is an extension of OCT that is capable of detecting the Doppler shift of a probe beam to provide blood flow contrast with a depth-resolved tissue structure [58,59]. On the other hand, Fourier-domain (FD) OCT, which is a second-generation OCT, enables rapid, three-dimensional volumetric imaging [22, 23, 60, 61]. In FD-OCT, the Doppler frequency shift is calculated from the phase difference between adjacent A-lines; for this phase difference calculation [27, 28, 62], high phase stability is required. Although there are several other methods of increasing the contrast of vessels using the Doppler effect, such as Doppler standard deviation imaging [29], phase-variance OCT [30], and joint spectral and time domain OCT [31], phase difference methods are the most common because of their simplicity of implementation [25, 27, 28].

*The portions of this chapter have been published in the following articles:
Y.-J. Hong, S. Makita, F. Jaillon, M. J. Ju, E. J. Min, B. H. Lee, M. Itoh, M. Miura, and Y. Yasuno, "High-penetration swept source doppler optical coherence angiography by fully numerical phase stabilization," Optics Express 20, 2740-2760 (2012).
Y.-J. Hong, M. Miura, S. Makita, M. J. Ju, B. H. Lee, T. Iwasaki, and Y. Yasuno, "Noninvasive investigation of deep vascular pathologies of exudative macular diseases by high-penetration optical coherence angiography," Investigative Ophthalmology & Visual Science 54, 3621–3631 (2013).

To supplement current angiographic methods, optical coherence angiography (OCA) was developed; it is based on the 840-nm spectral domain (SD) Doppler OCT [63]. Recently, there were reports that several ocular diseases, myopia, central serous chorioretinopathy (CSC), and age-related macular degeneration (AMD), are related to choroidal properties [2, 64, 65]. Although the 800-nm band SD-OCT-based OCA was able to measure retinal vessels, its ability to examine choroid was limited. This is mainly because the 800-nm-band probing beam is strongly absorbed by both the melanin in retinal pigment epithelium (RPE) and the choroid, and thus, penetration into the deep choroid is low. To obtain high penetration into the choroid, *in vivo* retinal OCT at 1-μm was demonstrated [51, 66, 67, 68, 69, 70]. The low absorption of melanin at a wavelength of around 1 μm enables high penetration into the choroid.

Recently, swept-source (SS) OCT became a common option to implement 1-μm OCT because of its advantages over SD-OCT, including robustness to motion [52], a long measurement range in depth due to short instantaneous line-width [53], k-linear sampling, compactness [53], and high imaging speed [54, 71].

However, SS-OCT typically has jitter in synchronization between the wavelength sweep and data acquisition; this jitter causes random spectral shifts among interference spectra and results in low phase stability. This low phase stability is a critical problem for phase-sensitive OCT modalities including Doppler OCT. To resolve this issue, previously demonstrated SS-Doppler-OCT commonly utilized a stationary mirror or a glass plate in the sample arm [72, 73, 74]. In this scheme, the unstable phase is measured by monitoring the phase of the mirror or the glass plate and is then corrected numerically. Although this method successfully enhances the phase stability, it requires additional hardware in the sample arm, and thus, it makes the system more complicated and limits the depth measurement range. Recently, Braaf *et al.* demonstrated phase stabilized SS-OCT which stabilizes the phase by using a separate Mach-Zehnder interferometer from an OCT interferometer [75]. Although this system demonstrated excellent phase stability and did not sacrifice depth imaging range, it still requires additional hardware complexity.

In this study, I demonstrate a high-penetration Doppler OCT and OCA based on high-speed 1-μm SS-OCT with a custom-made, fully numerical OCT phase stabilization method without needing any additional calibration hardware. Bidirectional choroidal blood flow and vasculature imaging are then demonstrated. This method does not require any additional calibration hardware, and thus, can be used with any SS-OCT system with a simple software update.

2.2 Methods

2.2.1 Swept-source optical coherence tomography

High-penetration Doppler OCA (HP-OCA) is based on an SS-OCT system with a fiber-based Michelson interferometer. A schematic of the SS-OCT is shown in Fig. 2.1. A commercially available short cavity laser (Axsun Technologies Inc.,MA) with a center wavelength of 1060 nm, a spectral scanning width of 120 nm, a -3-dB bandwidth of 100 nm, and a scanning speed of 100,000 scans/s was utilized. The laser beam passes through

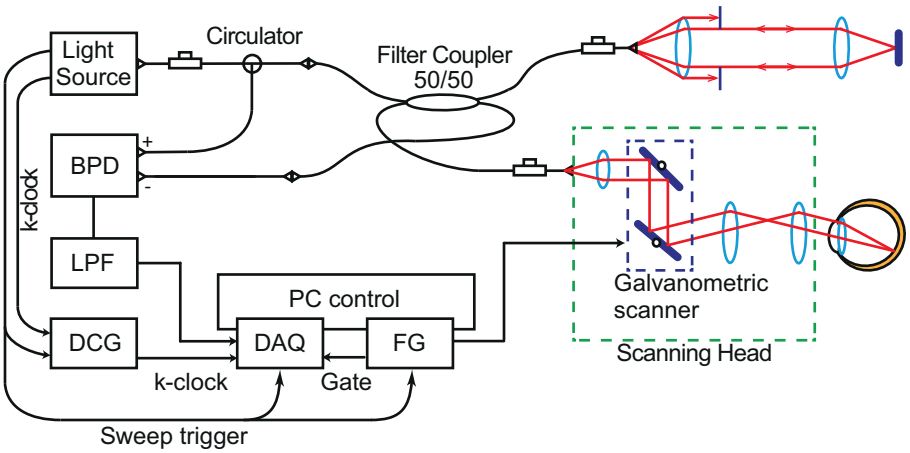

Figure 2.1: Schematic of HP-SS-OCT system. BPD: balanced photodetector, LPF: low-pass filter, DCG: dummy clock generator, DAQ: data acquisition board, FG: function generator.The uncommon configuration of the 50/50 coupler is due to the characteristics of a filter coupler which splits the beam into two opposite ports.

a polarization controller and enters a polarization independnt circulator (Agiltron, MA) with an operation wavelength of 1060 ± 30 nm. A filter coupler (Advanced Fiber Resources Ltd., Hong Kong) passes 50% of the light to the reference arm and reflects 50% into the sample arm. The reference beam power is adjusted using an iris diaphragm. A custom retinal scanner based on a commercial OCT device (3D-OCT-1000, TOPCON Corp., Tokyo, Japan) is connected to the sample arm. The galvanometric scanner steering the probe beam is controlled by a function generator board (PCI-6713, National Instruments, TX). The probing beam power was set as 1.85 mW, which is lower than the safe exposure limit of ANSI standard [76]. The reflected beams from both arms are combined at the coupler and detected by a balanced photodetector with a bandwidth of DC to 350 MHz (PDB130C, Thorlabs Inc.). To avoid high-frequency noise, the detector output signal is passed through a low-pass filter with a cut-off frequency of 170 MHz (7th order type-I Chebyshev filter, R & K Corp., Japan). The interference signal is digitized by a data acquisition (DAQ) board with 12-bit quantum resolution and a maximum sampling rate of 500 MS/s (ATS9350, AlazarTech, QC, Canada).

Data sampling was performed using an optically generated clock signal that is equi-spacing in wavenumber, namely, a k-clock. With the light source utilized in this study, the k-clock becomes unstable during the backward sweep, although only the forward sweeps are utilized for imaging. This unstable k-clock electrically interferes with the triggering of data acquisition. To supply a stable clock signal to the DAQ board during the backward sweep and avoid this interference, a custom-made dummy clock generator is employed. The dummy clock generator switches the clock signal supplied to the DAQ board between the k-clock and a dummy clock signal with a constant frequency (240 MHz) during forward and backward sweeps, respectively. It is noteworthy that the recent versions of 1-μm swept-source provided by AXSUN Technologies possess a similar dummy clock generation

function, and thus, a custom-made dummy clock generator is not needed. Owing to this k-linear sampling, no rescaling process is required.

Synchronization between data acquisition and the galvanometric scanner is achieved using the sweep trigger signal of the light source, which is utilized for triggering the data acquisition of the DAQ for a single sweep and utilized as an update clock for the waveform generation for galvanometric scanning.

The short cavity laser possesses a very narrow instantaneous line width; this short line width provides a very low signal roll-off. The signal roll-off was measured to be -2.5 dB over 3.0 mm. The sensitivity decay was measured to be -7.4 dB over 3.0 mm in air. It should be noted that the sensitivity decay is higher than the signal roll-off. This is due to the noise floor increase in the deeper region. The sensitivity was measured to be 99.1 dB in which the recoupling loss at the fiber tip of the sample arm is compensated. The expected shot-noise-limit sensitivity was 106.1 dB. The optical loss of the system was measured to be 4 dB; this may partially account for the departure of the measured sensitivity from the shot-noise-limit sensitivity. The depth resolution defined by the -6-dB width was measured to be 11.0 μm in air, which corresponds to the resolution of 8.0 μm in tissue (n= 1.38).

2.2.2 Phase-1 numerical phase stabilization:rough spectral shift correction

SS-OCT is commonly associated with jitter in synchronization between the wavelength sweep and data acquisition. This jitter results in random shifts in spectral sampling, and thus, results in jitter in the phase of the OCT signal. As the Doppler frequency obtained by the phase sensitive Doppler OCT algorithm is defined as the phase difference between the two A-scans, this jitter causes a significant error in the Doppler OCT measurement. In this section, a fully numerical method was described for the cancelling of this jitter and for the stabilization of the phase of the OCT; this method was refered as "phase-1 stabilization" in this thesis.

The phase error under consideration is caused by a relative shift between two sampled spectra $S_1(j)$ and $S_2(j)$, where j is the index of the sampling point of the spectrum and is linear with wavenumber k. We assume that $S_2(j)$ suffers from spectral shift by jitter and becomes

$$S_2'(j) = S_2(j) * \delta(j - \beta), \tag{2.1}$$

where β is the spectral shift in the sampling points and $*$ denotes convolution.According to the shift theorem of Fourier transform, the discrete Fourier transform of the shifted spectrum $S_2'(j)$ becomes the discrete Fourier transform of $S_2(j)$ with an erroneous phase:

$$\mathcal{F}\left[S_2'\right](\zeta) = \mathcal{F}\left[S_2\right](\zeta) \exp\left(-i2\pi\zeta\beta/N\right) \tag{2.2}$$

where $\mathcal{F}[\,]$ represents the discrete Fourier transform, N is the number of sampling points in a single spectrum, and $\zeta = 0, 1, \cdots N-1$ is the index of the discrete Fourier pair of j that also represents the depth position of the OCT signal. If the two spectra,

and thus, the two A-lines yielded from these spectra were fully correlated except for the spectral shift, i.e., $S_1(j) = S_2(j)$, the Doppler shift obtained from these two spectra would present this erroneous phase as $\angle\mathcal{F}\left[S_2'\right](\zeta)\mathcal{F}\left[S_1\right]^*(\zeta) = -2\pi\zeta\beta/N$, where the superscript $*$ denotes the complex conjugate. Under this condition, the erroneous phase caused by the jitter could be determined and numerically completely canceled. However, in practice, $S_1(j)$ and $S_2(j)$ are not fully correlated because of the structural difference between the two A-scans and the Doppler shift caused by the flow and bulk motion of a sample. In this strategy, I obtain and correct this erroneous phase by excluding these disturbances by cropping the perfectly correlated component of the spectra, i.e., the spectrum of the reference beam.

In the practical OCT measurements, the spectral interferometric signal $S_1(j)$ is expressed as

$$S_1(j) = |E_r(j)|^2 + |E_{p1}(j)|^2 + E_r(j)E_{p1}^*(j) + E_r^*(j)E_{p1}(j) \tag{2.3}$$

where $E_r(j)$ and $E_{p1}(j)$ are optical fields of the reference beam and probe beam of this A-scan. In a standard configuration, the reference arm length is adjusted so that the OCT signals, i.e., the third and the fourth terms in this equation, do not overlap with the zero-delay position (where the first and the second terms are located). Thus, we can filter out the third and fourth terms. In addition, in the standard OCT configuration, the reference power of the photodetector is significantly higher than the probe power; $|E_r(j)|^2 \gg |E_{p1}(j)|^2$. After performing this filtering and making this assumption, the spectrum becomes $S_1'(j) \simeq |E_r(j)|^2$; its Fourier transform becomes

$$\mathcal{F}\left[S_1'\right](\zeta) \simeq \mathcal{F}\left[|E_r(j)|^2\right]. \tag{2.4}$$

Note that, in practical SS-OCT configuration, $|E_r(j)|^2$ to be measured is not a reference spectrum in a precise sense because of the common mode rejection capability of balanced photo-detection. However, this effect is negligible as it is discussed in Section 2.4.1.

Similarly, the shifted spectrum of $S_2'(j)$ in practical OCT measurement is expressed as

$$S_2'(j) = \left\{|E_r(j)|^2 + |E_{p2}(j)|^2 + E_r(j)E_{p2}^*(j) + E_r^*(j)E_{p2}(j)\right\} * \delta(j-\beta), \tag{2.5}$$

where $E_{p2}(j)$ is the optical field of the probe beam of this A-scan. A similar filtering and assumption for $S_1(j)$ provides the cleaned-up spectrum of $S_2''(j) = |E_r(j)|^2 * \delta(j-\beta)$ and its Fourier transform of

$$\mathcal{F}\left[S_2''\right](\zeta) \simeq \mathcal{F}\left[|E_r(j)|^2\right](\zeta)\exp\left(-i2\pi\zeta\beta/N\right). \tag{2.6}$$

It is evident that Eqs. (2.4) and (2.6) are identical except for the erroneous phase slope component caused by the spectral shift. This erroneous phase is easily obtained using the following operation and thus, is easily canceled numerically.

$$\mathcal{F}\left[S_2''\right](\zeta)\mathcal{F}\left[S_1'^*\right](\zeta) = I(\zeta)\exp\left(-i2\pi\zeta\beta/N\right), \tag{2.7}$$

where $I(\zeta) \equiv \left|\mathcal{F}\left[|E_r(j)|^2\right]\right|^2$ and is equivalent to the OCT signal intensity.

In practical calculations with measured spectra, the phase obtained from Eq. (2.7) does not always have a perfectly linear slope. Thus, I determined the phase slope by weighted least-square fitting which determines the value of β that minimizese the following error energy.

$$R_1^2 \equiv \sum_{\zeta} I(\zeta) \left[-2\pi\zeta\beta/N - \varphi(\zeta)\right]^2, \tag{2.8}$$

where $\varphi(\zeta)$ is the differential phase defined as $\angle\mathcal{F}\left[S_2''\right](\zeta)\mathcal{F}\left[S_1'^*\right](\zeta)$, and $\mathcal{F}\left[S_2''\right](\zeta)$ and $\mathcal{F}\left[S_1'^*\right](\zeta)$ are derived from measured spectra $S_1(j)$ and $S_2(j)$. $I(\zeta)$ is set to zero if it is smaller than the noise level.

A detailed overview of the numerical phase stabilization process used in our particular implementation is as follows. First, the DC offset for each spectrum is removed by subtracting the mean of each spectrum so as to set the balanced voltage to zero. Discrete Fourier transform is performed after applying a Gaussian window with a standard deviation of $0.2N$ where $N = 1536$. Offset cancelation is important, otherwise the interaction between the offset and the window function degrades the accuracy of phase-1 stabilization. Namely, the offset reformed by the window function numerically mimics a pseudo spectrum with the shape of the window function, which has no spectral shift and overlapped with the real spectrum, and hence it disturbers the phase-1 stabilization. It is noteworthy that numerical dispersion compensation is not applied because the signal of interest is formed only from the reference beam, and thus, it is not affected by dispersion. The ± 30 pixels close to the zero-delay are utilized for the analysis. This ± 30-pixel width corresponds 304 μm in air and roughly 28 times the measured depth resolution defined as the 6-dB width. The phase difference between an A-line under shift correction and a reference A-line (typically the first A-line in an OCT volume) is obtained by multiplying the complex conjugate of the reference A-line by the A-line under correction. Least square fitting, described above, is applied to obtain the phase slope, which is proportional to the spectral shift. Finally, cancelation of the spectral shift is performed by multiplying the complex conjugate of the estimated phase slope to the entire ζ-range of the Fourier-transformed spectrum and then taking the inverse Fourier transform. Standard Fourier domain OCT (FD-OCT) processing (including complex median subtraction to eliminate fixed pattern noise [77] and automatic numerical dispersion compensation [67]) is then applied to obtain a phase-stabilized OCT image.

It should be noted that, phase-1 stabilization uses a signal generated by a reference beam which occupies the region close to the zero delay. And hence OCT signal should not be overlapped with this region and hence this region cannot be utilized for OCT imaging despite of its high sensitivity. This might be a drawback of phase-1 stabilization. However, in the clinical practice, imaging a retina at a region close to zero delay is generally discouraged to prevent the image folding due to the eye motion. And hence the negative effect of this drawback would be minimal.

2.2.3 Phase-2 numerical phase stabilization: Correction of residual spectral shift and bulk motion

To obtain the Doppler OCT image, the phase difference between adjacent A-lines of the phase-stabilized OCT image is calculated by multiplying an A-scan by the complex conjugate of the other A-scan.

As described in Section 2.2.2, spectral shift cancelation (phase-1 stabilization) is performed using tens of data points, which is close to the zero delay. Because data points close to the zero delay are relatively insensitive to the phase error than the data points far from the zero delay, a certain level of residual fine spectral shift will still exist. In addition, the Doppler frequency measured from an in vivo subject, such as a human eye, is sensitive not only to the flow of interest but also to the bulk motion of the subject. Although bulk motion is a true signal in the broadest sense of term, it frequently disrupts flow measurement and should therefore be canceled. In this section, I describe the phase-2 phase stabilization algorithm, which eliminates the residual phase errors caused by residual spectral shift and bulk motion.

By accounting for these errors, the Doppler phase shift obtained from a sample is described as

$$\Delta\varphi(\zeta) = \frac{4\pi\tau}{\lambda_c} n v_z(\zeta) + \frac{4\pi\tau}{\lambda_c} v_b - 2\pi\zeta\beta'/N, \tag{2.9}$$

where τ is the time interval between two A-scans under Doppler calculation, λ_c is the center wavelength, n is the refractive index of the sample, $v_z(\zeta)$ is an axial velocity of the flow of interest, v_b is the axial velocity component of the sample bulk motion, and β' is the residual spectral shift. It should be noted that $v_z(\zeta)$ is a function of depth (ζ), whereas v_b is a constant; therefore, the second term of this equation is a depth-independent phase offset. The third term is generated by the residual spectral shift and is a linear function of depth whose slope is in proportion to the residual spectral shift β'. It is noteworthy that if β' is very large, phase wrapping occurs and the third term can no longer be a linear function of depth. In our algorithm, β' is warranted to be sufficiently small owing to phase-1 stabilization.

In this phase-2 stabilization algorithm, weighted linear fitting is applied to each depth-resolved Doppler signal $\Delta\varphi(\zeta)$. If the effect of the flow of interest is negligible (in other words, if we only consider the Doppler signal of a static part of the sample), the slope and intercept of the linear fitting line are respectively proportional to the residual spectral shift and the bulk motion as evident in Eq. (2.9). Therefore, these two errors can be canceled by subtracting this fitting line from the phase. However, in practical measurement, the flow of interest is not negligible. In the phase-2 stabilization algorithm, this disturbance from the flow of interest is eliminated by iterative fitting described below.

In this iteration, weighted linear fitting was applied to the measured Doppler signal, which determines the slope and intersept so as to minimize the following error energy:

$$R_2^2 = \sum_{\zeta} W_m(\zeta) \left[\Delta\varphi(\zeta) - (a_m\zeta + b_m)\right]^2 \tag{2.10}$$

where $\Delta\varphi(\zeta)$ is the Doppler signal obtained from a measurement, a_m and b_m are the slope

and the intersept determined by the i-th iteration, respectively, and $W_m(\zeta)$ is the weight of the fitting. For the first iteration ($m = 0$), $W_0(\zeta)$ is defined as

$$W_0(\zeta) = \begin{cases} \sqrt{I(\zeta)} & : \quad I(\zeta) > \epsilon^2 \\ 0 & : \quad \text{otherwise} \end{cases} \tag{2.11}$$

where $I(\zeta)$ is the OCT signal intensity of the corresponding A-line, and ϵ^2 is the noise level.

In this method, I iteratively exclude the part with flow from the fitting by relying on the assumption that the Doppler shift caused by the real flow is eccentric with respect to the phase slope defined by the second and third term of Eq. (2.9). To exclude the part that satisfies this assumption, the weight is updated as

$$W_m(\zeta) = \begin{cases} 0 & : \quad |\Delta\varphi_m(\zeta) - (a_{m-1}\zeta + b_{m-1})| \geq T(m; p, M) \\ W_0(\zeta) & : \quad \text{otherwise} \end{cases} \tag{2.12}$$

where $m = 0, 1, 2, \cdots, M$, the iteration step of linear fitting. $T(m.p.M)$ is threshold for the update of weight, $W_m(\zeta)$, and the weight is set to zero if the fitting error is larger than or equal to the threshold. Threshold, $T(m.p.M)$, was defined as following

$$T(m; p, M) = \frac{\pi}{p}\left\{1 + \frac{p-1}{1 + \exp(m - M/2)}\right\} \tag{2.13}$$

where p is a constant determined by the phase stability obtained after the phase-1 stabilization. Note that Eq. (2.13) is a monotonically decreasing sigmoid function with the maximum limit of π and the minimum limit of π/p, and p was set to make π/p to be the phase noise level. In our particular case, $p = 12$. M is the total iteration number of iteration, and in our particular case, $M = 7$.

Note that Eq. (2.13) is a sigmoid function. And hence, In this condition, $T(m; p, M)$ keeps large for the first iterations, rapidly decreases at around the middle of the iteration, and becomes relatively constant for the late steps of the iterations. And this should be noted, according to Eq. (2.12), even the weight was set to zero once, if the fitting error of $(m-1)$-th step become less than the threshold of m-th step linear fitting, the weigth is retreived and the Doppler phase of ζ position could be utilized for m-th step linear fitting. Hence this algorithm estimates the phase error caused by the system instability and the bulk eye motion accurately and improves the image quality of Doppler tomography and OCA.

After applying the phase-2 stabilization, a 3-D Kasai auto-correlation filter [78,79] was applied to the Doppler signal to further improve the Doppler sensitivity. Two Doppler modes were implemented for HP-OCA, bi-directional and high-sensitive modes as described in section 2.2.4. The kernel sizes utilized were 4 pixels (depth) $\times$ 4 pixels (horizontal) $\times$ 1 pixel (vertical) for the bi-directional mode, and 4 pixels (depth) $\times$ 1 pixel (horizontal) $\times$ 4 pixels (vertical) for the high-sensitive mode. This kernel sizes correspond to the physical size 19.0 μm (depth) $\times$ 38.8 μm (horizontal) $\times$ 30.0 μm (vertical) for the bi-directional mode and 19.0 μm (depth) $\times$ 30.0 μm (horizontal) $\times$ 38.8 μm (vertical) for the high-sensitive mode.

2.2.4 Bi-directional and high-sensitive Doppler modes

Because flow velocity is calculated from phase difference, the measurable minimum axial velocity is limited by phase noise σ_φ [80]. Further, the measurable maximum axial velocity is limited by the 2π-ambiguity of the phase, i.e., the measured phase value is wrapped onto the range from to $-\pi$ to π. Finally, the measurable velocity range is given by

$$\frac{\lambda_c \sigma_\varphi}{4\pi n \tau} \leq |v_z| \leq \frac{\lambda_c}{4n\tau} \tag{2.14}$$

where τ is the time interval between the two A-scans utilized for the Doppler calculation. It should be noted that the velocity range is downward-shifted as τ increases. In other words, a larger value of τ provides slower Doppler velocity signal and *vice versa*.

In our device, I implemented two scanning modes to achieve two velocity ranges; so-called bi-diretional and high-sensitive Doppler modes. The bi-diretional Doppler mode, also referred to as the intra-B-scan mode, calculates the phase difference between adjacent A-lines in a B-scan as same as conventional Doppler OCT. In our implementation, $\tau = 10$ μs. In this configuration, the theoretically estimated best velocity range is from 1.75 mm/s to 19.2 mm/s, where the phase noise is assumed to be limited by the signal-to-noise ratio (SNR) and structural decorrelation by the transverse scanning. The SNR was assumed to be 25 dB, and the structural decorrelation was estimated from the separation of A-lines at one-tenth the optical transverse resolution.

The high-sensitive Doppler mode, also referred to as the inter-B-scan mode, calculates the phase difference between adjacent B-scans at each A-line [81]. In our implementation, $\tau = 3.2$ ms. The velocity range at this configuration is theoretically estimated from 5.2 μm/s (at 25-dB SNR) to 60 μm/s, where the phase noise is again assumed to be limited by the SNR and structural decorrelation. With this mode, almost all vessels are measured owing to the slow minimum measurable speed. However, the reduced maximum speed results in multiple phase-wrappings.

Two Doppler modes are switched by changing the scanning protocol. The typical protocols for the two Doppler modes are 2048 A-lines (horizontal) $\times$ 256 A-lines (vertical) for the bi-diretional Doppler mode and 256 A-lines (horizontal) $\times$ 2048 A-lines (vertical) for the high-sensitive Doppler mode. Both scans of the two Doppler modes typically cover 6 mm $\times$ 6 mm area. To make the phase noise for both Doppler modes identical, the separation between A-lines utilized for the Doppler processing is set identically for both modes. The separation is about one tenth of the spot size of the probing beam: 2.9 μm for a spot size of 30 μm in our particular implementation.

For the visualization of Doppler images, two visualization modes are utilized. One is a bidirectional Doppler visualization mode in which a white-to-black colormap ranged from $-\pi$ rad to π rad or a blue-to-red colormap ranged from -0.37π rad to 0.37π rad is assigned to $\Delta\varphi$. The positive value of $\Delta\varphi$ represents a positive flow direction, which represents the flow direction from posterior to the anterior in a posterior eye. The other is a power Doppler visualization mode in which a black-to-white colormap or a gradual-red colormap (invisible for 0 rad^2 to red for π^2 rad^2) is assigned.

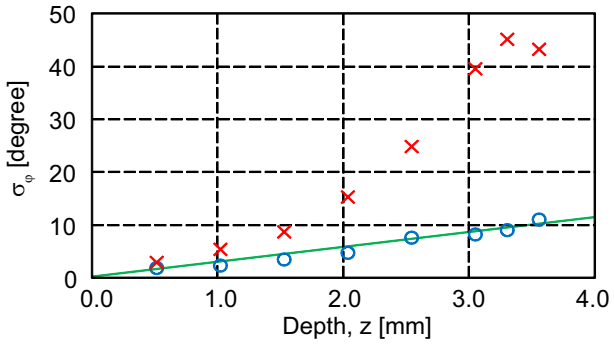

Figure 2.2: Phase stability measured at several depth position with (○) and without (×) phase-1 stabilization algorithm. The green line represents theoretical prediction (see Section 2.4.1).

2.3 Results

2.3.1 Phase stability

To quantitatively examine the enhancement of phase stability obtained from the phase-1 stabilization algorithm, a stationary mirror was used as a sample. In this measurement, lateral scanning was not performed and the mirror was measured at several distances from the zero delay. The standard deviation of the phase differences between adjacent A-lines (σ_φ) is measured at the mirror position. The standard deviations were obtained with and without phase-1 stabilization; 1024 A-lines were utilized for each calculation. As shown in Fig. 2.2, the phase stability is significantly enhanced, especially in the deep region.

As the phase-2 stabilization algorithm is designed to work with a practical sample that involves bulk motion and a flow of interest, it is not possible to quantitatively evaluate this algorithm using the mirror sample. To semi-quantitatively evaluate this algorithm, I measured an *in vivo* human retina and evaluated the histogram of a section of the retina that does not contain visible blood vessels.

Figure 2.3 shows bidirectional Doppler phase shift images obtained from an *in vivo* human eye. Each pane represents the bidirectional Doppler signal without phase stabilization (Fig. 2.3(a)), with phase-1 stabilization (Fig. 2.3(b)), with phase-1 and phase-2 stabilizations (Fig. 2.3(c)), and with phase-1 and phase-2 stabilizations and Kasai filter (Fig. 2.3(d)). The region indicated by the small yellow box is utilized for the phase stability evaluation. The insets indicated by the large yellow boxes are the magnified images of the small yellow box. Figure 2.4 shows histograms obtained from the regions indicated by yellow boxes in Fig. 2.3. Figures 2.4(a)–(d) correspond to Figs. 2.3(a)–(d).

Abrupt spectral shift caused by erroneous synchronization between the starting trigger of the wavelength sweep and data acquisition resulted in several vertical line artifacts, as shown in Fig. 2.3(a) (arrows). This produced the side lobes in the corresponding histogram of Fig. 2.4(a) and a large standard deviation of $\Delta\varphi$ of 43.6°. It should be noted that this standard deviation would be significantly larger than that measured using a static mirror possibly because of the lower SNR and structural decorrelation between A-lines, and thus,

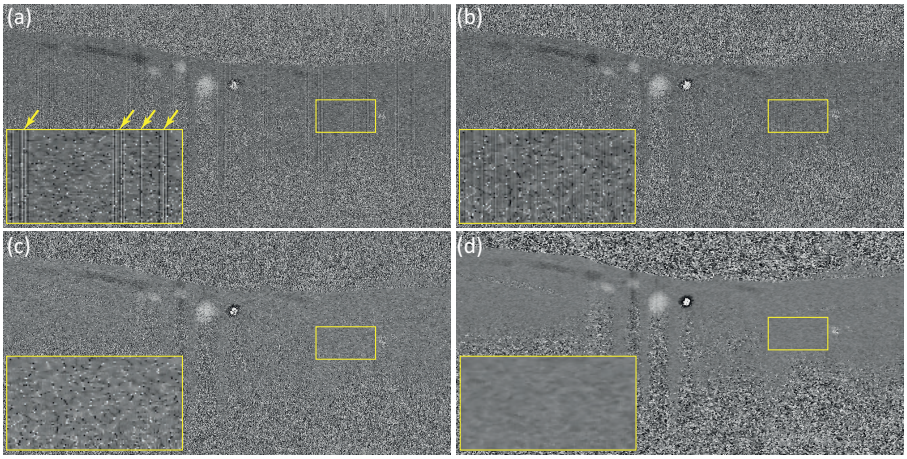

Figure 2.3: Bidirectional Doppler phase images without phase stabilization (a), with phase-1 stabilization (b), with phase-1 and phase-2 stabilizations (c), and with phase-1 and phase-2 and Kasai filter (d).

cannot be directly compared with the value presented in Fig. 2.2. By applying phase-1 stabilization, the vertical line artifacts were dramatically reduced, as shown in Fig. 2.3(b). This reduction corresponded with the disappearance of side lobes in Fig. 2.4(b). The standard deviation decreased to a value as small as 38.0°. Despite the reduction of standard deviation, the constant phase offset induced by bulk motion still exists, as shown in the histogram. This phase offset was successfully eliminated by phase-2 stabilization, as shown in Fig. 2.4(c). It was also found that the histogram was further narrowed and that the standard deviation was decreased to 35.7°. The Kasai filter further reduced the phase noise, as shown in Fig. 2.3(d), and further narrowed the histogram to the standard deviation of 9.8°, as shown in Fig. 2.4(d).

2.3.2 Bidirectional blood flow imaging by bi-diretional Doppler mode

To demonstrate bidirectional *in vivo* flow imaging of a retina, I measured a healthy retina of a 31-year-old Asian male. 6 mm × 6 mm areas centered at a macula and an optic nerve head (ONH) were scanned with 2048 × 256 A-lines in the bi-diretional (intra-B-scan) Doppler mode. A single volumetric scan took 6.6 s. Figure 2.5 shows the cross-sectional OCT intensity and Doppler OCT images. In the macular region, several choroidal blood flows are visible; they are indicated by arrows in Fig. 2.5(b) In the ONH region, both the choroidal and the retinal vessels are visible; they are indicated by arrows in Fig. 2.5(d).

To provide intuitive and comprehensive recognition of three-dimensional flow structures, the volumes of the OCT intensity and bidirectional flow signal were combined, as shown in Fig. 2.6. The OCT intensity is rendered as green; the bidirectional blood flow is rendered using a red-blue colormap. Both in the macular and the ONH regions (Figs. 2.6(a) and (b)), several choroidal vessels are visualized. In the ONH region (Fig. 2.6(b)), large retinal vessels are clearly seen, while the visibility of retinal vessels in macula (Figs. 2.6(a)) is relatively low. This may because the measurable minimum velocity of the bi-

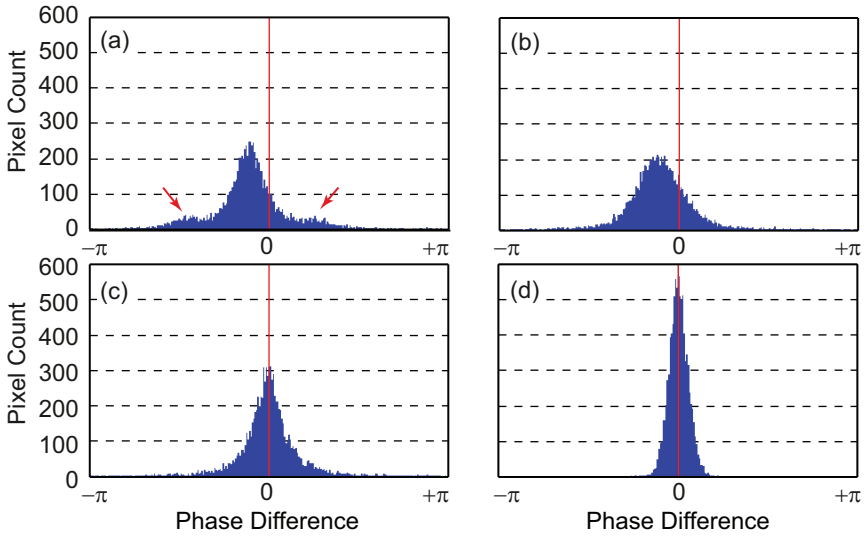

Figure 2.4: Histogram of Doppler phase shift in static tissue regions indicated by yellow boxes in Fig. 2.3. Panes (a)–(d) correspond to Figs. 2.3(a)–(d), respectively.

diretional Doppler mode is too high to visualize fine retinal vessels in the macular region. I will demonstrate the visualization of fine retinal vessels in the high-sensitive Doppler mode in Section 2.3.3.

To evaluate the performance of high-penetration bidirectional blood flow imaging of bidiretional Doppler mode, I measured 12 eyes of 6 Asian subjects without marked posterior disorders. All subjects were male and their age was 29.6 ± 3.7 years (mean ± standard deviation); their ages ranged from 25 to 36 years. For this study, 3 mm × 3 mm areas of maculae and ONHs werescanned with 1024 × 256 A-lines. The scan of a single volume took 3.3 s. Some representative images are shown in Fig. 2.7.

In the ONH area, bidirectional blood flow was visible in the retina and choroid in all 12 eyes. Among them, blood flow beneath the lamina cribrosa was visible in 1 eye, as indicated by a yellow circle in Fig. 2.7(c) (case-1). In the macular area, blood flow was clearly observed in choroid in 11 out of the 12 eyes, as shown in Fig. 2.7(f) (yellow circles, case-2). Eight of the 12 eyes were myopic, which is defined as the spherical equivalent refractive error of more than - 3 diopters; 6 of the 8 myopic eyes were appeared with myopic conus. As exemplified by Fig. 2.7(i) (yellow circle, case-3), 5 of the 6 eyes with myopic conus showed blood flow signals beneath the conus. The red circles in Figs. 7(b), (e), and (h) indicate the same locations as the yellow circles in Fig. 2.7(c), (f), and (i). It should be noted that here the vessels/flow were classified as “visible” as long as a portion of the vessel was observed in the bidirectional Doppler image.

2.3.3 Vasculature imaging by high-sensitive Doppler mode

The same subject as described as the first subject in Section 2.3.2 was examined in the high-sensitive Doppler mode. 6 mm × 6 mm areas of ONH and macula were scanned

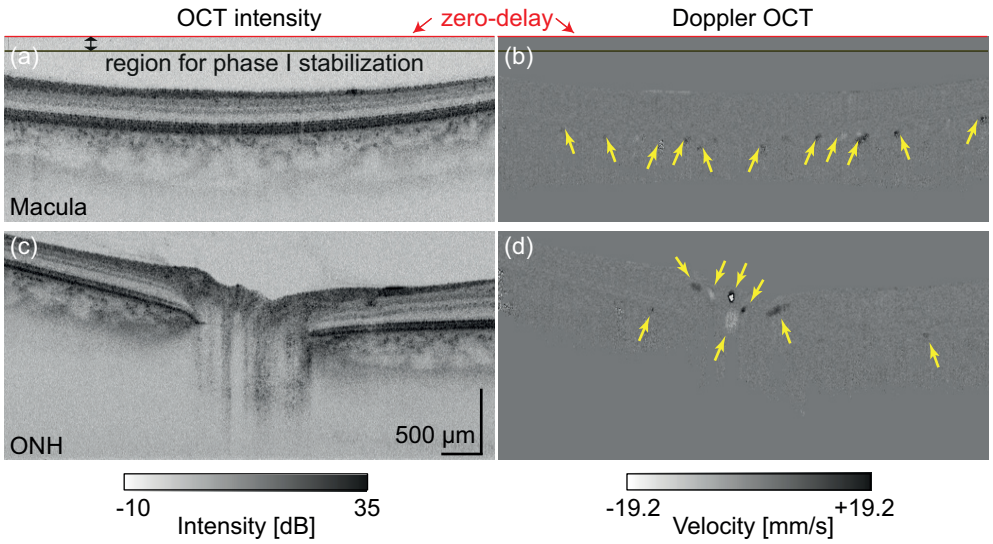

Figure 2.5: OCT intensity images (a) and (c) and bidirectional Doppler images (b) and (d) of a healthy human retina. A horizontal 6-mm regeion was scanned with 2048 A-lines for single B-scan. The red horizontal lines indicate the zero delay, and the region between the red and black horizontal lines indicate the region which has been utilized for phase-1 stabilization. The bidirectional Doppler images were taken in the bi-diretional Doppler mode.

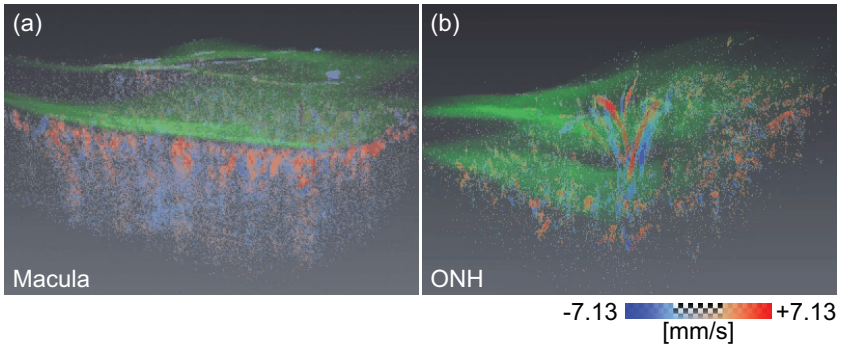

Figure 2.6: Integrated volume rendering of OCT intensity and bidirectional flow in healthy retina.

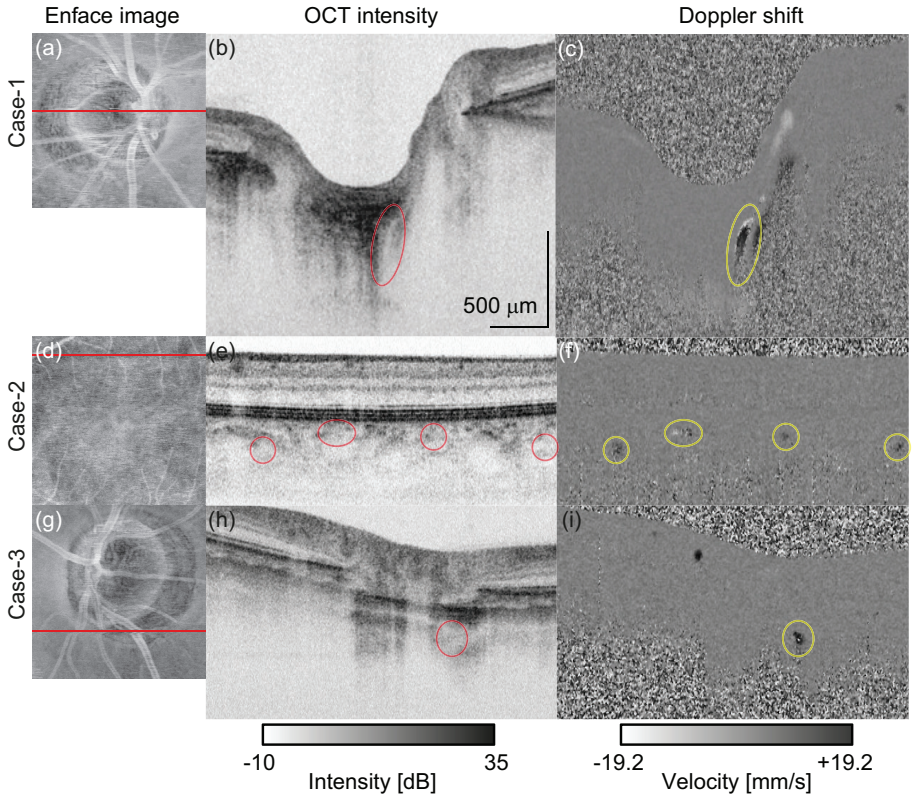

Figure 2.7: Representative images taken for a feature-visibility study. The scanning range was 3 mm (horizontal) × 3 mm (vertical) corresponding 1024 × 256 A-lines. Cases-1 and-3 are of ONH and case-2 is of macula. (a), (d), and (g) are *en face* projections of OCT intensity; (b), (e), and (h) are intensity B-scans; and (c), (f), and (i) are bidirectional flow images obtained in the bi-diretional Doppler mode. The red circles in (b), (e), and (h) indicate the same locations as the yellow circles in (c), (f), and (i). The red lines in (a), (d) and (g) represent the location corresponding B-scans.

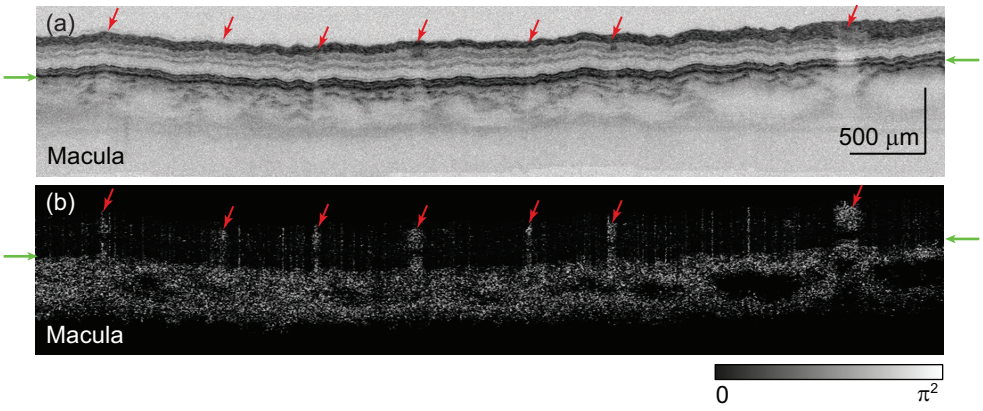

Figure 2.8: OCT intensity (a) and power Doppler (b) images taken from a normal subject in high-sensitive Doppler mode. A vertical 6-mm region was scanned with 2048 B-scans. The arrows indicate retinal vessels.

with 256 × 2048 A-lines in 6.6 s. Figure 2.8 shows the cross-sectional OCT intensity (Fig. 2.8(a)) and power of the Doppler phase shift (Fig. 2.8(b)) images in the macula area, where the green arrows indicate the same location in these two figures. Instead of losing the bidirectionality of the Doppler phase shift because of the reduced measurable velocity range and its resulting multiple phase-wrapping, many Doppler shift signals are observed. The retinal vessels are visible in both the OCT and the Doppler OCT images, as indicated by red arrows. Although it is not easy to recognize individual vessel structures, densely visualized Doppler phase shift signals under the RPE are consistent with the anatomical property of the choroid. In Fig. 2.8(b), the power Doppler signal in the choroid shows a random appearance.

To provide a more comprehensive clinical understanding of vasculature, *en face* projections of the power Doppler signal, also referred to as OCA, were created, as shown in Fig. 2.9. For comparison, the power Doppler projections were created both in the bi-diretional Doppler mode (Fig. 2.9(a)) and in the high-sensitive Doppler mode (Fig. 2.9(b)). In the case of the bi-diretional Doppler mode (Fig. 2.9(a)), the density of visualized vessels is small because of the relatively high minimum measurable velocity in the high-sensitive Doppler mode. In the case of the high-sensitive Doppler mode (Fig. 2.9(a)), clear retinal vasculature and dense choroidal vasculature are visualized.

Owing to the depth resolution of OCT and automatic segmentation of RPE [63], It is possible to created two separate OCAs from a single volume of high-sensitive Doppler mode; one is for retinal angiogram and the other is for choroidal angiogram, as shown in Fig. 2.10. It is noteworthy that this clear separation of depth layers can be performed neither by fluorescein angiography (FA) nor ICGA. The horizontal line artifacts indicated by red and yellow arrows are caused by imperfections in axial shift motion cancelation and saccadic motion, respectively. The details of the line artifacts are discussed in Section 2.4.4.

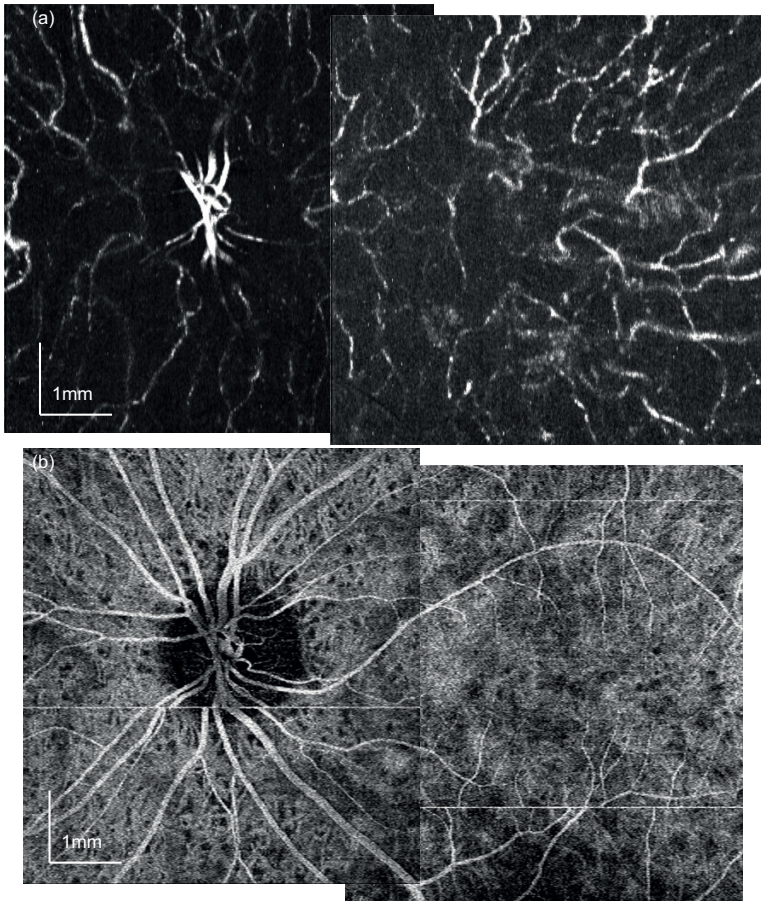

Figure 2.9: *En face* vasculature images obtained by (a) bi-diretional and (b) high-sensitive Doppler modes. The sizes of the datasets for bi-diretional and high-sensitive Doppler modes are 2022 × 255 A-lines in 5.92 mm × 5.98 mm (bi-diretional Doppler mode) and 234 × 2045 A-lines in 5.48 mm × 5.99 mm (high-sensitive Doppler mode).

2.4 Discussion

2.4.1 Effects of common mode rejection by dual-balanced photodetector

As described in Section 2.2.2, the phase-1 stabilization algorithm relies on the OCT signal that is generated only by the reference beam. However, this signal is a common mode for dual-balanced photo-detection, and thus, cannot be detected if the dual-balanced photo-detection is perfectly working. In this section, I show that a standard dual-balanced photodetector and standard power configuration of OCT provide sufficient signal intensity to allow the use of the phase-1 stabilization algorithm owing to the inevitable imperfection of the photodetector.

In a standard OCT configuration, the reference power at the detector is much higher than the probe power. In our configuration, for a probe power at the sample of 1.85

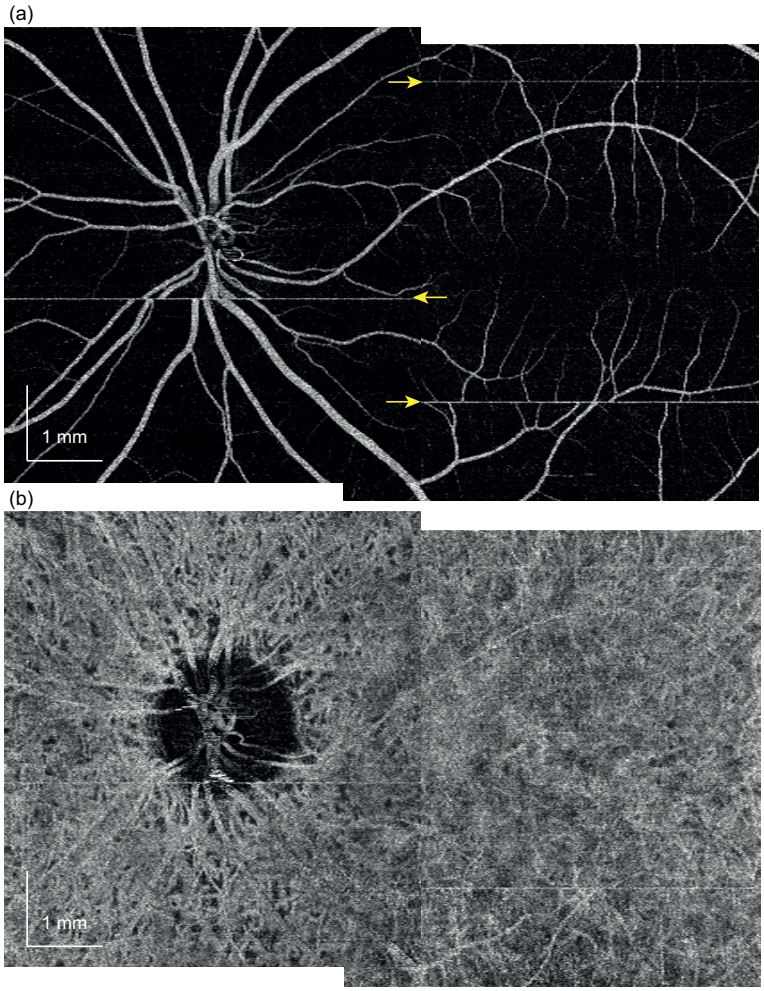

Figure 2.10: Retinal (a) and choroidal (b) optical coherence angiograms of a normal eye. The angiograms were created as projections of the power Doppler signal obtained in the high-sensitive Doppler mode.

mW and a well known retinal reflectivity of -60 dB, the probe power at the detector is estimated to be 1.85 nW. In contrast, the reference power at the detector was configured to be approximately 230 μW. Although a huge portion of the reference power is rejected by the common-mode rejection nature of dual-balanced detection, an considerable portion remains. The typical common-mode rejection ratio of our balanced photodetector is -40 dB; therefore, the residual reference power should be 23 nW.This is still 12 times higher than that of the probe beam. Therefore, even with the dual-balanced photo-detection scheme, the signal intensity would be sufficiently high for the phase-1 stabilization.

The following analysis would provide more quantitative measure of the required signal intensity for phase-1 stabilization. The phase-1 stabilization relies on linear fitting of the phase around the zero-delay point. In our implementation, the fitting area is ± 30 pixels around the zero delay. Since the phase is an odd function of a depth, this fitting is equivalent to the fitting of the area from 0th to 30th pixel with a constriction of null-intercept. Under this condition, a least square fitting provide a slope of the fitting line as $\sum_i \zeta_i \varphi_i / \sum_i \zeta_i^2$, where ζ_i and φ_i are the depth position and the phase value of the i-th data point to be fitted, respectively, and $i = 0, 1, \cdots, 30$. Here I have assumed, for simplicity, the signal is uniformly distributed along the fitting area, and hence the weight of the fitting is constant.

By using this fitting line, the erroneous phase occurred by a spectral jitter at the depth of z is expected to be $\varphi = \left(\sum_i \zeta_i \varphi_i / \sum_i \zeta_i^2\right) \zeta$. By partially differentiating this equation by φ_i, I have the following equation which relates the tiny variations of φ and φ_i as

$$d\varphi = \frac{\sum_i \zeta_i d\varphi_i}{\sum_i \zeta_i^2} \zeta \tag{2.15}$$

where $d\varphi$ and $d\varphi_i$ are the tiny variations of φ and φ_i. Here $d\varphi_i$ is interpreted as an error in the phase measurement due to a stochastic phase noise of OCT and $d\varphi$ is a resulting error in the phase estimation. Although the stochastic phase error cannot be deterministically predicted, its statistical property can be predicted as $\sigma_i = 1/\sqrt{\mathrm{SNR}_i}$ [80], where σ_i and SNR_i are the standard deviation of the stochastic phase error and SNR at z_i. Since the signal intensity is assumed to be uniformly distributed within the fitting region, $\sigma_0 = \sigma_1 = \cdots = \sigma_{30} \equiv \sigma$. In our specific configuration, σ is expected to be 0.025 rad.

By applying error propagation analysis to Eq. (2.15), it is found that the phase estimation at z might have a phase error with standard deviation of

$$\sigma_z = \frac{|z|}{\sqrt{\sum_i z_i^2}} \sigma. \tag{2.16}$$

By substituting our experimental parameters, this equation gives a theoretical prediction of phase estimation error at each depth as shown in Fig. 2.2 (green line). This theoretical prediction is well agreed with the experimental results. According this prediction, the phase error at the deepest perimeter of the measurement range is predicted to be $\sigma_d = 0.19$ rad. Since the condition which warrants a correct operation of phase-2 stabilization, i.e. non-existence of phase wrapping, is $\sigma_d < \pi$, the phase-1 stabilization surely can provide a sufficient phase stabilization.

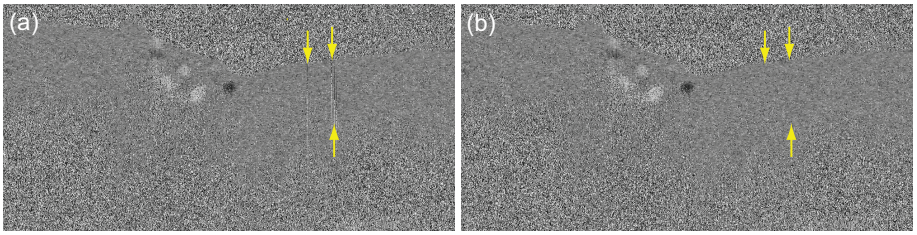

Figure 2.11: Bidirectional Doppler images obtained only with phase-2 stabilization (a) and with phase-1 and phase-2 stabilizations (b). The yellow arrows in (a) indicate A-lines where phase artifacts exist. The arrows in (b) indicate the identical locations to those in (a).

2.4.2 The role of phase-1 stabilization

The phase-2 stabilization aims at canceling both a Doppler phase slope occurred by spectral shift and Doppler phase offset occurred by bulk motion of the sample, while phase-1 stabilization is designed only to cancel the Doppler phase slope. Because of this inclusive property of phase-2 stabilization, phase-1 stabilization is not always required.

However, phase-2 stabilization can work only if no phase wrapping exists in a static tissue which phase-2 stabilization uses to monitor the phase. This condition of no phase wrapping is not always warranted. In contrast, phase-1 stabilization is robust for this wrapping issue although its accuracy is less excellent than phase-2. This is because phase-1 stabilization relies on phase close to the zero delay where phase wrapping is unlikely happened. And hence, the purpose of phase-1 is to cancel the phase slope only with low accuracy but to surely eliminate phase wrapping in the region of the static tissue. This elimination assures successful application of the subsequent phase-2 stabilization.

An example showing this role of phase-1 stabilization is shown in Fig. 2.11. Figure 2.11(a) shows an example of a bidirectional Doppler image which is stabilized only by phase-2 stabilization. Evident artifacts, vertical lines, exist as indicated by yellow arrows. Figure 2.11(b) shows the same Doppler B-scan but stabilized both by phase-1 and phase-2 stabilizations. It is evident that the line artifacts are totally eliminated.

2.4.3 Weight for linear fit in numerical phase stabilization

In both the phase-1 and phase-2 stabilization algorithms, weighted least square fitting was utilized, as described in Sections 2.2.2 and 2.2.3. It should be noted that the OCT intensity is used as the weight in Eq. (2.8) of phase-1, whereas the OCT amplitude, i.e., the square root of the intensity, is utilized in Eq. (2.10) of phase-2.

It is known that the energy of the SNR-limited phase noise of OCT is inversely proportional to the OCT intensity as long as the OCT noise level is constant [80]. Therefore, using the OCT intensity as the weight in Eq. (2.8) is rational.

In contrast, the use of the square root of the intensity in Eq. (2.10) derives from the following compromise. The retinal blood vessels have strong scattering in OCT in general. Although the phase-2 stabilization algorithm is designed to avoid the effects of Doppler

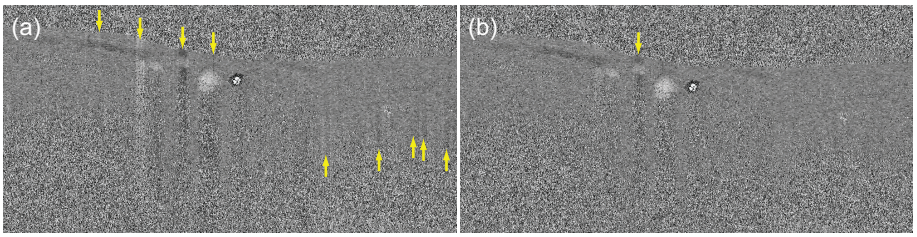

Figure 2.12: Bidirectional Doppler images stabilized by phase-1 stabilization followed by non-standard phase-2 stabilization which uses an OCT intensity as a weight (a) and by phase-1 stabilization followed by standard phase-2 stabilization. The arrows indicate phase artifacts occurred by the imperfection of the phase-2 stabilization.

shift in the retinal vessel, the linear fit will be strongly affected by the blood flow if we utilize the OCT intensity as the weight. To reduce the effect of the blood flow and to give a larger weight to high-SNR regions, the square root of the intensity was utilized for the weight. The sufficient performance of the algorithm with this compromise was experimentally verified in Section 2.3.1.

In order to further demonstrate the adequacy of the square root of OCT intensity as a weight, an example is shown in Fig. 2.12. Figure 2.12(a) shows a bidirectional Doppler image which is stabilized by phase-1 stabilization followed by phase-2 stabilization but with the OCT intensity as a weight. Several vertical line artifacts are evident as indicated by arrows. On the other hand, standard phase-2 stabilization which uses the square root of the OCT intensity as the weight eliminates almost all of these artifacts as shown in Fig. 2.12(b).

2.4.4 Horizontal line artifacts in high-sensitive Doppler OCA images

Several horizontal line artifacts are observed in the high-sensitive Doppler OCA images, such as in Figs. 2.9(b) and 2.10. They appears with the full horizontal transverse width, as indicated by yellow arrows in Fig. 2.10(a). A full-width artifact could occur because of total decorrelation between the B-scans utilized for Doppler processing because of rapid saccadic eye motion. The disconnection of structures across the artifact line is the defining characteristic of this type of artifact.

2.5 Summary

High-penetration Doppler optical coherence tomography and angiography were demonstrated based on a 1-μm SS-OCT. Newly developed phase stabilization algorithm enables high-sensitivity Doppler detection via SS-OCT, without the need for additional calibration hardware. As this method is purely a software method, it can be applied to most SS-OCT devices, without the need for hardware modication. This system was utilized to examine normal eyes The study with normal eyes demonstrated the effectiveness of high-penetration Doppler imaging in the choroid and ONH.

Chapter 3

Noninvasive investigation of Deep Vascular Pathologies of Exuative Macular Disease by HP-ODA*

3.1 Introduction

Exudative macular diseases threaten vision ability of humans. Among them, pathological myopia and age-related macular degeneration (AMD) are representative causes of blindness worldwide [1, 2, 3, 4, 5]. These diseases frequently appear with choroidal neovascularization (CNV). Polypoidal choroidal vasculopathy (PCV) is one form of CNV and it is characterized by a branching vascular network (BVN) terminating in polypoidal lesions [7, 8]. In Asian countries, PCV represents between 56% and 72% of all neovascular AMD patients1.

One of the most effective treatments of CNV is intravitreal injection of bevacizumab or ranibizumab. This treatment requires repeated injection with several rounds with 1- to 3-month periods, and fluorescence angiography (FA) and indocyanine green angiography (ICGA) images are required for the initial diagnosis. However, FA and ICGA imaging is sometimes restricted, because they are invasive methods requiring dye injection into a vein, which makes patients uncomfortable, and sometimes induces adverse reactions [13, 15]. Hence, it is clinically important to establish a new modality that non-invasively reveals the vasculature including abnormal vasculature.

In order to provide a non-invasive alternative angiographic modality, high-penetration Doppler optical coherence angigography (HP-OCA) was developed as described in Chapter 2 [55]. This HP-OCA enables vascular imaging of the deep posterior eye.

The purpose of study in this chapter is evaluating the clinical utility of HP-OCA as a non-invasive angiographic modality. A descriptive case series of myopic CNV (mCNV),

*The portions of this chapter have been published in the following article:
Y.-J. Hong, M. Miura, S. Makita, M. J. Ju, B. H. Lee, T. Iwasaki, and Y. Yasuno, "Noninvasive investigation of deep vascular pathologies of exudative macular diseases by high-penetration optical coherence angiography," Investigative Ophthalmology & Visual Science 54, 3621-3631 (2013).

Patient ID	Eye	Sex	Age	Diopter	Diagnosis	# of IVR
Subject-1	R	M	44.9	-11.0	mCNV	3
Subject-2	L	M	32.8	-5.5	mCNV	0 and 2
Subject-3	L	F	68.5	1.0	AMD (Classic)	0 and 3
Subject-4	L	M	61.5	0.0	AMD (Classic)	0 and 5
Subject-5	L	M	63.1	0.0	AMD (Classic)	0
Subject-6	L	M	54.4	-0.5	AMD (Classic)	0 and 3
Subject-7	L	M	82.3	-0.5	PCV	0
Subject-8	R	M	71.8	-5.0	PCV	0
	L			-5.0	PCV	0
Subject-9	R	M	68.8	1.5	PCV	0
Subject-10	L	M	64.9	-0.5	PCV	0

Table 3.1: R: right, L: left, M: male, F: female, # of IVR: number of intravitreal injection of ranibizumab prior to the investigation with HP-OCA. The multiple numbers in the cell of [# of IVR] represent multiple measurements by HP-OCA after the each number of treatments.

AMD and PCV are presented. Through detailed discussion of the cases, the clinical utility of HP-OCA is also discussed.

3.2 Methods

3.2.1 Subjects

Eleven eyes of 10 subjects were involved in this study as summaries in Table 3.1. The subjects included 2 eyes of 2 subjects with mCNV, 4 eyes of 4 subjects with AMD, and 5 eyes of 4 subjects with PCV. All subjects were Japanese. The mean age of the patients was 61.3 $\pm$ 14.2 (mean $\pm$ standard deviation), and the age ranged from 32.8 to 82.3. Specifically, the mean age of the subjects with each type of disease was 38.8 $\pm$ 8.5 for mCNV, 61.9 $\pm$ 5.8 for AMD and 72.0 $\pm$ 7.5 for PCV. The mean of the spherical equivalent refractive error of the eyes was -2.3 $\pm$ 3.8 D ranging from -11 D to 1.5 D. Specifically, the mean refractive error of the eye for each type of disease was -8.3 $\pm$ 3.9 D for mCNV, 0.1 $\pm$ 0.6 D for AMD, and -1.9 $\pm$ 2.9 D for PCV.

The patients were diagnosed at Ibaraki Medical Center Hospital, Tokyo Medical Uni-

versity. All subjects received a comprehensive ophthalmic examination including color fundus photography, spectral domain OCT with an 830-nm probe (3D OCT-2000, Topcon Corp., Tokyo, Japan), FA, and ICGA. Subjects who showed an allergic reaction to fluorescein, one of mCNV and one of PCV, did not receive FA. Patients who were diagnosed as exudative macular disease were transferred to an optics laboratory at the University of Tsukuba, where their eyes were scanned with a custom built HP-OCA. The research protocol adhered to the tenets of the Declaration of Helsinki and was approved by the institutional review board of Tokyo Medical University and the University of Tsukuba. Informed consent was obtained from the subjects after providing an explanation of the nature and possible consequences of the research.

3.2.2 Investigation with HP-OCA

HP-OCA employs two measurement modes for two types of Doppler tomography as described in section 2.2.4. The first mode is a bi-directional mode, this mode is sensitive to relatively fast flow; in our particular configuration it was from 1.75 mm/s to 19.2 mm/s (axial velocity) and it provides bi-directional axial flow velocity. A potential drawback of this mode is the relatively high minimum measurable velocity (1.75 mm/s). A flow signal slower than this limit is not detectable. In this clinical study, the bi-directional cross-sectional tomogram, in which the bi-directional Doppler signal overlaid on structural OCT, is denoted as bi-directional Doppler tomogram, while *en face* projection of the squared bi-directional Doppler tomogram is denoted as bi-directional OCA.

The second mode is the high-sensitive mode, this mode is sensitive to relatively slow flow, such as >5.2 μm/s (axial velocity) in our particular configuration. A potential drawback of this mode is relatively low maximum measureable velocity (60 μm/s) for quantitative measurement. A flow signal faster than this limit is wrapped into the measureable Doppler range and appears as a strong but random pattern. Hence this high-sensitive mode is not suitable for qualitative bi-directional measurement, but suitable for high-contrast selective imaging of small vessels. In this mode, the image is displayed in the form of the squared energy of the Doppler signal, and is utilized for small vascular observation with flow-selective contrast. In this clinial study, a high-sensitive Doppler signal overlaid on structural cross-sectional OCT is denoted as high-sensitive Doppler tomogram, and the *en face* projection of the high-sensitive Doppler signal is denoted as high-sensitive OCA.

Square area of 6 mm $\times$ 6 mm was scanned around the pathologic region with two Doppler modes as in section 2.2.4. It should be noted that a finally obtained *en face* OCA image of high-sensitive mode is not always perfectly rectangle. This is because of invalid A-lines caused by high-frequency scanning of a scanning mirror in the OCT scanner and its resulting synchronization imperfection between the scanning mirror and data acquisition.

3.2.3 Clinical ophthalmic image and HP-OCA comparison

Figure 3.1 shows typical images of *en face* OCA (Fig. 3.1e and 3.1f), OCA tomogram (Fig. 3.1g and 3.1h) and corresponding color fundus (Fig. 3.1a) and ICGA (Fig. 3.1b and 3.1c) images, which were obtained from a normal macula of a 37-year-old Japanese male with -6.0 D myopia. The *en face* OCT projection image (Fig. 3.1d) was obtained

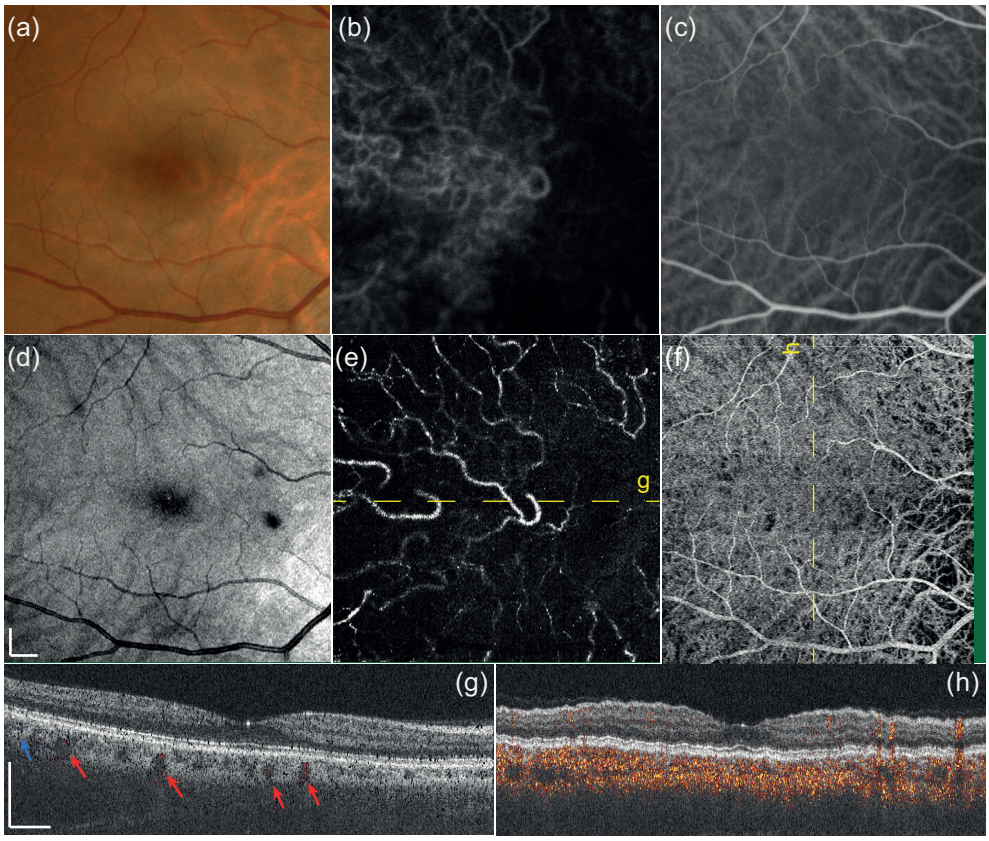

Figure 3.1: Macular images of a normal eye with -6.0 D myopia of a 37-year-old Japanese male. (a) is a color fundus photograph, (b) and (c) are early-phase and mid-phase ICGA images, respectively, and (d) is an *en face* projection of structural OCT. (e) and (f) are bi-directional and high-sensitive OCAs, respectively. (g) and (h) are bi-directional and high-sensitive Doppler tomogram, respectively. Scale bars in (d) and (g) indicate 0.5 mm.

by the depth average of the logarithmic OCT. Thick choroidal vessels were observed with moderate hypo-scattering in the OCT *en face* projection (Fig. 3.1d); however, the visualization of choroidal vessels were limited compared to the mid-phase of ICGA (Fig. 3.1c). Bi-directional OCA (Fig. 3.1e) and high-sensitive OCA (Fig. 3.1f) showed different vasculatures. The retinal vasculature of the macular region was rarely imaged with bi-directional OCA, while high-sensitive OCA visualized similar retinal vasculature to that of color fundus photograph and the mid-phase of ICGA. For imaging of the choroidal vasculature, the bi-directional OCA showed mainly thick choroidal vasculatures that had fast axial blood flow and appeared in the early-phase of ICGA (Fig. 3.1b), while high-sensitive OCA showed a similar choroidal vasculature to that of the mid-phase of ICGA. In addition, several choroidal vessels that did not appear in the mid-phase ICGA were also visualized in the high-sensitive OCA.

The depth locations of the blood flow are identifiable in Doppler tomogram. In bi-directional Doppler tomogram (Fig. 3.1g), red and blue color represent axial flow directions to the anterior or to the posterior, respectively, and the locations of the flow are indicated with arrows. Fig. 3.1h is a vertical high-sensitive Doppler tomogram. The weaving appearance in this Doppler tomogram was caused by imperfect axial motion correction among the horizontal frames.

3.3 Results

3.3.1 Case-1: Myopic choroidal neovascularization (mCNV)

Fig. 3.2 shows a case of mCNV. The subject was a 45-year-old man who had been received intravitreal ranibizumab injection three times prior to the HP-OCA examination (Subject-1 in Table 3.1). Fig. 3.2a, 3.2b and 3.2c represent the color fundus, FA (late-phase) and ICGA (mid-phase) images, respectively, corresponding to the area of the HP-OCA examination.

RPE elevation was observed in structural OCT (Fig. 3.2f), which was simultaneously obtained with bi-directional tomogram as well as in the high-sensitive Doppler tomogram as indicated by yellow arrows (Fig. 3.2g). In high-sensitive Doppler tomogram, abnormal Doppler signals were observed in the sub-RPE space beneath the elevated RPE and above Bruchs membrane as indicated by a red arrow.

The region of RPE elevation appeared with hyper-scattering in *en face* structural OCT (Fig. 3.2d) and with hyper-Doppler signals in high-sensitive OCA as indicated by arrows (Fig. 3.2e). These signals were co-located with the hyper-reflective spot in the color fundus (an arrow in Fig. 3.2a) and the hyper-fluorescence signal in FA (an arrow in Fig. 3.2b), which is the indicator of inactive CNV. The hyper-scattering in the structural OCT projection was surrounded by a hypo-scattering rim, as a similar appearance was shown in the color fundus. Similarly, the hyper-Doppler spot in the *en face* OCA was surrounded by a hypo-Doppler rim, which was similar to a pattern that appeared in the ICGA image (an arrow in Fig. 3.2c). The pattern of CNV appearance in the *en face* structural OCT and OCA was found in 2 of 2 cases with mCNV, 4 of 4 cases with AMD, and 1 of 4 cases with PCV. It is also noteworthy that high-sensitive OCA showed a high overall similarity

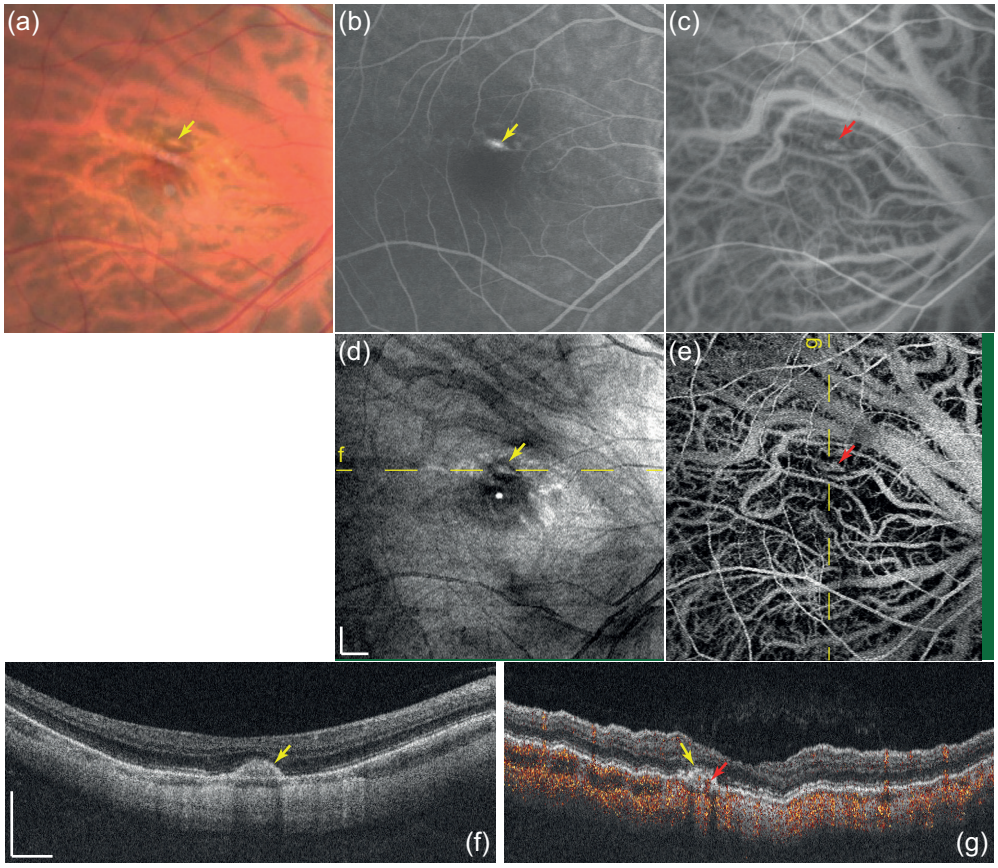

Figure 3.2: Right macular images of a 45-year-old man with mCNV, (a) color fundus, (b) FA (late-phase), (c) ICGA (mid-phase), *en face* projections of (d) structural OCT and (e) high-sensitive OCA, (f) structural OCT taken by a scanning protocol of bi-directional mode and (g) high-sensitive Doppler tomogram. Yellow dashed line in (d) and (e) indicate the location of tomograms of (f) and (g), respectively. Scale bars in (d) and (f) indicate 0.5 mm.

to the mid-phase of ICGA.

3.3.2 Case-2: mCNV with ranibizumab injection

Figure 3.3 summarizes another case with mCNV. The subject was a 33-year-old man who was treated with intravitreal ranibizumab injection (0.05 ml of 10 mg/ml solution for each injection) two times with a 28-day separation (Subejct-2 in Table 3.1). HP-OCA examination was performed 6 days before the first injection and 59 days after the second injection.

Figures 3.3a, 3.3b and 3.3c are mid-phase ICGA, high-sensitive OCA, and *en face* structural OCT projection taken before the treatment, respectively. Fig. 3.3d, 3.3e and 3.3f are corresponding images taken after the injection. The CNV was observed as a

hyper-fluorescent region surrounded by a dark rim in the ICGA image (red arrow in Fig. 3.3a) before the treatment. This CNV area became smaller after the ranibizumab injection (red arrow in Fig. 3.3d). This CNV appeared as a hyper-Doppler region surrounded by a dark rim in the OCA image (red arrow in Fig. 3.3b), and it also became smaller after the ranibizumab injection (red arrow in Fig. 3.3e). This appearance was well correlated with ICGA. This CNV region appeared as a large hyper-scattering region in *en face* OCT (a circle in Fig. 3.3c), and this region became smaller after the injection (a circle in Fig. 3.3f).

Figures 3.3g and 3.3h are vertical high-sensitive Doppler tomograhies. These tomograhies were created from the same datasets of Fig. 3.3b and 3.3c, and Figs. 3.3e and 3.3f, respectively, and the locations of the tomograms are indicated by dashed lines in the *en face* images. Note that the vertical gap in Fig. 3.3g was created by an eye blink. Before the ranibizumab injection, subretinal fluid (blue arrow) and exudates (yellow arrow) were evident in the structural OCT (Fig. 3.3g). The RPE in the exudative region was hardly visible. In addition to structural tomogram, Doppler tomogram provided more detailed insight. Hyper-Doppler signals were observed in the exudates and the choroid beneath the exudates (a red arrow in Fig. 3.3g), which indicated abnormal flow in this region. After ranibizumab injection, as shown in Fig. 3.3h, sub-retinal fluid disappeared and the CNV related elevation became smaller. The RPE became clearly visible with structural OCT. With Doppler tomogram, it was found that the abnormal blood flow disappeared (Fig. 3.3h).

3.3.3 Case-3: Age-related macular degeneration (AMD)

Figure 3.4 summarizes a case of AMD with classic CNV. The subject was a 62-year-old man (Subject-4 in Table 3.1). An active CNV was observed at the fovea by dye leakage in the late-phase of FA (arrow in Fig. 3.4b). The mid-phase of ICGA (Fig. 3.4c) shows CNV that appeared as hyper-fluorescence surrounded by a dark rim (arrow). Several hard drusen were observed in the color fundus as white spots (Fig. 3.4a).

OCT *en face* projection (Fig. 3.4d) shows a similar appearance to the color fundus photograph including hyper-scattering spots and choroidal vasculatures. It is noteworthy that the choroidal vasculature around the CNV appeared with hyper-scattering signal (red arrow inside a circle), while other choroidal vessels in non-pathologic regions generally appeared with hypo-scattering, as indicated by a yellow arrow. This appearance would be caused by the deeper penetration beneath the choroidal vessels around the CNV, as indicated by red arcs in the horizontal structural OCT cross-section taken with the bi-directional scanning protocol (Fig. 3.4f).

High-sensitive OCA (Fig. 3.4e) showed almost all of the retinal and choroidal vessels shown in the mid-phase of ICGA ((Fig. 3.4c) even with higher contrast. Remarkably, the detailed abnormal choroidal vasculature was observed at the CNV region, as indicated by a circle in Fig. 3.4e, while it was hardly observed in ICGA.

In high-sensitive Doppler tomogram (Fig. 3.4g), RPE elevation was observed. Remarkably, abnormal Doppler signals were observed beneath the elevated RPE, as indicated by an arrow.

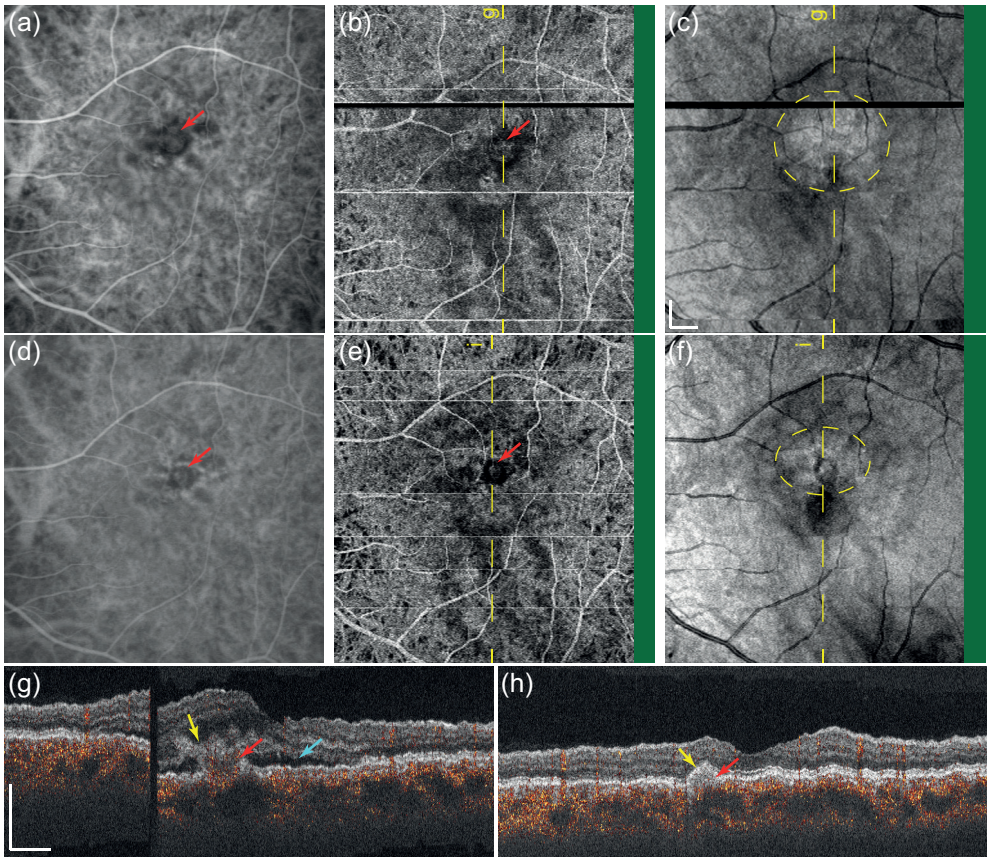

Figure 3.3: Left macular images of a 33-year-old man with mCNV taken before and after the ranibizumab treatment. (a) and (d) ICGAs (mid-phase), (b) and (e) high-sensitive OCAs, (c) and (f) *en face* structural OCT projections taken with the high-sensitive scanning mode, and (g) and (i) high-sensitive Doppler tomograms. (a)-(c) and (g) were taken before treatment and (d)-(f) and (i) were taken after treatment. Scale bars in (c) and (g) indicate 0.5 mm.

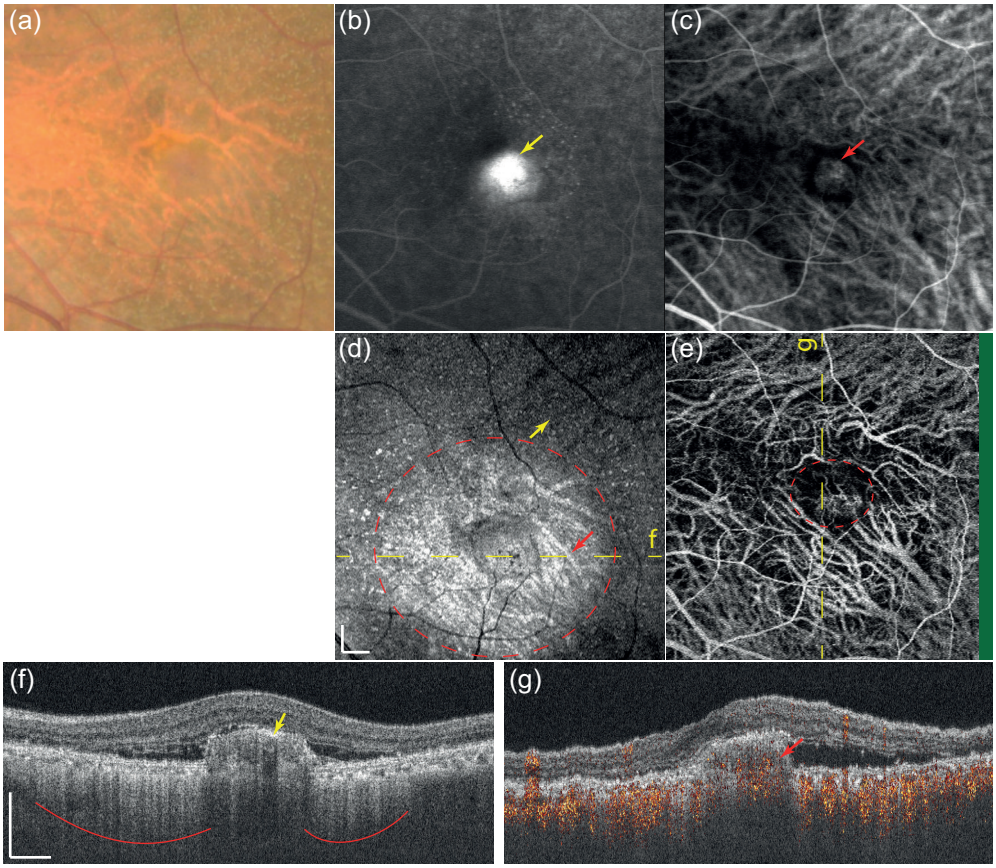

Figure 3.4: Left macular images of a 62-year-old man with AMD, (a) color fundus, (b) FA (late-phase), (c) ICGA (mid-phase), (d) *en face* projection of structural OCT, (e) high-sensitive OCA, (f) structural OCT cross-section taken with bi-directional scanning mode, and (g) high-sensitive Doppler tomogram. Yellow dashed lines in (d) and (e) indicate the locations of (f) and (g), respectively.

3.3.4 Case-4: AMD with ranibizumab injection

Figure 3.5 summarizes another case of AMD with classic CNV. The subject was a 69-year-old woman treated with intravitreal ranibizumab injection 3 times within time periods of 28 days and 35 days (Subject-3 in Table 3.1). The first HP-OCA examination was performed 4 days before the first injection and the second examination was done 49 days after the third injection.

Figures 3.5a3.5d represent late-phase FA, mid-phase ICGA, high-sensitive OCA, and structural OCT projection, respectively, taken before the first injection. Figs. 3.5e3.5h are corresponding images taken after the third injection. The active CNV, indicated by a red arrow in the FA image (Fig. 3.5a) became inactive after three injections, as shown in Fig. 3.5e. In the ICGA images, the CNV appeared as hyper-fluorescence surrounded by a dark rim, as indicated by arrows in Fig. 3.5b and 3.5f. The size of the CNV region was reduced by the injections. A similar appearance with ICGA was found in high-sensitive OCA images, as indicated by arrows in Fig. 3.5c and 3.5g, where a hyper-Doppler signal was surrounded by a hypo-Doppler rim. The size of this appearance was also reduced by the ranibizumab injections.

In *en face* OCT projection (Fig. 3.5d), active CNV appeared with hyper-scattering (red arrow). This hyper-scattering decreased after the ranibizumab injection (red arrow in Fig. 3.5d). In the post-injection OCT image, some other hyper-scattering spots were observed (yellow arrows in Fig. 3.5h). These hyper-scattering spots were well correlated with the hyper-fluorescence of FA (arrows in Fig. 3.5e).

A clear difference was observed between the OCT cross-sections taken before and after the injections. Before the treatment (Fig. 3.5i), exudates were observed as indicated by a yellow arrow. In this region, the RPE was not clearly observed. In the corresponding high-sensitive Doppler tomogram, hyper-Doppler signals were observed in the exudates as indicated by a red arrow in Fig. 3.5j. After the injections, exudates disappeared and only a small RPE elevation was observed (yellow arrow in Fig. 3.5k). In high-sensitive Doppler tomogram (Fig. 3.5l), nearly no abnormal Doppler signal was observed (arrow).

3.3.5 Case-5: Polypoida choroidal vasculopathy (PCV)

Figure 3.6 summarizes a case of PCV that appeared with a large abnormal vascular network. The subject was a 65-year-old man and his left eye was examined (Subject-10 in Table 3.1). The eye was not treated at the time of the examination. Widely spread exudates were observed with white color in the fundus photograph (Fig. 3.6a). The hyper-fluorescent region in the late-phase FA (Fig. 3.6g) indicated a large pigment epithelial detachment (PED). Abnormal vasculature and polypoids were observed in the mid-phase of ICGA (Fig. 3.6c). In *en face* OCT projection (Fig. 3.6d), a strong hyper-scattering (left circle) and a moderate hyper-scattering (right circle) were observed. This corresponded to the hyper-fluorescence regions in FA (Fig. 3.6g).

In bidirectional Doppler tomogram (Fig. 3.6h), clear Doppler signals were observed beneath the moderate PED (red arrow). Fig. 3.6e shows the bi-directional OCA, where the red arrow indicates the Doppler signal in Fig. 3.6h. When comparing this OCA and early phase ICGA (Fig. 3.6b), it is evident that this Doppler signal corresponds to a feeder

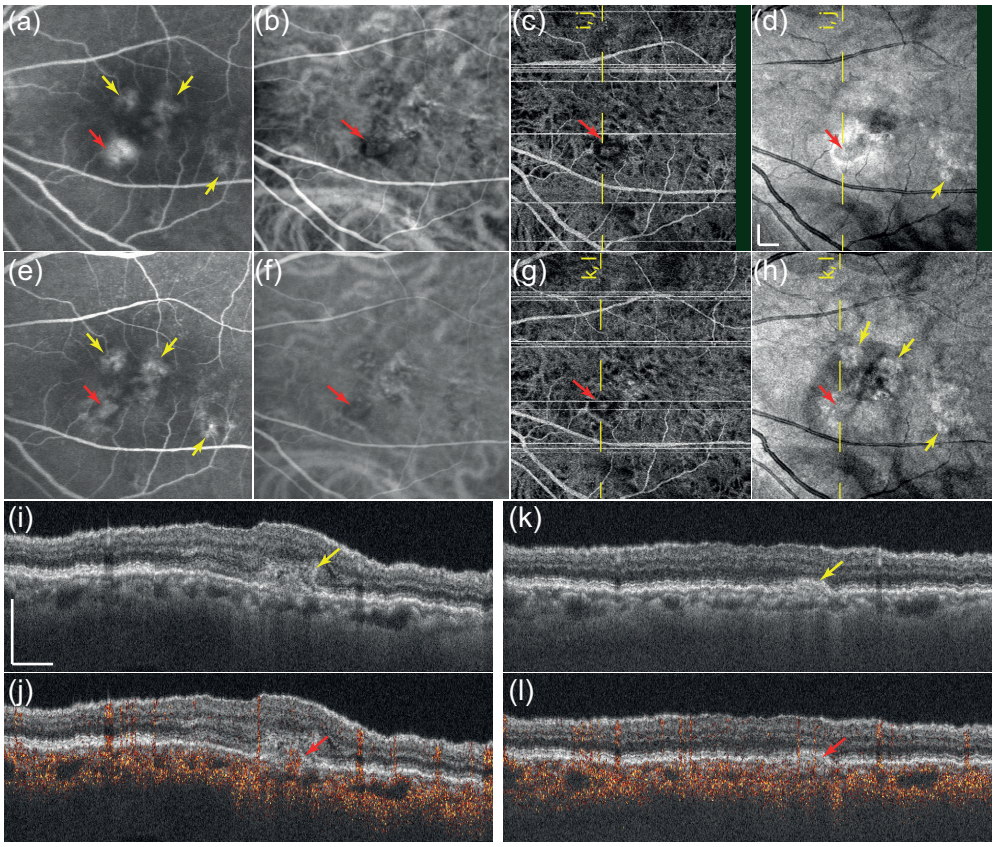

Figure 3.5: Left macular images of a 69-year-old woman with AMD taken before and after the three times of intravitreal ranibizumab injection. (a) FA (late-phase), (b) ICGA (mid-phase), (c) high-sensitive OCA, and (d) *en face* structural OCT projection images taken using the high-sensitive scanning mode before the first ranibizumab injection. (e)(h) are corresponding images taken after the third ranibizumab injection. (i) and (j) are structural OCT and high-sensitive Doppler tomogram taken before the first injection. The locations of these tomograms are indicated by yellow lines in (c) and (d). (k) and (l) are those taken after the third injection. The yellow lines in (g) and (h) indicate the location of these tomograms. Scale bars in (d) and (i) indicate 0.5 mm.

vessel.

In high-sensitive Doppler tomogram (Fig. 3.6i), many abnormal Doppler signals were observed beneath the PED as indicated by the red arrows. Remarkably, some Doppler signals, such as that indicated by the leftmost arrow, represented abnormal vessels that penetrated Bruchs membrane into the sub-RPE space. The high-sensitive OCA (Fig. 3.6f) shows a highly correlated pattern with the mid-phase of ICGA (Fig. 3.6c).

3.3.6 Case-6: PCV with volumetric polypoidal CNV

Figure 3.7 summarizes another case of PCV. The subject was a 69-year-old man (Subject-9 in Table 3.1). The early-phase of ICGA (Fig. 3.7a) shows a clear branching vascular network (BVN) at the PED area. The late-phase of ICGA (Fig. 3.7d) shows terminal aneurismal dilatation of the BVN. High-sensitive OCA (Fig. 3.7b) shows a highly correlated vascular pattern including the BVN with the early-phase of ICGA. High-sensitive Doppler tomogram (Fig. 3.7g) presents several Doppler signals beneath the PED (arrows). The location of this Doppler tomogram is indicated on ICGAs (Fig. 3.7a and 3.7d) and *en face* OCA (Fig. 3.7b) with yellow lines. This indicates that the Doppler signals beneath the PED in Fig. 3.7g are associated with the BVN.

A volume rendering of the high-sensitive OCA provides more intuitive understanding, as shown in Fig. 3.7e, where the Doppler signal and the structural OCT signal are respectively displayed in orange and green colors. In this image, the comprehensive three-dimensional structure of the BVN is clearly visualized. In addition, a blood vessel connecting the BVN to the choroid is clearly observed as indicated with an arrow.

An active CNV is observed in FA, as indicated by a circle in Fig. 3.7c. A similar pattern is observed in high-sensitive OCA (Fig. 3.7b) and OCT *en face* projection (Fig. 3.7f) with hyper-Doppler and hyper-scattering, respectively. Corresponding Doppler signals are observed in the choroid under the PED (arrow in Fig. 3.7h).

3.3.7 Visibility of Doppler Signals at abnormal chroidal vessels

Two graders (YJH and MM) graded the visibility of abnormal Doppler signals. A fly-through sequence of structural OCT, Doppler tomogram, and the Doppler tomogram overlaid on the structural OCT were presented to the graders. In this grading, the eyes with Doppler signals at abnormal regions found in structural OCT were labeled as positive and the other eyes were labeled as negative. This grading was independently done for the following three regions; (1) an abnormal region anterior to the RPE, (2) a region between the RPE and Bruchs membrane, and (3) within Bruchs membrane, i.e., Doppler signal penetrated through Bruchs membrane.

Table 3.2 summarizes the occurrence of Doppler signals at abnormal choroidal vessels graded by two graders and their agreements. In this table, the three regions described above were denoted as above RPE, RPE-Bruch, and in Bruch. The three numbers in each cell represent, from the left, the number of positive eyes found by grader YJH, that found by grader MM, and the number of eyes in which the grading of the two graders are agreed.

With bi-directional Doppler tomogram, abnormal flows were observed in PCV eyes with 80% by grader YJH and 60% by MM. Conversely, no abnormal flow was observed

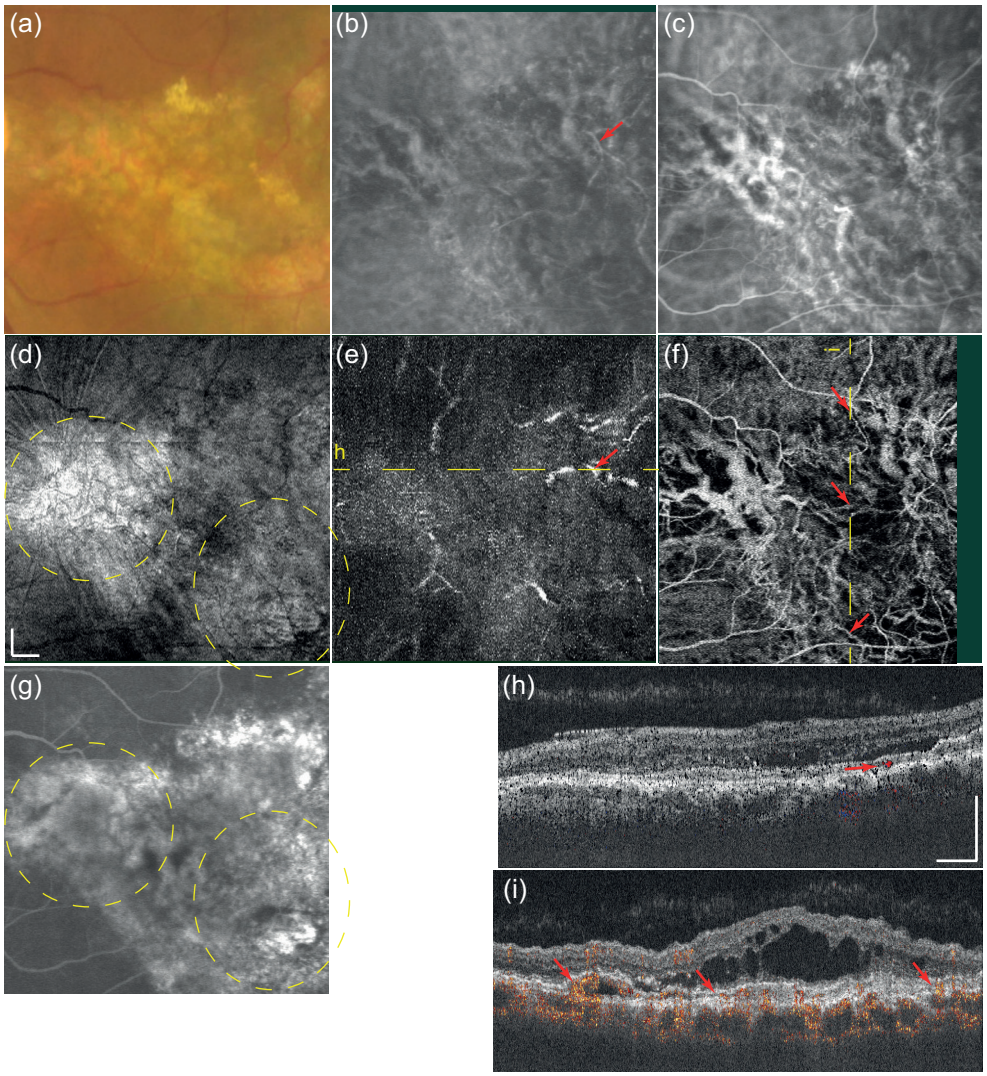

Figure 3.6: Left macular images of a 65-year-old man with PCV with a large area of polypoid, (a) color fundus photograph, (b) early-phase of ICGA, (c) mid-phase of ICGA, (d) *en face* projections of structural OCT, (e) bi-directional OCA, (f) high-sensitive OCA, (g) late-phase of FA, (h) bi-directional Doppler tomogram, and (i) high-sensitive Doppler tomogram. Yellow dashed lines in (e) and (f) indicate the location of (h) and (i), respectively. Scale bars in (d) and (h) indicate 0.5 mm.

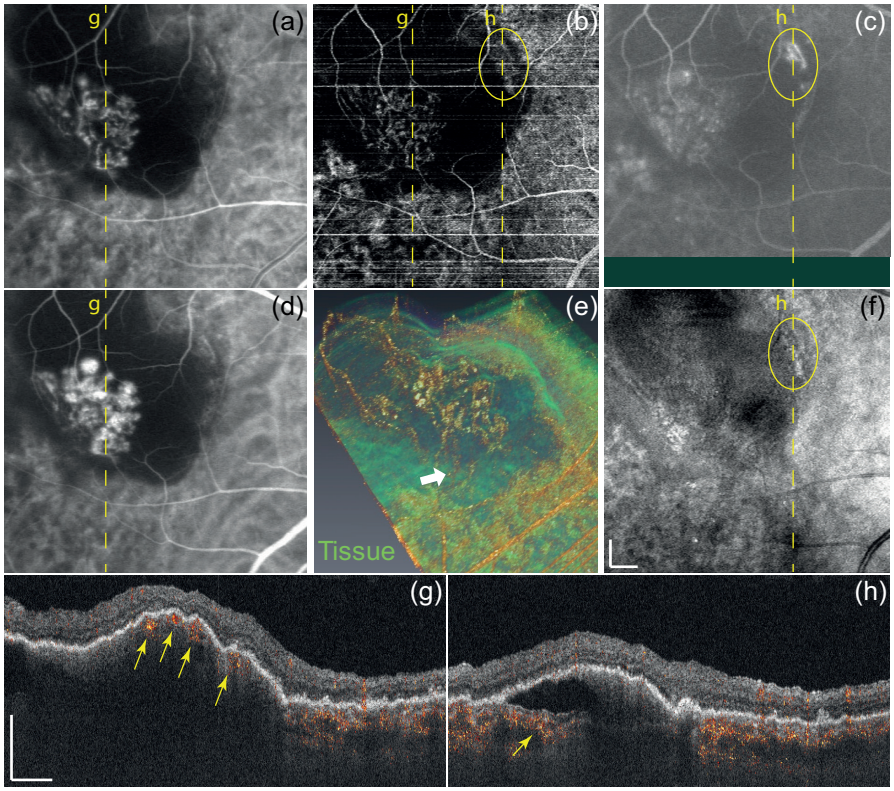

Figure 3.7: Right macular images of a 69-year-old man with PCV with a clear BVN. (a) early-phase and (d) late-phase ICGA, (b) high-sensitive OCA, (e) volume rendering of high-sensitive three-dimensional Doppler tomogram, (c) late-phase FA, (f) *en face* projection of structural OCT. (g) and (h) are high-sensitive Doppler tomograms. The location of (g) is indicated by dashed lines in (a), (b), and (d), while the location of (h) is indicated by yellow lines in (b), (c), and (f). Scale bars in (f) and (g) indicate 0.5 mm.

Doppler mode	Region	Untreated			Treated	
		mCNV (N=1)	AMD (N=4)	PCV (N=5)	mCNV (N=2)	AMD (N=3)
Bi-directional mode	Above RPE	0, 0, 1	0, 0, 4	0, 0, 5	0, 0, 2	0, 0, 3
	RPE-Bruch	0, 0, 1	0, 0, 4	4, 3, 4	0, 0, 2	0, 0, 3
	In Bruch	0, 0, 1	0, 0, 4	2, 1, 2	0, 0, 2	0, 0, 3
High-sensitive mode	Above RPE	1, 1, 1	3, 3, 4	0, 0, 5	0, 0, 2	0, 0, 3
	RPE-Bruch	0, 0, 1	1, 1, 4	5, 5, 5	1, 2, 1	1, 2, 3
	In Bruch	1, 1, 1	4, 4, 4	4, 5, 4	1, 1, 2	1, 2, 3

Table 3.2: A summary occurrence of Doppler signals in bi-directional and high-sensitive Doppler tomograms. The values in each cell, from the left, represent the number of eyes in which the Doppler signal was found by grader YJH, that found by MM, and agreement between two graders. N is the number of eyes. Three regions are defined as: (1) an abnormal region anterior to the RPE (above the RPE), (2) a region between the RPE and Bruchs membrane (RPE-Bruch), and (3) within Bruchs membrane (in Bruch), in which case a Doppler signal penetrated through Bruchs membrane

in mCNV and AMD cases. High-sensitive OCA showed a high occurrence of abnormal Doppler signals within the untreated eyes with both graders. The grading of the two graders were perfectly agreed except the following three cells; the bi-directional Doppler of untreated PCV at the RPE-Bruch and in Bruch region, high-sensitive Doppler of untreated PCV at the In Bruch region, and high-sensitive Doppler of mCNV at the RPE-Bruch region. And hence, the overall agreement of all cells in Table 3.2 was 89% (82/90).

3.4 Discussion

In the *en face* OCT projections of 1 eye with AMD (Fig. 3.4d) and 2 eyes of a single case of PCV, the choroidal vessels appeared with hyper-scattering at the pathologic regions, while it appeared with hypo-scattering in non-pathologic regions. It is also known that, the choroidal vessels appeared with hypo-scattering in the *en face* OCT projection of normal eyes. In these pathologic regions, abnormal hyper-penetration to the deep choroid and sclera was observed as exemplified in Fig. 3.4f. This hyper-scattering could be explained by abnormality in the choroidal or RPE tissue, such as reduction of melanin content, abnormal thinning of the choroid or both. The hypo-scattering appearance of choroidal vessels can be utilized as an indicator of the choroidal abnormality.

Since the bidirectional mode is only sensitive to fast blood flow, it is selectively sensitive to the arteries among the choroidal vessels. This property of the bidirectional mode provides a similarity between bidirectional OCA and the early-phase (arterial phase) of ICGA as exemplified in Figs. 3.1b and 3.1e. For ICGA imaging of the PCV, feeder

vessels were imaged at the early phase. It would be expected that the feeder vessels can be visualized by bidirectional OCA. In the current study, bidirectional OCA visualized choroidal vessels beneath or close to the PED in 3 of 5 PCV eyes to both graders. These choroidal vessels were correlated with the feeder vessels that appeared in early-phase ICGA. This indicates the utility of bidirectional OCA for noninvasive imaging of feeder vessels of PCV.

The high-sensitive OCA of PCV cases visualized the three-dimensional (3-D) structure of the BVN and polypoids. It is known that a cluster of abnormal vessels are co-localized in some region beneath the PED and a feeder vessel connects the abnormal vessel cluster and a choroidal vessel [8].

The abnormal vessel cluster of PCV has been investigated by structural OCT with a 830-nm probe beam [8], structural high-penetration OCT with a 1-m probe beam [70], and Doppler OCT with a 840-nm probe beam [82]. However, none of them has been used to visualize the comprehensive 3-D structure of PCV including the vessels cluster and the feeder vessel. As exemplified by Fig. 3.7d, high-sensitive OCA has enabled comprehensive visualization of the 3-D structure of the PCV including the vessel cluster and the feeder vessel. This comprehensive investigative ability of high-sensitive OCA can provide a detailed understanding of the pathology.

The appearance of a high-sensitive Doppler *en face* projection image is generally well correlated with mid-phase ICGA, as exemplified in Figs. 3.1c and 3.1f, Figs. 3.2c and 3.2e, Figs. 3.3a and 3.3b, Figs. 3.3d and 3.3e, Figs. 3.4c and 3.4e, Figs. 3.5b and 3.5c, Figs. 3.5f and 3.5g, and Figs. 3.6c and 3.6f. The CNV appearance with high-sensitive OCA was also similar to that of ICGA. Furthermore, in some cases, such as shown in Figs. 3.4, 3.6, and 3.7, high-sensitive OCA provided higher contrast than ICGA.

In this study, FA images showed leakages in some untreated cases including 1 eye with mCNV, 4 eyes with AMD and 1 eye with PCV. The number of leakages was 6 in total. In all leakage spots, a similar pattern was observed in *en face* high-sensitive OCA as exemplified in Figs. 3.2b and 3.2e, Figs. 3.4b and 3.4e, Figs. 3.5a and 3.5c, and Figs. 3.7c and 3.7b. The leakage in FA is an indicator of abnormal penetration of a choroidal vessel into the retina, while the Doppler OCT, and hence OCA, is sensitive to localized motion and selectively contrasts the structure of the blood vessels. Although, the leakage is not directly detectable by OCA, its related structural abnormality can be detected. And hence, high-sensitive OCA has indirectly indicated the region of the leakage. Because of the difference in the contrast mechanism, OCA cannot be the full alternative for FA. However, the high correlation between OCA and FA and non-invasive nature of OCA would make OCA a comparable utility to FA.

While FA and ICGA use fluorescent dye as a vessel contrast agent, HP-OCA uses blood flow as a contrast source. The different vessel contrast mechanism between conventional angiography and HP-OCA would result in different characteristics. FA and ICGA have advantages of time elapse imaging after dye injection and investigation of tissue damage through dye leakage. Conversely, OCA has the two major advantages of 3-D investigation and non-invasiveness. The 3-D visualization of the ocular vasculature would provide more detailed insight of the pathology. The non-invasiveness enables safe and repetitive application of OCA to the patient. This repetitive examination is particularly useful for the

frequent monitoring of the outcome of treatments. This could provide insights in natural history and response to the treatment of retinal illness. In addition, OCA can be also utilized for mass-screening not only for the specific clinical diagnosis and the time-sequence monitoring.

Since HP-OCA provides vast amount of information including a structural OCT volume and two types of Doppler OCT volumes, a conventional static-page-oriented patient report is not always convenient for clinicians. Alternatively, a sophisticated data browser is necessary. Figure 3.8 shows a screen shot of our custom made HP-OCA browser. It consists of an en face projection image of structural OCT and en face Doppler OCA in its left column, while cross-sectional images of structural OCT, Doppler tomogram, and the Doppler tomogram overlaid on the structural OCT are displayed at the right column. An operator is allowed to quickly find the point of pathology in the en face images. By pointing the position of pathology in the en face images with a line cursor, corresponding cross-sections are displayed in the right column. Hence the operator can utilize both the structural OCT projection and en face OCA to quickly find the pathologic region. This simultaneous usage of the structural projection and en face OCA reduces the risk of overlooking of pathologies in comparison to a conventional OCT. The operator is also allowed to markup one of the cross-sectional images. As marking up an image, the same mark simultaneously appears at the same location in the other cross-sectional images. This function enables quick co-registration of structural and Doppler findings. By using a well-designed data browser, such as this HP-OCA browser, the operator can quickly and effectively review the huge amount of information provided by HP-OCA.

In this study, I demonstrated vasculature imaging of exudative macular diseases by HP-OCA. HP-OCA provided two measurement modes; i.e. bidirectional OCA and high-sensitive OCA. With bi-directional OCA, feeder vessels of the PCV were successfully visualized. Conversely, the high-sensitive OCA provided similar angiograms to the mid-phase of ICGA with higher contrast. This new modality can be partially utilized as an alternative to FA and ICGA. In addition, the non-invasive and 3-D rendering imaging ability of OCA enables wider applications than FA and ICGA.

3.5 Summary

HP-OCA revealed depth-resolved abnormal vasculatures in exudative macular diseases. The *en face* HP-OCA images showed high similarity with FA and ICGA images. These results suggest HP-OCA can be used for non-invasive and three-dimensional angiography in a clinical routine.

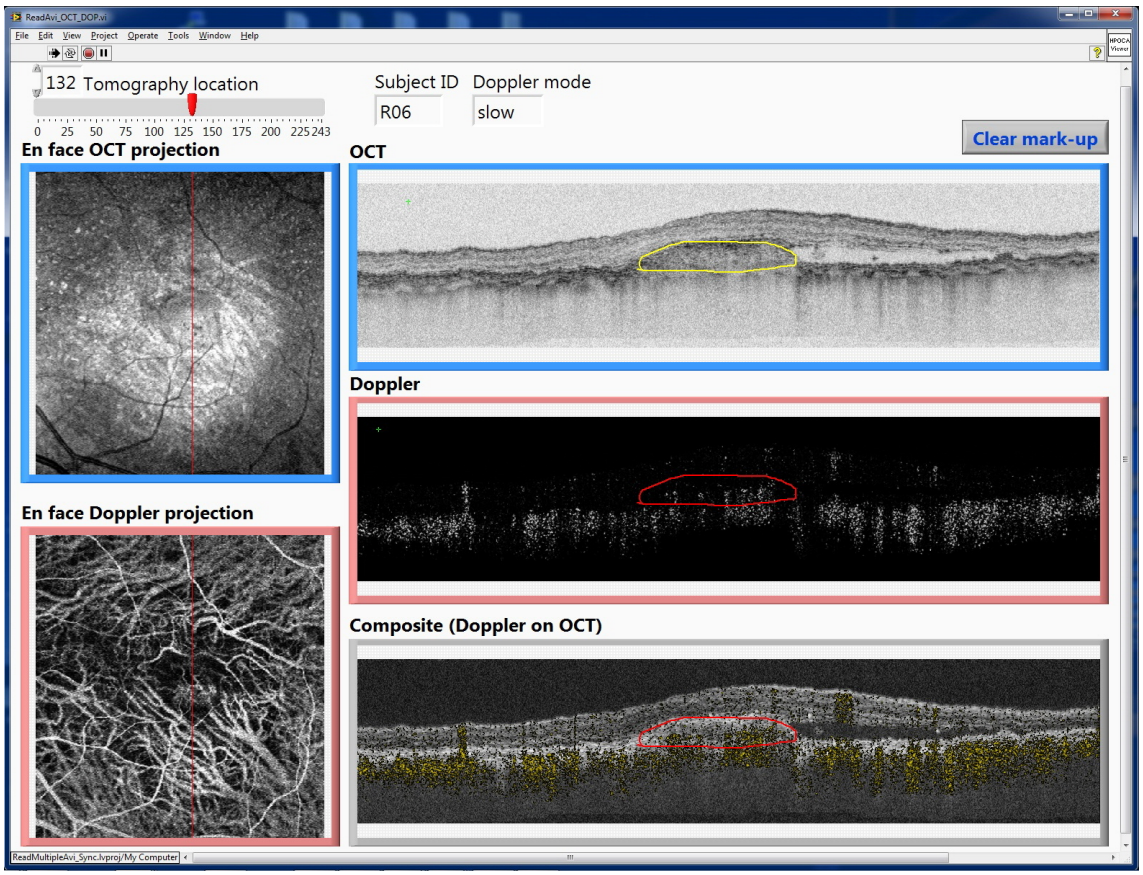

Figure 3.8: A screen shot of a custom-made HP-OCA data browser. The *en face* projection of structural OCT and *en face* Doppler OCA are displayed at the left column and the cross-sectional structural OCT, Doppler tomogram, and the Doppler tomogram overlaid on the structural OCT are displayed in the right column. As pointing the position of interest in the *en face* images by a red line cursor, the corresponding cross-sectional images are simultaneously displayed in the right column. The operator can mark up one of the cross-sections, and the same mark simultaneously appears at the same positions of the other cross-sections.

Chapter 4

Multi-Functional Imaging of the Posterior Eye*

4.1 Introduction

Several ocular diseases are related with abnormalities of retinal pigment epithelium (RPE) as well as the abnormalities of choroidal blood circulation. This is because the nutrition trasnfer and waste excretion are done through choroidal vessels for retina and RPE plays a significant role in metabolism between retina and choroid [16]. And RPE also absorbs excess light for better vision, maintains the excitability of photoreceptor outer segment (POS), help the regeneration of POS by phagocyte the end of POS. Any disturbance of the RPE can lead to severe visual impairment.

A direct visualization of the RPE would be considerable diagnostic value. OCT image of normal eye which doesn't have disorder shows three closely spaced hyper-scattering layer between retina and choroid in the macular region. And the most bottom layer is the RPE. However, when there is retinal disorder, it is not easy to distinguish the RPE layer or its existence because the boundaries of three layers are not clear. It is known that PRE cells contain melanin granules [83, 84] and they have polarization scrambling property. In order to contrast RPE and to examine the integrity of RPE, PS-OCT techonology was utilized to calculate polarization uniformity [47, 85, 86, 87].

Jones-matrix-based OCT [88, 38, 35, 36] has been developed as one of the PS-OCT variations. It is known that the Jones-matrix OCT has high intrinsic robustness for the measurement of polarization properties of biological samples. However, polarization multiplexing was required for the polarization diversity detection in Jones-matrix OCT, And active optical components, such as electro-optic or acousto-optic modulator, has been utilized to change the input polarization state [35, 36, 89]. Recently, a passive-component-based Jones matrix OCT system was demonstrated [57, 90]. This system realized Jones matrix measurements without any active optical components.

*The portions of this chapter have been published in the following article:
Y. Lim, Y.-J. Hong, L. Duan, M. Yamanari, and Y. Yasuno,"Passive component based multifunctional jones matrix swept source optical coherence tomography for doppler and polarization imaging," Optics Letters 37, 1958-1960 (2012).

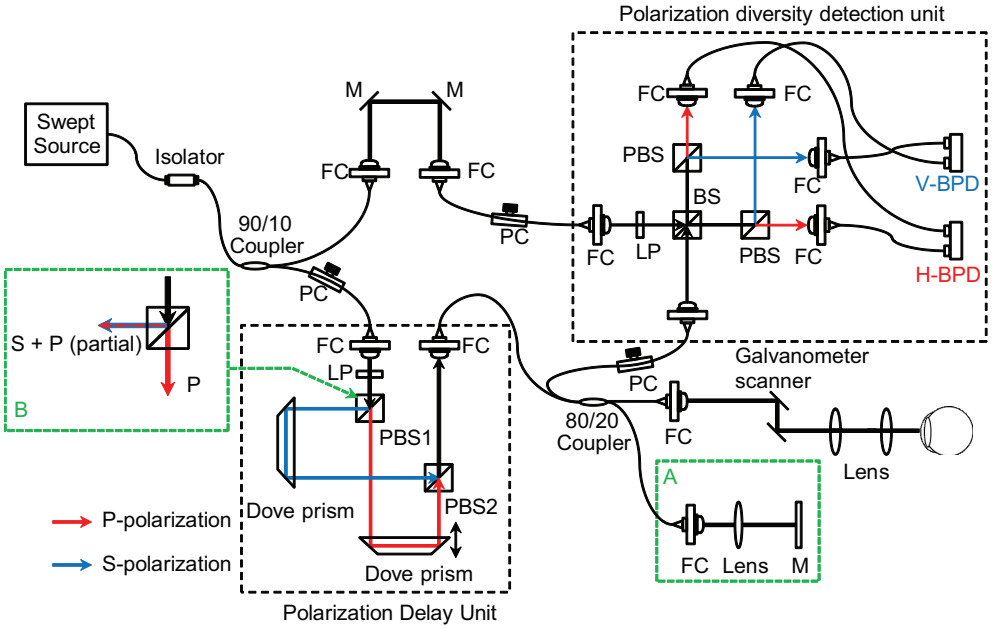

Figure 4.1: Schematic diagram of Jones-matrix OCT system. LP: linear polarizer, PC: polarization controller, FC: fiber collimator, M: mirror, PBS: polarization beam splitter, BS: beam splitter, H- and V-BPD: balanced photo-detector for horizontally and vertically polarized signals, respectively.)

HP-OCA was extended to multi-functional OCT (MF-OCT). In particular, a fiber-based passive-component Jones matrix swept-source OCT (JM-OCT) [57] was utilized and simultaneous Doppler and polarization-sensitive measurement was implemented for the vasculature and RPE discriminable imaging. Preliminary descriptive case series of geographic atrophy (GA), AMD, and PCV are presented.

4.2 Jones matrix OCT

4.2.1 JM-OCT configuration

As shown in Fig. 4.1, the JM-OCT is built with an MEMS-based swept-source (Axsun Technologies Inc., Massachusetts) which has center wavelength of 1.06 μm with full width at half maximum of 111 nm and 100 kHz sweeping rate. Entire wavelength scanning width is 123 nm and the average output power is 30 mW.

The interferometer is built with single-mode optical fiber (HI 1060, Corning). The light is split by a 90/10 fiber coupler after passing through an isolator. 90 % portion of laser output is guided to a passive component polarization delay unit of probe-arm, and 10 % portion of laser output is guided to a reference arm.

The light passed the polarization delay unit is splitted by 80/20 fiber coupler, the 20 % portion of light is guided to a custom-built retinal scanner for the illumination of eye, and the 80 % portion of light is guided to a calibration refrlector (dashed green box-A in

Fig. 4.1. Retinal scanner is composed with a fiber collimator (F280 APC-C, Thorlabs Inc., NJ), a two-axis galvanometer scanner, two objective lenses (f=60 mm), and an aspheric ophthalmic lens (40D, Volk Optical Inc., OH). The beam diameter incident on the cornea and retin were around 1.4 mm and 21 μm,respectively. The optical power on the cornea is 1.15 mW in current alignment, it is satisfy the saftey regulation defined by ANSI [76]. The back-scattered light from the retina is recoupled to the 80/20 fiber coupler and 80 % portion is guided to a polarization diversity (PD) detection unit.

The PD detection unit compose of a lnear polarizer, a beam splitter (BS), two polarizing beam splitters (PBSs), and 350 MHz two balanced photo-detectors (BPDs, PDB430C, Thorlabs Inc.). The reference light from reference arm guided to pass a 45 ° oriented linear polarizer for the polarization balancing between two polarization diversity channels. In the PD detection unit, the reference and back-scattered light from the eye is combined at the BS, splitted into horizontal and vertical polarization components by the two PBSs, and finally detected by the PBDs. The detected signals from the BPDs were samppled by an digitizer (ATS9350, AlazarTech Inc., QC, Canada) with 12-bit resolution and a sampling rate of 500 MHz after passing through a high-pass (1 MHz) and low-pass (250 MHz) filter (HP1CH3-0S and LP250CH3-0S, R&K Co. Ltd. Shizuoka, Japan). The sampled interference signals were rescaled to the linear frequency domain using pre-defined rescaling parameters determined by a time frequency calibration method [91]. The rescaling algorithm also cancels the spectral shift among A-lines and stabilizes the phase of the OCT signal.

With an average probe power of 1.15 mW, the sensitivity and signal roll-off were to be 91.05 dB and -0.65 dB/mm, respectively. Because the signal energy is split into the four OCT images, the sensitivity of the system measured for a single image is 6-dB lower than that of standard OCT.

4.2.2 Incident polarization multiplexing by polarization delay unit

A passive polarization delay unit is utilized to multiplex two incident polarization states by applying optical path lengths difference (OPLD). As shown in Fig. 4.1, the passive polarization delay unit consists of a linear polarizer, two PBSs, and two Dove prisms. In this delay unit, the collimated light is passing through the linear polarizer oriented at 45 ° and splitted into two orthogonal polarization components by the PBS 1. After the internal reflection in the Dove prisms, the two orthogonally polarized lights were combined by the PBS 2, and then coupled to a optical fiber connected to the the 80/20 fiber coupler.

By the OPLD, the two incident polarization states are multiplexed in depth positions, and the OPLD is adjusted by moving one of the Dove prisms. In our particular setup, the OPLD is adjusted to be $z_d = 3.1$ mm, so two OCT signals corresponding to the two multiplexed incident polarization states appear with a depth separation of 3.1 mm. With this configuration, the measurable imaging depth range for each signal was determined to be around 2.95 mm, which is large enough for clinical imaging of pathologic posterior eyes.

Since this polarization delay unit is compact in size and consists only bulk optical components, the perturbation of the delay caused by temperature fluctuation is negligible.In

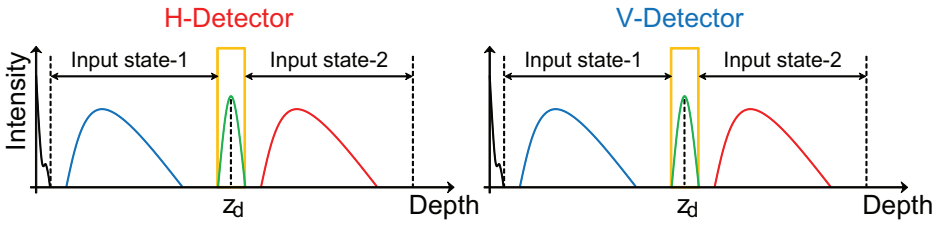

Figure 4.2: Diagram of the Fourier transformed interference signals from horizontal (H) and vertical (V) detection channels.

addition, this polarization delay unit relies only on passive polarization components. This property results in high stability and easy operation of the JM-OCT.

4.2.3 Polarization diversity detection

JM-OCT relies on PD detection by which two interference signals corresponding to different polarization states are independently detected. It should be noted that the two polarization states are not necessarily identical to those of the polarization delay unit. By this detection scheme, two interference signals of different polarization states are simultaneously detected by two balanced photodetectors. Each interference signal generates two OCT images at different depth positions, which correspond to the two incident polarization states multiplexed by the polarization delay unit. Finally, owing to the PD detection and the incident polarization multiplexing, four OCT images are simultaneously acquired as schematically shown in Fig. 4.2.

4.2.4 Phase calibration reflector

In this JM-OCT, the fluctuation in spectral sampling timing among OCT A-lines are monitored and canceled by using a stable spectral interference fringe denoted as a calibration signal. The generation of a calibration signal relies on the imperfection of the PBSs in the polarization delay unit. Ideally, the PBS separates S- and P-polarization components by reflecting only the S-polarization component and transmitting only the P-polarization component. However, with an off-the-shelf PBS, some portion of the P-polarization component is reflected and mixed with the S-polarization component. At the 1.06-μm wavelength, according to the manufacturer's specification, the reflected beam of the PBS employed in the passive polarization delay unit (NT49-870, Edmund Optics Inc., US) consists of 4.4% of P-polarization.

Owing to this imperfection of the PBS, the polarization delay unit behaves as a Mach-Zehnder interferometer with the OPLD of z_d for the P-polarization component, and generates the calibration signal. The calibration signal is directed to the BPDs in the PD detection unit through the 20/80 fiber coupler and a calibration reflector (box-A in Fig. 4.1).

As shown in the orange squares in Fig. 4.2, the calibration signal appears at the depth location of z_d that was exactly the axial displacement between the two depth-multiplexed

signals. This calibration signal is used for the estimation of spactral shift.

It should be noted that the imperfection of the PBS does not disturb the polarization sensitive measurement of JM-OCT. The details are discussed in Section 4.3.1.

4.2.5 Measurement protocol for the MF-OCT

For the simultaneous imaging of Doppler and PS-OCT, scanning protocol was revised from the scanning protocol of HP-OCA. And, from the clinical study with HP-OCA [56], it was known that the high-sensitive Doppler mode is clinically useful, so the scanning protocol was designed as 512 A-lines × 4 frames (for fast axis scan) × 256 B-scans (for slow axis scan). For a single cross-section, scanning of 512 A-lines were repeated 4 times, this scanning protocol is for the calculation of Doppler phase shift and improvement of SNR of Jones matrix elements. Around the region of interest, 6.0 mm × 6.0 mm area was scanned and it taken 6.6 seconds for one volume data. And the structure, vasculature, and RPE discriminable MF-OCT tomograms of each B-scan were calculated from 4 multiple frames. Probing power for retinal measurement was 1.15 mW and sensitivity was 91.05 dB for the first Jones matrix element.

A tissue structure tomogram was obtained by maximum intensity projection (MIP) of 4 Jones matrix elements. Global phase offset among 4 frames were compensated [92] and 4 frames were averaged, prior to the MIP. Vasculature tomogram, Doppler phase shift B-scan, was obtained from the phase difference between two A-lnies of successive B-scans, and complex averaging of 3 Doppler phase shift of the first Jones matrix elements were used as Doppler phase shift tomogram. RPE and exudation discriminable tomogram was obtained by calculating degree of polarization uniformity (DOPU) [47]. Detail calculation method is described in the section 4.3.

4.3 Post-Processing

4.3.1 Principle of Jones matrix OCT

Prior to the detailed processing algorithms of MF-OCT, conceptual principle of JM-OCT is described in this section. By employing two incident polarization states and PD detection, JM-OCT determines the polarization property of a sample through Jones matrix analysis [38, 93]. By denoting the Jones vector one of the incident polarization states as $\vec{E}_{in}^{(1)} = \begin{bmatrix} H_{in}^{(1)} & V_{in}^{(1)} \end{bmatrix}^T$ and the corresponding OCT signals measured by the two detectors in the PD detection unit as $E_{out\,A}^{(1)}(z)$, $E_{out\,B}^{(1)}(z)$, and $\vec{E}_{out}^{(1)}(z) \equiv \begin{bmatrix} E_{out\,A}^{(1)}(z) & E_{out\,B}^{(1)}(z) \end{bmatrix}^T$, the relationship between $\vec{E}_{in}^{(1)}$ and $\vec{E}_{out}^{(1)}(z)$ becomes

$$\vec{E}_{out}^{(1)}(z) = \chi\ \mathbf{J}_{all}(z)\ \vec{E}_{in}^{(1)} \tag{4.1}$$

where $\mathbf{J}_{all}(z)$ is the Jones matrix representing the overall polarization property from the output point of the polarization delay unit to the PD detection unit including the Jones matrix of OCT system and the depth resolved round trip Jones matrix of the sample. χ

is a general transform matrix which transforms the horizontal and vertical components of the Jones vector at the PD detection unit to the two arbitrary polarization components detected by the two detectors in the PD detection unit. Namely, χ represents the imperfection of the PD detection such as the optical unbalance in the reference power of OCT detection, the gain unbalance of photo-detectors and the cross-talk between two detectors. Similarly, the other incident polarization component and its corresponding OCT signals are related as

$$\vec{E}^{(2)}_{out}(z) = \chi\ \mathbf{J}_{all}(z)\ \vec{E}^{(2)}_{in}. \tag{4.2}$$

Note that, in the JM-OCT using polarization-delay-based multiplexing scheme, the OCT signals corresponding to $\vec{E}^{(1)}_{in}(z)$ and $\vec{E}^{(2)}_{in}(z)$ appear at two different depth. In order to avoid the confusion, we define the variable of depth z as relative depth from each zero-delay point of each incident polarization component. Namely, the same value of z represents the same depth location in the sample.

Equations (4.1) and (4.2) can be combined as

$$\mathbf{E}_{out}(z) = \chi\ \mathbf{J}_{all}(z)\ \mathbf{E}_{in} \tag{4.3}$$

where $\mathbf{E}_{in} \equiv \begin{bmatrix} H^{(1)}_{in} & H^{(2)}_{in}; & V^{(1)}_{in} & V^{(2)}_{in} \end{bmatrix}$ and $\mathbf{E}_{out}(z)$ is a matrix of measured OCT signals

$$\mathbf{E}_{out}(z) = \begin{bmatrix} E^{(1)}_{out\,A}(z) & E^{(2)}_{out\,A}(z) \\ \\ E^{(1)}_{out\,B}(z) & E^{(2)}_{out\,B}(z) \end{bmatrix}. \tag{4.4}$$

Note that, in Eq. (4.3), $\mathbf{E}_{out}(z)$ is a measured value, while $\mathbf{E}_{in}$ is predefined but not accurately known matrix.

By considering the general configuration of the JM OCT, $\mathbf{J}_{all}(z)$ can be decomposed into three components as

$$\mathbf{J}_{all}(z) = \mathbf{J}_{out}\ \mathbf{J}_s(z)\ \mathbf{J}_{in} \tag{4.5}$$

where $\mathbf{J}_{in}$ is the Jones matrix from the polarization delay unit to the sample surface, $\mathbf{J}_{out}$ is that from the sample surface to the PD detection unit and $\mathbf{J}_s(z) = \mathbf{J}'_s(z)^T\mathbf{J}'_s(z)$ is the round trip Jones matrix of the sample with that of single trip $\mathbf{J}'_s(z)$.

The purpose of the JM OCT measurement is determining polarization properties of $\mathbf{J}_s$ through its eigenvalues. To obtain the eigenvalues, a similar matrix of $\mathbf{J}_s$ is obtained by the following protocol. First, the surface of the sample is segmented and $\mathbf{E}_{out}$ at the sample is obtained as $\mathbf{E}_{out}(z_0)$ where z_0 represents the depth position of the surface. And then, a similar matrix of the $\mathbf{J}_s(z)$ at each location in the sample is obtained as

$$\begin{aligned} \mathbf{E}_{out}(z)\ \mathbf{E}_{out}(z_0)^{-1} &= \chi\ \mathbf{J}_{out}\ \mathbf{J}_s(z)\ \mathbf{J}_{in}\ \mathbf{E}_{in}\ \mathbf{E}^{-1}_{in}\ \mathbf{J}^{-1}_{in}\ \mathbf{J}^{-1}_{out}\ \chi^{-1} \\ &= \chi\ \mathbf{J}_{out}\ \mathbf{J}_s(z)\ \mathbf{J}^{-1}_{out}\ \chi^{-1} \end{aligned} \tag{4.6}$$

This equation indicates that by using two measured matrices of $\mathbf{E}_{out}(z)$ and $\mathbf{E}_{out}(z_0)$, we can define the similar matrix of the round trip Jones matrix of the sample, and hence its eigenvalues. It would be noteworthy that, JM-OCT provides this similar matrices regardless of the combination of the input polarization states except the two states are

parallel to each other [93]. Owing to this inherent robustness, the imperfection of PBS, which has been utilized to generate the calibration signal (see Section 4.2.4), does not affect to the polarization measurement.

In practical implementation, $\mathbf{E}_{out}(z_0)$ is obtained by averaging the Jones matrices at the surface of the sample within a B-scan by using adaptive Jones matrix averaging method described in Section 4.3.3. This averaging enhances the signal to noise ratio (SNR) of $\mathbf{E}_{out}(z_0)$ and provides a more reliable result.

4.3.2 Phase retardation and relative attenuation calculation

The round-trip phase retardation of the sample is obtained from the similar matrix which has been obtained through Eq. (4.6). The eigenvalues of the round round-trip sample Jones matrix can be obtained through matrix diagonalization [35] or the following equation [94]

$$\lambda_{1,2} = T/2 \pm \sqrt{T^2/4 - D} \tag{4.7}$$

where T and D are the trace and determinant of the similar matrix and $\lambda_{1,2}$ indicates two eigenvalues of the matrix. Here we have utilized the fact that the eigenvalues of the similar matrix are identical to those of the round-trip Jones matrix of the sample.

The phase retardation $\delta(z)$ is then obtained as the phase difference between two eigenvalues as

$$\delta(z) = |\mathrm{Arg}\left[\lambda_1 \lambda_2^*\right]| \tag{4.8}$$

Note that $\delta(z)$ is defined to be aliased into the range of $[0, \pi]$ because the assignment of λ_1 and λ_2 are underspecified.

In addition to the phase retardation, the relative attenuation between two characteristic polarization states $\epsilon(z)$ is obtained as

$$\epsilon(z) = \left| \ln \frac{|\lambda_1|}{|\lambda_2|} \right| \tag{4.9}$$

4.3.3 Adaptive Jones Matrix Averaging

To obtain a high quality phase retardation image, adaptive Jones matrix averaging [92] can optionally be applied to the similar Jones matrices.

This method relies on weighted least square estimation of the relative global phase of a Jones matrix in respect to an arbitrary reference Jones matrix. Consider several Jones matrices $\mathbf{M}^{(j)}$ (or similarly several of $\mathbf{E}_{out}$) are obtained in a single homogeneous birefringence domain of a sample but not within a coherence volume, i.e. the resolution of OCT. Under this condition, it would be rational to assume the following relation ship; $\mathbf{M}^{(0)} \simeq \exp\left(i\,\Delta\varphi^{(0,j)}\right)\mathbf{M}^{(j)}$. Here $\Delta\varphi^{(0,j)}$ is the relative global phase between $\mathbf{M}^{(0)}$ and $\mathbf{M}^{(j)}$. The basic concept of adaptive Jones matrix averaging is averaging $\mathbf{M}^{(j)}$ after canceling the global phase.

In the adaptive Jones matrix averaging method, the global phase between two Jones

matrix are estimated as

$$\Delta\varphi^{(0,j)} \equiv \mathrm{Arg}\left[\sum_{l=1}^{4} \frac{\exp i\left(\mathrm{Arg}\left[M_l^{(j)}/M_l^{(0)}\right]\right)}{\left|M_l^{(0)}\right|^{-1} + \left|M_l^{(j)}\right|^{-1}}\right], \tag{4.10}$$

where $M_l^{(j)}$ is the l-th entry of j-th matrix under averaging.

After determining the global phase, the averaged matrix is obtained as

$$\overline{\mathbf{M}} \equiv \sum_j \exp\left(i\,\Delta\varphi^{(0,j)}\right)\mathbf{M}^{(j)}. \tag{4.11}$$

Note that $\mathbf{M}^{(0)}$ is a reference matrix for the determination of the global phase, and hence the phase noise of this matrix should be small. In practical processing, a Jones matrix possessing highest SNR among the matrices being averaged is utilized as $\mathbf{M}^{(0)}$.

In practical JM-OCT measurement, this adaptive Jones matrix averaging is optionally applied to the similar matrices ($\mathbf{E}_{out}(z)\mathbf{E}_{out}(z_0)^{-1}$) with a averaging kernel smaller than the birefringence domain of the sample prior to calculate the eigenvalues.

4.3.4 Degree of polarization uniformity calculation

Degree of polarization uniformity (DOPU) is a parameter originally introduced by Götzinger *et al.* [47] for representing the spatial uniformity of polarization.Since some important tissues such as retinal pigment epithelium (RPE) are known to be selectively visualized by DOPU contrast, DOPU imaging by JM-OCT is of great interest.

DOPU was first defined by using Hee-Hitzenberger type PS-OCT [32], and recently applied for JM-OCT [90]. In our JM-OCT, DOPU is obtained directly from $\mathbf{E}_{out}(z)$ by following method.

Since DOPU is defined based on Stokes parameters of a back scattered light, we should define a virtual incident beam with an arbitrary state of polarization. Horizontal polarization state was empirically selected and the virtual incident polarization state was assumed as $\mathbf{E}_{out}(z_0)[1 \quad 0]^T$. The corresponding Stokes parameters are then defined as

$$\mathbf{S} = \begin{bmatrix} I \\ Q \\ U \\ V \end{bmatrix} = \begin{bmatrix} \left|E^{(1)}_{out\,A}(z)\right|^2 + \left|E^{(1)}_{out\,B}(z)\right|^2 \\ \left|E^{(1)}_{out\,A}(z)\right|^2 - \left|E^{(1)}_{out\,B}(z)\right|^2 \\ 2Re\left(E^{(1)}_{out\,A}(z)E^{(1)}_{out\,B}(z)^*\right) \\ 2Im\left(E^{(1)}_{out\,A}(z)E^{(1)}_{out\,B}(z)^*\right) \end{bmatrix} \tag{4.12}$$

Where, $Re(\ )$ and $Im(\ )$ represent real and imaginary value. Note that this Stokes parameters are only calculated from two OCT signals obtained from the PD detection unit.

DOPU is then defined as

$$\mathrm{DOPU} = \sqrt{\overline{Q}^2 + \overline{U}^2 + \overline{V}^2} \tag{4.13}$$

with

$$(\overline{Q}, \overline{U}, \overline{V}) = \left(\sum_i \frac{Q_i}{I_i}, \sum_i \frac{U_i}{I_i}, \sum_i \frac{V_i}{I_i} \right) \tag{4.14}$$

where i indicates i-th pixel within a spatial kernel by which DOPU is defined. It should be noted that this DOPU was not directly determined from the polarization property of the sample $\mathbf{J}_s(z)$, but from $\mathbf{E}_{out}(z) = \chi \mathbf{J}_{out} \mathbf{J}_s(z)$. However, it would provide a rational measure of DOPU of the sample because χ and $\mathbf{J}_{out}$ can be regarded as constant in space and time.

In MF-OCT particular implementation, a kernel size of 8 pixels (horizontal) $\times$ 3 pixels (vertical) is utilized.

4.3.5 Doppler phase shift calculation

In MF-OCT measurement protocol, the Doppler phase shift was defined as phase difference between B-scans [81], and for this purpose, a single location of a sample is scanned multiple times.

In general, a raw Doppler phase shift obtained from a living sample is expressed as

$$\Delta\phi(z) = \frac{4\pi\tau}{\lambda_c} n \nu_z(z) + \phi_b \tag{4.15}$$

where λ_c is the center wavelength, n is the refractive index of the sample, ν_z is an axial velocity of the flow of interest, and ϕ_b is a constant phase offset occurred by a bulk motion of the sample. τ is a time interval between two A-scans under Doppler calculation, and in our protocol, which is equivalent to the time interval of B-scans.

In MF-OCT, the raw Doppler phase shift $\Delta\phi(j)$ is, in principle, defined by using the coherently composite signals as

$$\Delta\phi(z, j) = \mathrm{Arg}\left[\overline{E_{out}}(z, j+1)\overline{E_{out}}(z, j)^*\right] \tag{4.16}$$

where $\Delta\phi(j)$ is the Doppler phase shift of an A-line in j-th B-scan against the corresponding A-line in $(j+1)$-th B-scan. The the bulk phase offset $\phi_b(j)$ is obtained by averaging the complex part of Eq. (4.16) as [95]

$$\phi_b(j) = \mathrm{Arg}\left[\sum_z \overline{E_{out}}(z, j+1)\overline{E_{out}}(z, j)^*\right] \tag{4.17}$$

where j denotes the index of B-scan.

In our measurement protocol, multiple (m) B-scans are obtained at the same location of a sample. By using these m B-scans and its bulk phase offsets, a sensitivity-enhanced Doppler signal is obtained as

$$\overline{\Delta\phi}(z, j) = \mathrm{Arg}\left[\sum_{j=m_0}^{m_0+m-2} \overline{E_{out}}(z, j+1)\overline{E_{out}}(z, j)^* \exp\left(-i\phi_b(j)\right) W(z, j)\right] \tag{4.18}$$

Patient ID	Sex	Age	Eye	Diagnosis
Subject-11	M	68.8	R	Wet AMD
Subject-12	M	43.9	L	Neovascular maculopathy
Subject-13	F	67.8	L	PCV
Subject-14	M	64.3	L	GA
Subject-15	M	80.7	L	PCV
Subject-16	M	58.2	R	PCV

Table 4.1: Subjects of MF-OCT clinical study. R: right, L: left, M: male, F: female, # of IVR: number of intravitreal injection of ranibizumab prior to the investigation with HP-OCA. The multiple numbers in the cell of [# of IVR] represent multiple measurements by HP-OCA after the each number of treatments.

where m_0 is the starting B-scan index of the multiple B-scans, $W(z,j)$ is an intensity mask defined as

$$W(z,j) = \begin{cases} 1 & : \quad \overline{E_{out}}(z,j+1)\overline{E_{out}}(z,j)^* > \epsilon^2 \\ 0 & : \quad otherwise \end{cases} \tag{4.19}$$

and ϵ^2 is the intensity of the noise floor of an OCT image.

For a particular case of $m = 1$, the bulk-phase-offset-free Doppler phase shift can be defined as

$$\overline{\Delta\phi}(z,j) = \mathrm{Arg}\left[\overline{E_{out}}(z,j+1)\overline{E_{out}}(z,j)^* \exp\left(-i\phi_b(j)\right) W(z,j)\right] \tag{4.20}$$

For displaying optical coherence angiography, the squared intensity of the Doppler phase shift $\left|\overline{\Delta\phi}(z,j)\right|^2$ is utilized.

4.4 Results

4.4.1 Multi-functional imaging

Figure 4.3 shows typical images of *en face* MF-OCT projection (Fig. 4.3a: OCT, Fig. 4.3b: power of Doppler, Fig. 4.3c: DOPU) and MF-OCT tomograms (Fig. 4.3d: OCT, Fig. 4.3e: power of Doppler phase, Fig. 4.3f: cumulative phase, Fig. 4.3g: DOPU) which were obtained from a normal macula of a 27-year-old Chinese male with -3.95 D myopia. 4 tomograms are extracted from the location indicated with yellow line in Figs. 4.3a–4.3c. Red arrows indicate the retinal vessels, retinal vessels appeared with hyper-scattering OCT intensity, non-zero Doppler phase, no-retardation and high DOPU value. Yellow arrow indicate RPE level, RPE is the most-bottom layer among three hyper-scattering layers (top: juction of the inner and outer segments of photoreceptor (IS/OS), middle: posterior tip of outer segment (PT), bottom: RPE) between retian and choroid. Depends on the imaging condition or sample states, it is hard to distinquish RPE with OCT image,

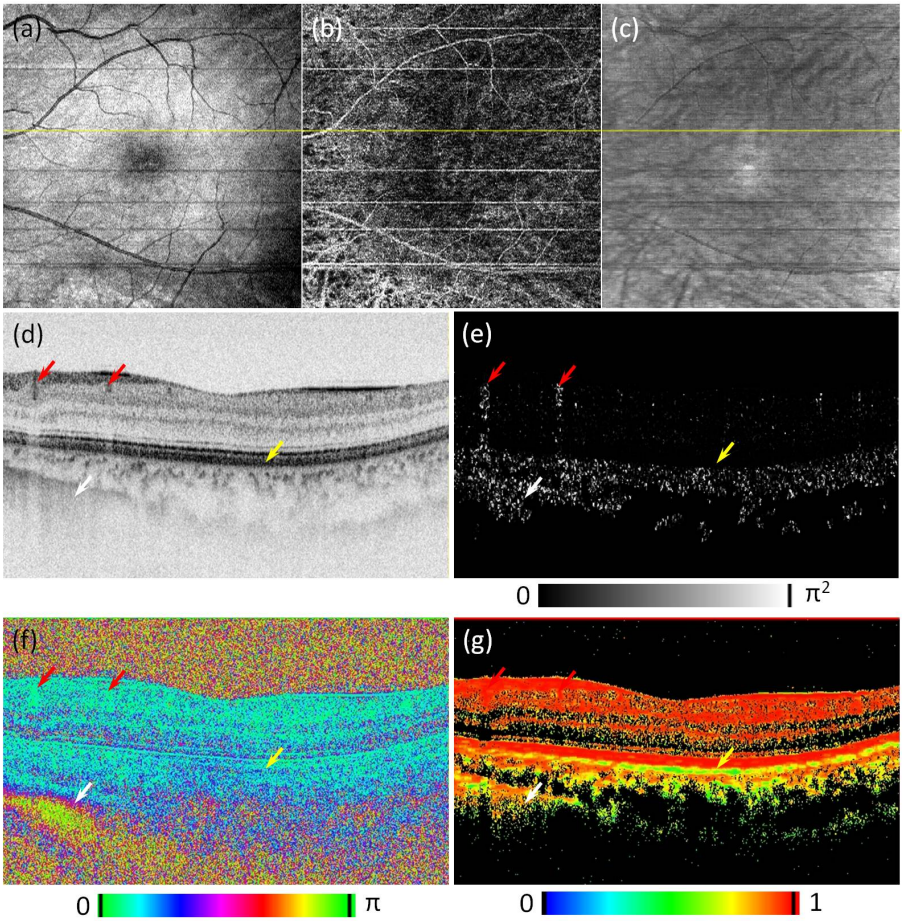

Figure 4.3: Left macular images of 27-year-old man without ocular disorder, *en face* projection images of (a) structrual OCT intensity, (b) power of Doppler phase and (c) DOPU, and cross-section images of (d) OCT, (e) power of Doppler phase, (f) cumulative phase retardation, and (g) DOPU. Yellow line in (a)–(c) indicates location of (d)–(g).

however, RPE is distinquishible with DOPU imaging as shown in Fig. 4.3g. White arrow indicate the location of choroid-sclera interference (CSI), birefreingence of sclera induce increase of phase retardation.

4.4.2 Case-7: Geographic atrophy

Figure 4.4 summarizes a case of geographic atrophy (GA). The subject was 64-year-old man (Subject-14 in Table 4.1). A circular atrophy was observed over macular region by low auto-fluorescence in fundus auto-fluorescence (FAF) (yellow dashed cirle in Fig. 4.4c), and the corresponding region was indicated with yellow dashed circles in other *en face* images. ICGA (Fig. 4.4b) shows clearer choroidal vasculature in the GA region compared with vasculature of non-GA region. Color fundus photograph(Fig. 4.4a) show bright yellow color in the GA region.

OCT *en face* projection (Fig. 4.4d) shows a similar appearance with color fundus photograph including the GA region appeared with hyper-scattering intensity. This appearance would be caused by the deep penetration into the choroid due to the RPE damage and induced lower absorption in RPE location. The deep penetration is clearly seen from the cross-section image of OCT intensity as indicated with black arrows in Fig. 4.4 g and j (Boundary of GA region is indicated with two dashed vertical lines and the corresponding reigion is indicated in other cross-section images.), and the choroid part under the GA region show more high-scattering intensity compared with non-GA region.

DOPU cross-sectional images (Figs. 4.4i and 4.4l) show high DOPU value at RPE location in GA region while the other PRE location in non-GA region show low DOPU value. This makes the DOPU *en face* projection in the RPE location (Fig. 4.4f) to appear similarly with FAF image.

Broken Bruch's membrane (BM) was observed in the GA region with low scattering intensity at the BM location as indicated with red arrow in Fig. 4.4g, at the same location abnormal Doppler signal was observed (arrow in Fig. 4.4h). and near the broken BM location, abnormal Doppler sinals were observed above BM level as indicated with arrow in Fig. 4.4k. These abnormal Doppler signals were indicated with arrow in Doppler *en face* projection image (Fig. 4.4e). ICGA image also shows the similar vasculature (arrow in Fig. 4.4b).

This subject was originally diagnosed as GA in the hospital, however from the investigation with MF-OCT abrnomal Doppler signals were observed as choroidal neovascularization (CNV). And the similar appearance of vasculatures were identified in ICGA. After the MF-OCT investigation, this case was suspected as an end-stage of wet AMD or a secondary GA from wet AMD.

4.4.3 Case-8: Wet AMD with CNV

Figure 4.5 introduces a case of wet AMD investigated with MF-OCT. The subject was 69-year-old man (Subject-11 in Table 4.1). CNV was observed from mid-phase of ICGA image as indicated with arrow in Fig. 4.5b, and the CNV was surrounded by dark-rim. Late-phase of FA image (Fig. 4.5c) shows the leakage at the CNV location, it can be known

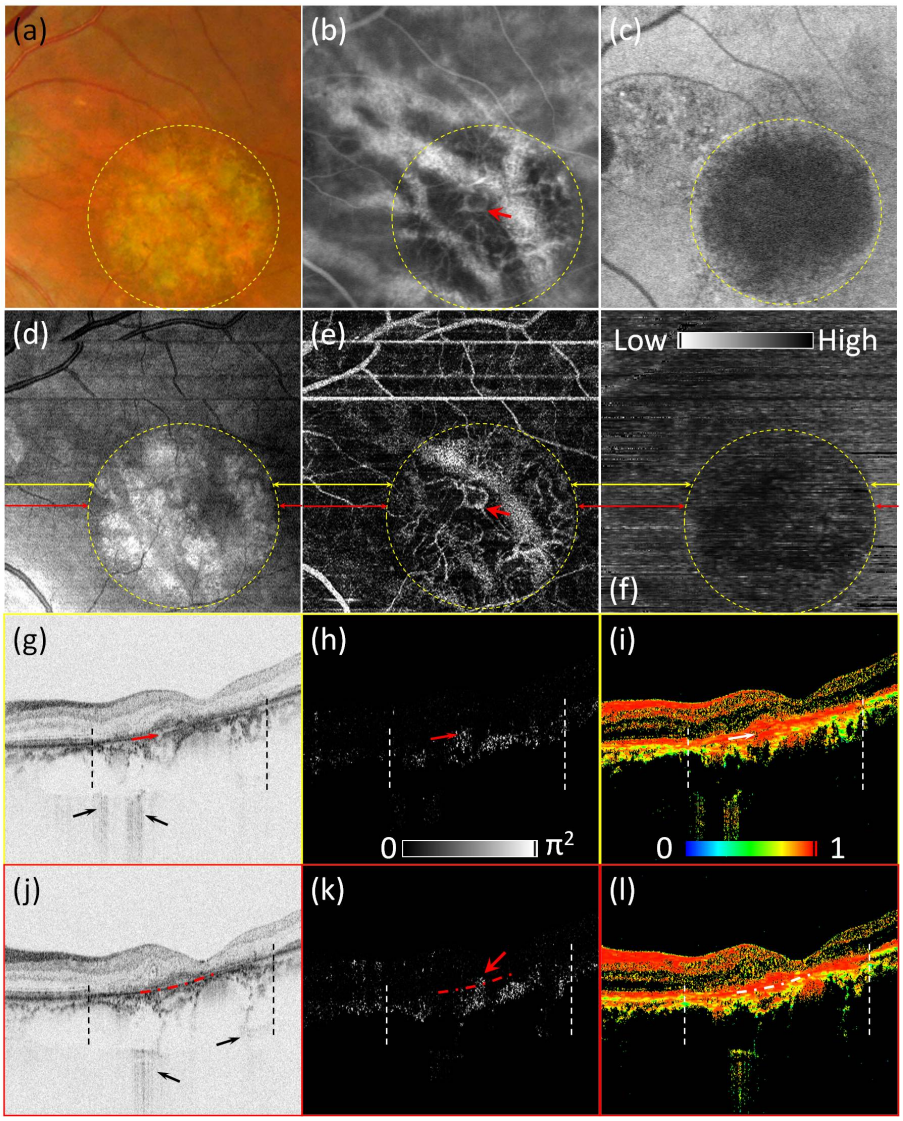

Figure 4.4: Left macular images of 64-year-old man with GA, (a) Color fundus photography, (b) ICGA (mid-phase), (c) fundus auto-fluorescence, *en face* projection images of (d) structrual OCT intensity, (e) power of Doppler phase and (f) DOPU (DOPU was projected in RPE region), and cross-section images of (g),(j) OCT, (h),(k) power of Doppler phase and (i),(l) DOPU. Yellow and red arrows pairs in (d)–(f) indicate locations of (g)–(i) and (j)–(l), respectively.

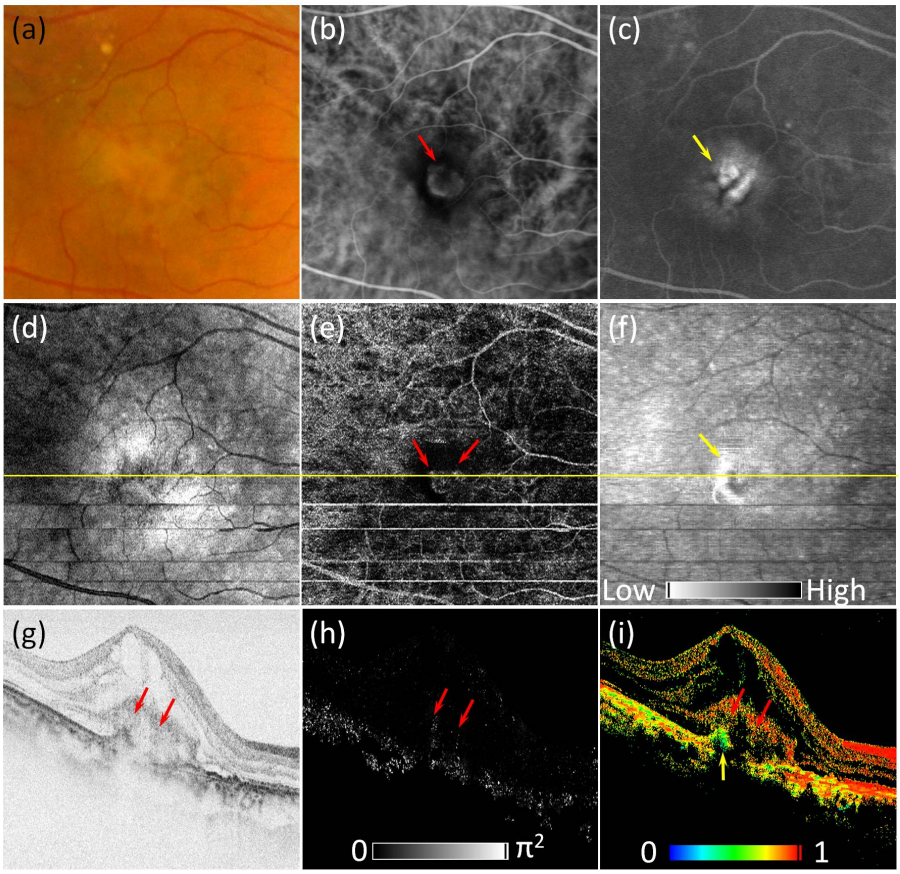

Figure 4.5: Right macular images of 69-year-old man with wet AMD, (a) Color fundus photography, (b) indocyanine angiography (mid-phase), (c) fluorescence angiography (late-phase), *en face* projection images of (d) OCT intensity, (e) power of Doppler phase and (f) DOPU, and cross-sectional images of (g) OCT, (h) power of Doppler phase and (i) DOPU. Yellow lines in (d)-(f) indicate locations of (g)–(i), respectively.

that the CNV is in active state. And color fundus photograph (Fig. 4.5a) show moderate bright appearance around CNV location.

OCT intensity *en face* projection (Fig. 4.5d) shows similar pattern with olor fundus photograph at the CNV location, however the appearance is slightly different. OCT *en face* projection image show low-scattering intensity at the CNV location while color fundus shows bright appearance.

En face Doppler projection (Fig. 4.5e) shows similar appearance with ICGA including the CNV. Abnormal Doppler signals were observed at the CNV location and surrounded by hypo-Doppler signals as indicated with two red arrows in Fig. 4.5e. the The cross-sectional image of Power Doppler (Fig. 4.5h) shows the depth location of the abnormal Doppler signal as indicated with two red arrows in Figs. 4.5h and 4.5g, Doppler signals are were observed at the exudation and connected with choroid. Beneath of the exudation, RPE deformation was observed as indicated with yellow arrow in DOPU B-scan image (Fig. 4.5i). This RPE deformation was appeared with crescent shape in DOPU *en face* projection (Fig. 4.5f) with low DOPU value around CNV location. This RPE deformation corresponded to the leakage location of FA ((arrow in Fig. 4.5c).

4.4.4 Case-9: PCV with polypoidal CNV and RPE damage

Figure 4.6 introduces a case of PCV investigated with MF-OCT. The subject was 58-year-old man (Subject-15 in Table 4.1). Hemorrhage with large crescent shape was observed in color fundus photography(Fig. 4.6a), late-phase of FA (Fig. 4.6c) and FAF image(Fig. 4.6f) inferior side of pigment epithelium detachment (PED) with dark appearance. Mid-phase of ICGA (Fig. 4.6b) shows PED with hypo-fluorescence and polypoidal CNV was observed in the peripheral region of PED and leakage was observed at the location of the polypoidal CNV in the late-phase of FA (Fig. 4.6c) as indicated by red arrow in each figure.

OCT *en face* projection of this case does not show the similar crescent shape of hemorrhage as color fundus images. However, OCT *en face* projection shows well delineated boundary of PED with hyper-scattering signal, this is related with highly elevated PED and its stiff angled RPE of PED as shown in OCT cross-sections (Figs. 4.6g and 4.6j). Doppler *en face* projection (Fig. 4.6e) shows abnormal Doppler signal at the location of polypoidal CNV as indicated by arrows. (The Doppler signals inside of yellow dashed circle in Fig. 4.6e are artifacts, they are induced by unwanted specular reflection on lens surface during the scanning.) Two cross-sections (Figs. 4.6g, 4.6h, and4.6i - yellow line framed and Figs. 4.6j, 4.6k, and 4.6l - red line framed) were extracted from polypoidal CNV location. In the yellow line framed cross-sections, Doppler signals were observed beneath the PED and RPE appeared with low DOPU value over entire region include PED. In the red line framed cross-section also shows abnormal Doppler signals beneath PED and the RPE above the abnoral Doppler signals appeared with high DOPU value as indicated with circle in Fig. 4.6l. This location is well matched with the location of RPE damage in FAF (arrow in Fig. 4.6f).

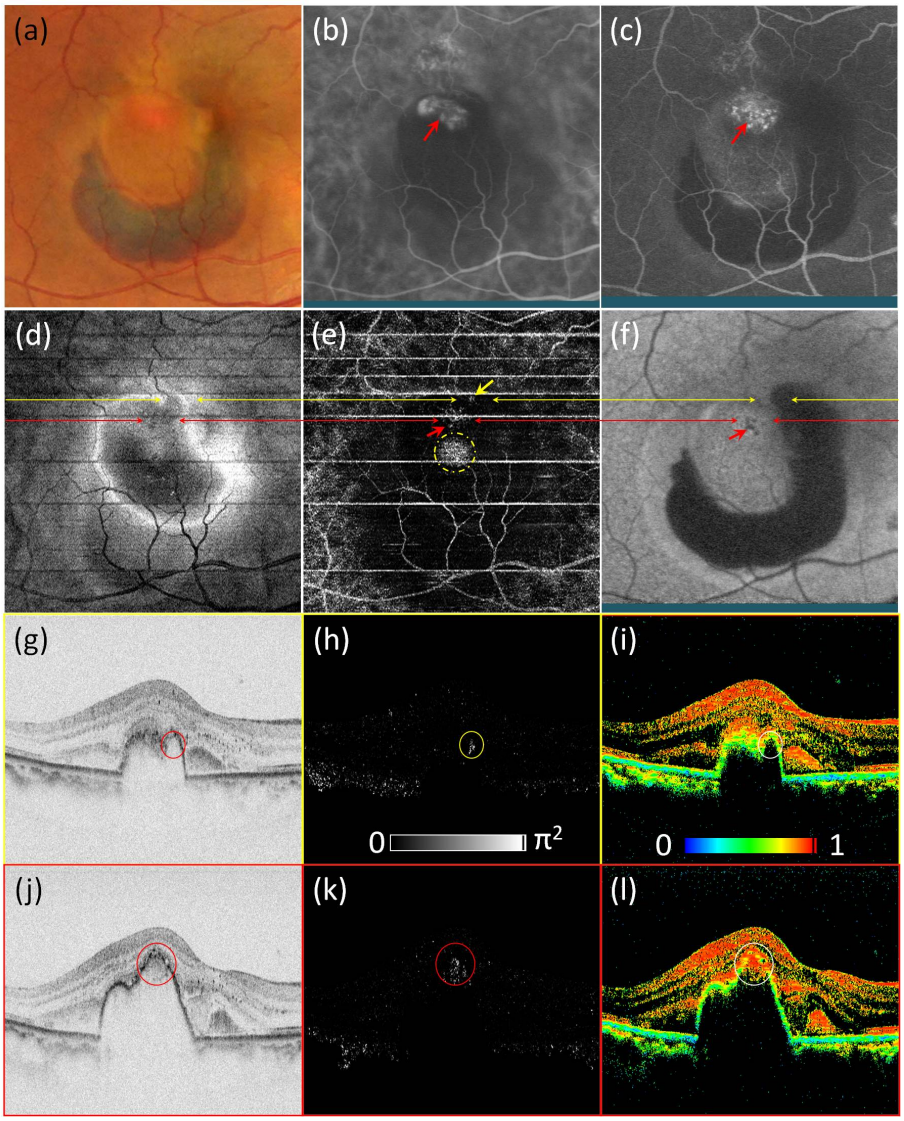

Figure 4.6: Right macular images of 58-year-old man with PCV, (a) Color fundus photography, (b) indocyanine angiography (mid-phase), (c) fluorescence angiography (late-phase), and (f) fundus auto-fluorescence (FAF), *en face* projection images of (d) OCT intensity and (e) power of Doppler phase, and cross-sectional images of (g) OCT, (h) power of Doppler phase and (i) DOPU. Yellow and red arrows pairs in (d)–(f) indicate locations of (g)–(i) and (j)–(l), respectively.

4.5 Discussion

4.5.1 Effect of practical factors in JM-OCT measurement

In this discussion, the fundamental robustness of the JM-OCT method is present. As discussed in Section 4.3.1, the relationship between incident and output light in an ideal JM-OCT is described by Eq. (4.3).

In a practical system, several additional factors should be considered. By accounting for these factors and by substituting $\mathbf{J}_{all}(z) = \mathbf{J}_{out}\mathbf{J}_s(z)\mathbf{J}_{in}$, Eq. (4.3) is modified to

$$\mathbf{E}_{out}(z) = \eta\, \mathbf{X}'\, \mathbf{R}\, \rho\, \mathbf{J}_{out}\, \mathbf{J}_s(z)\, \mathbf{J}_{in}\, \mathbf{X}\; f\,(\mathbf{X}\, \mathbf{E}_{in}\;) \tag{4.21}$$

where $\mathbf{X}$ is a matrix representing the imperfection of the PBS in the polarization delay unit. Because it is used to generate the calibration signal, there is a significant amount of polarization cross-talk in the PBS. The off-diagonal entries of $\mathbf{X}$ account for the cross-talk and the diagonal entries represent the transmittance and reflectance of the horizontally and vertically polarized light. $f(\,)$ is a function which represents the delay between two incident polarization states generated by the polarization delay unit. $\mathbf{R}$ represents interference with the reference beams and is $\mathbf{R} = \begin{bmatrix} H^*_{ref} & 0; & 0 & V^*_{ref} \end{bmatrix}$ where H^*_{ref} and V^*_{ref} are the complex conjugates of the field amplitudes of the reference beam with horizontal and vertical polarization states. ρ is a rotation matrix representing the relative rotation between the polarization delay unit and the PD detection unit. $\mathbf{X}'$ represents the imperfection of the PBS in the PD detection unit, similar to that of the polarization delay unit $\mathbf{X}$. Finally, η represents the detection efficiency of the two BPDs in the polarization delay unit as $\eta = [\eta_A \;\; 0; \;\; 0 \;\; \eta_B]$, where η_A and η_B are the detection efficiencies of the two BPDs.

Although $\mathbf{E}_{out}(z)$ is affected, these practical factors do not affect the phase retardation measurement. In JM-OCT, a similar matrix of $\mathbf{J}_s(z)$ is obtained by Eq. (4.6). By substituting Eq. (4.21) for Eq. (4.6), we found

$$\mathbf{E}_{out}(z)\mathbf{E}_{out}(z_0)^{-1} = \eta\, \mathbf{X}'\, \mathbf{R}\, \rho\, \mathbf{J}_{out}\, \mathbf{J}_s(z)\, \mathbf{J}^{-1}_{out}\, \rho^{-1}\, \mathbf{R}^{-1}\, \mathbf{X}'^{-1}\, \eta^{-1}. \tag{4.22}$$

It is evident that the right-hand side of this equation retains its similarity to $\mathbf{J}_s(z)$. Hence all the practical factors discussed in this section do not significantly affect the JM-OCT measurement.

4.5.2 DOPU and input polarization states

As described in Section 4.3.4, DOPU values were calculated from the the Stokes parameters of back scattered light, and the input polarization state was virtually emulated as horizontal polarization state. Because, the non-modulated input polarization state was horizontal state and it has relatively higher SNR than delayed vertical polarization state. Fig. 4.7 shows 6 DOPU images which were obtained by different input polarization states, Figs. 4.7a-4.7f are DOPU images obtained from inputs of horizontal, vertical, +45°, -45°, left-hand circular and right-hand circular polarization states, respectively. Location of RPE in 6 DOPU images commonly appeared with low DOPU values compared with other tissue region, however contrast of RPE to the other tissue is different depends on the input

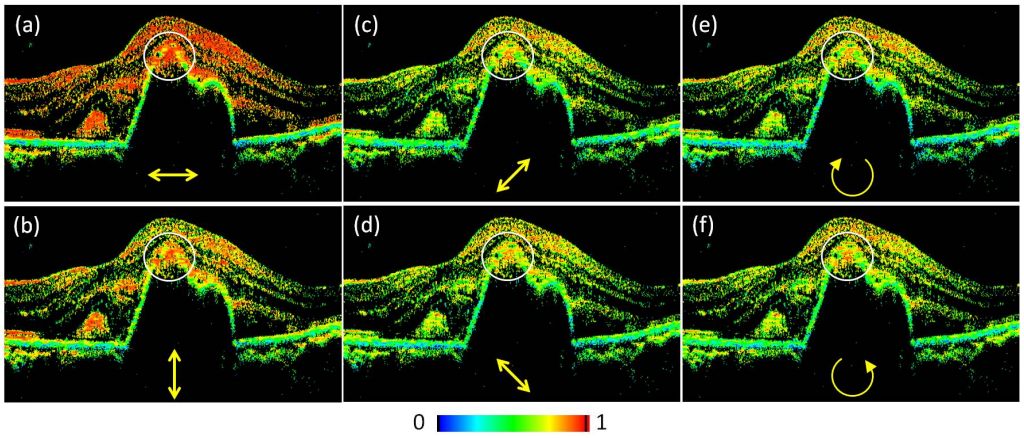

Figure 4.7: DOPU imaging according to the input polarization states. (a) horizontal polarization state, (b) vertical polarization state, (c) +45 ° polarization state, (d) -45 ° polarization state, (e) left-hand circular polarization state, and (f) right-hand circular polarization state. Double yellow arrow in each figure represnts input polarization state.

polarization states, among them, DOPU of horizontal polarization state input shows better contrast than other input state cases. The effect of different contrast is clearly obseved in the pathologic region as indicated with white circles in Fig. 4.7. Fig. 4.7a clearly shows the abnormal RPE at the peak of PED.

4.6 Summary

The development of MF-OCT based on JM-OCT extended the investigation of HP-OCA to the simultaneous Doppler and polarization properties imaging. MF-OCT demonstrated structure, vasculature, exudation and RPE discriminable imaging. Among 6 cases clinical investigation with MF-OCT, clear abnormal Doppler signals were observed from 5 cases at pathologic region and the location was well correlated with CNV location in ICGA. Abnormal RPEs were observed from 6 cases at patholgic region and the location was corresponding to the low auto-fluorescence of FAF.

Chapter 5

Conclusions

5.1 Clinical utility of HP-OCA

While FA and ICGA use fluorescent dye as a vessel contrast agent, HP-OCA uses blood flow as a contrast source. The different vessel contrast mechanism between conventional angiography and HP-OCA would result in different characteristics. FA and ICGA have advantages of time elapse imaging after dye injection and investigation of tissue damage through dye leakage. Conversely, OCA has the two major advantages of three-dimensional investigation and non-invasiveness. The three-dimensional visualization of the ocular vasculature would provide more detailed insight of the pathology. The non-invasiveness enables safe and frequent application of OCA to the patient. Therefore, OCA can be utilized not only for a specific clinical diagnosis but also for mass-screening.

5.2 Clinical utility of MF-OCA

MF-OCA demonstrated structure, vasculature, exudation and RPE discriminable imaging. RPE and hard exudates commonly have polarization scrambling property, and appeared with hyper-scattering in OCT intensity and non-zero Doppler phase value. Currently, the discrimination of RPE and hard exudates is done subjectively according to the difference in morphological location. Similar vasculature patter between Doppler *en face* images and ICGA was observed as HP-OCA. Abnormal RPE cells were observed at patholgic region and the location was corresponding to the low auto-fluorescence of FAF.

5.3 Summary

HP-OCA was developed for an alternative non-invasive angiographic modality. Ophthalmic clinical utility was investigated with 10 cases of exudative macular diseases, and it was found that the HP-OCA is able to be utilized as a supplementary angiographic modality. MF-OCA, functional extension of HP-OCA for the polarization sensitive imaging, was demonstrated and simultaneous vasculature and RPE imaging is available. Preliminary

clinical study was done with 6 cases, and clinical utility of MF-OCA is also expected as a comprehensive ophthalmic imaging modality.

Bibliography

Bibliography

[1] L. A. Yannuzzi, *The Retinal Atlas* (Elsevier, 2010), 1st ed.

[2] Y. Ikuno and Y. Tano, "Retinal and choroidal biometry in highly myopic eyes with spectral-domain optical coherence tomography," Investigative Ophthalmology & Visual Science **50**, 3876–3880 (2009).

[3] Y. Ikuno, Y. Jo, T. Hamasaki, and Y. Tano, "Ocular risk factors for choroidal neovascularization in pathologic myopia," Investigative Ophthalmology & Visual Science **51**, 3721–3725 (2010).

[4] N. M. Bressler, S. B. Bressler, and S. L. Fine, "Age-related macular degeneration," Survey of Ophthalmology **32**, 375 – 413 (1988).

[5] AREDS, "Risk factors associated with age-related macular degeneration: A case-control study in the age-related eye disease study: age-related eye disease study report number 3," Ophthalmology **107**, 2224 – 2232 (2000).

[6] J. D. M. Gass, "Biomicroscopic and histopathological consideratios regarding the feasibility of surgical excision of subfoveal neovascular membranes," Transactions of the American Ophthalmological Society **92**, 91–1116 (1994).

[7] L. A. Yannuzzi, D. W. K. Wong, B. S. Sforzolini, M. Goldbaum, K. C. Tang, R. F. Spaide, K. B. Freund, J. S. Slakter, D. R. Guyer, J. A. Sorenson, Y. Fisher, D. Maberley, and D. A. Orlock, "Polypoidal choroidal vasculopathy and neovascularized age-related macular degeneration," Arch Ophthalmol **117**, 1503–1510 (1999).

[8] A. Tsujikawa, M. Sasahara, A. Otani, N. Gotoh, T. Kameda, D. Iwama, Y. Yodoi, H. Tamura, M. Mandai, and N. Yoshimura, "Pigment epithelial detachment in polypoidal choroidal vasculopathy." Am. J. Ophthalmol. **143**, 102–111 (2007).

[9] V. Patel, S. Rassam, R. Newsom, J. Wiek, and E. Kohner, "Retinal blood flow in diabetic retinopathy." Br. Med. J. **305**, 678–683 (1992).

[10] E. Friedman, "A hemodynamic model of the pathogenesis of age-related macular degeneration." Am. J. Ophthalmol. **124**, 677–682 (1997).

[11] J. Flammer, S. Orgl, V. P. Costa, N. Orzalesi, G. K. Krieglstein, L. M. Serra, J.-P. Renard, and E. Stefnsson, "The impact of ocular blood flow in glaucoma," Progress in Retinal and Eye Research **21**, 359 – 393 (2002).

[12] J. D. M. Gass, *Stereoscopic atlas of macular diseases : diagnosis and treatment* (Mosby, 1997).

[13] L. Yannuzzi, K. Rohrer, L. Tindel, R. Sobel, M. Costanza, W. Shields, and E. Zang, "Fluorescein angiography complication survey," Ophthalmology **93**, 611–617 (1986).

[14] K. Kwiterovich, M. Maguire, R. Murphy, A. Schachat, N. Bressler, S. Bressler, and S. Fine, "Frequency of adverse systemic reactions after fluorescein angiography. results of a prospective study," Ophthalmology **98**, 1139–1142 (1991).

[15] M. Hope-Ross, L. A. Yannuzzi, E. S. Gragoudas, D. R. Guyer, J. S. Slakter, J. A. Sorenson, S. Krupsky, D. A. Orlock, and C. A. Puliafito, "Adverse reactions due to indocyanine green," Ophthalmology **101**, 529–533 (1994).

[16] O. Strauss, "The retinal pigment epithelium in visual function," Physiological Reviews **85**, 845–881 (2005).

[17] S. SCHMITZ-VALCKENBERG, F. G. HOLZ, A. C. BIRD, and R. F. SPAIDE, "Fundus autofluorescence imaging: Review and perspectives," RETINA **28**, 385–409 (2008).

[18] L. Querques, G. Querques, R. Forte, and E. H. Souied, "Microperimetric correlations of autofluorescence and optical coherence tomography imaging in dry age-related macular degeneration," American Journal of Ophthalmology **153**, 1110 – 1115 (2012).

[19] D. Huang, E. Swanson, C. Lin, J. Schuman, W. Stinson, W. Chang, M. Hee, T. Flotte, K. Gregory, C. Puliafito, and a. et, "Optical coherence tomography," Science **254**, 1178–1181 (1991).

[20] A. F. Fercher, W. Drexler, C. K. Hitzenberger, and T. Lasser, "Optical coherence tomography - principles and applications," Reports on Progress in Physics **66**, 239 (2003).

[21] W. Drexler and J. G. Fujimoto, *Optical Coherence Tomography: Technology and Applications* (Springer Berlin / Heidelberg, 2008).

[22] A. F. Fercher, C. K. Hitzenberger, G. Kamp, and S. Y. El-Zaiat, "Measurement of intraocular distances by backscattering spectral interferometry," Optics Communications **117**, 43 – 48 (1995).

[23] G. Hausler and M. W. Lindner, ""Coherence radar" and "spectral radar" —new tools for dermatological diagnosis," J. Biomed. Opt. **3**, 21–31 (1998).

[24] J. A. Izatt, M. D. Kulkarni, S. Yazdanfar, J. K. Barton, and A. J. Welch, "In vivo bidirectional color doppler flow imaging of picoliter blood volumes using optical coherence tomography," Opt. Lett. **22**, 1439–1441 (1997).

[25] Y. Zhao, Z. Chen, C. Saxer, S. Xiang, J. F. de Boer, and J. S. Nelson, "Phase-resolved optical coherence tomography and optical doppler tomography for imaging blood flow in human skin with fast scanning speed and high velocity sensitivity," Opt. Lett. **25**, 114–116 (2000).

[26] R. A. Leitgeb, C. K. Hitzenberger, A. F. Fercher, and T. Bajraszewski, "Phase-shifting algorithm to achieve high-speed long-depth-range probing by frequency-domain optical coherence tomography," Opt. Lett. **28**, 2201–2203 (2003).

[27] R. A. Leitgeb, L. Schmetterer, W. Drexler, A. F. Fercher, R. J. Zawadzki, and T. Bajraszewski, "Real-time assessment of retinal blood flow with ultrafast acquisition by color doppler fourier domain optical coherence tomography," Opt. Express **11**, 3116–3121 (2003).

[28] B. White, M. Pierce, N. Nassif, B. Cense, B. Park, G. Tearney, B. Bouma, T. Chen, and J. de Boer, "In vivo dynamic human retinal blood flow imaging using ultra-high-speed spectral domain optical coherence tomography," Opt. Express **11**, 3490–3497 (2003).

[29] Y. Zhao, Z. Chen, C. Saxer, Q. Shen, S. Xiang, J. F. de Boer, and J. S. Nelson, "Doppler standard deviation imaging for clinical monitoring of in vivo human skin blood flow," Opt. Lett. **25**, 1358–1360 (2000).

[30] D. Y. Kim, J. Fingler, J. S. Werner, D. M. Schwartz, S. E. Fraser, and R. J. Zawadzki, "In vivo volumetric imaging of human retinal circulation with phase-variance optical coherence tomography." Biomed Opt Express **2**, 1504–1513 (2011).

[31] M. Szkulmowski, A. Szkulmowska, T. Bajraszewski, A. Kowalczyk, and M. Wojtkowski, "Flow velocity estimation using joint spectral and time domain optical coherence tomography," Opt. Express **16**, 6008–6025 (2008).

[32] M. R. Hee, D. Huang, E. A. Swanson, and J. G. Fujimoto, "Polarization-sensitive low-coherence reflectometer for birefringence characterization and ranging," J. Opt. Soc. Am. B **9**, 903–908 (1992).

[33] J. F. de Boer, T. E. Milner, M. J. C. van Gemert, and J. S. Nelson, "Two-dimensional birefringence imaging in biological tissue by polarization-sensitive optical coherence tomography," Opt. Lett. **22**, 934–936 (1997).

[34] Y. Yasuno, S. Makita, Y. Sutoh, M. Itoh, and T. Yatagai, "Birefringence imaging of human skin by polarization-sensitive spectral interferometric optical coherence tomography," Opt. Lett. **27**, 1803–1805 (2002).

[35] M. Yamanari, S. Makita, V. D. Madjarova, T. Yatagai, and Y. Yasuno, "Fiber-based polarization-sensitive fourier domain optical coherence tomography using b-scan-oriented polarization modulation method," Opt. Express **14**, 6502–6515 (2006).

[36] M. Yamanari, S. Makita, and Y. Yasuno, "Polarization-sensitive swept-source optical coherence tomography with continuous source polarization modulation," Opt. Express **16**, 5892–5906 (2008).

[37] S. Jiao and L. V. Wang, "Two-dimensional depth-resolved mueller matrix of biological tissue measured with double-beam polarization-sensitive optical coherence tomography," Opt. Lett. **27**, 101–103 (2002).

[38] B. H. Park, M. C. Pierce, B. Cense, and J. F. de Boer, "Jones matrix analysis for a polarization-sensitive optical coherencetomography system using fiber-optic components," Opt. Lett. **29**, 2512–2514 (2004).

[39] J. Zhang, S. Guo, W. Jung, J. Nelson, and Z. Chen, "Determination of birefringence and absolute optic axis orientation using polarization-sensitive optical coherence tomography with pm fibers," Opt. Express **11**, 3262–3270 (2003).

[40] C. Hitzenberger, E. Goetzinger, M. Sticker, M. Pircher, and A. Fercher, "Measurement and imaging of birefringence and optic axis orientation by phase resolved polarization sensitive optical coherence tomography," Opt. Express **9**, 780–790 (2001).

[41] M. Pircher, E. Götzinger, R. Leitgeb, H. Sattmann, O. Findl, and C. Hitzenberger, "Imaging of polarization properties of human retina in vivo with phase resolved transversal ps-oct," Opt. Express **12**, 5940–5951 (2004).

[42] E. Götzinger, M. Pircher, and C. K. Hitzenberger, "High speed spectral domain polarization sensitive optical coherence tomography of the human retina," Opt. Express **13**, 10217–10229 (2005).

[43] M. Miura, M. Yamanari, T. Iwasaki, A. E. Elsner, S. Makita, T. Yatagai, and Y. Yasuno, "Imaging polarimetry in age-related macular degeneration," Investigative Ophthalmology & Visual Science **49**, 2661–2667 (2008).

[44] Y. Yasuno, M. Yamanari, K. Kawana, T. Oshika, and M. Miura, "Investigation of post-glaucoma-surgery structures by three-dimensional and polarization sensitive anterior eye segment optical coherence tomography," Opt. Express **17**, 3980–3996 (2009).

[45] E. Götzinger, M. Pircher, B. Baumann, C. Ahlers, W. Geitzenauer, U. Schmidt-Erfurth, and C. K. Hitzenberger, "Three-dimensional polarization sensitive oct imaging and interactive display of the human retina," Opt. Express **17**, 4151–4165 (2009).

[46] M. Pircher, E. Gtzinger, O. Findl, S. Michels, W. Geitzenauer, C. Leydolt, U. Schmidt-Erfurth, and C. K. Hitzenberger, "Human macula investigated in vivo with polarization-sensitive optical coherence tomography," Investigative Ophthalmology & Visual Science **47**, 5487–5494 (2006).

[47] E. Götzinger, M. Pircher, W. Geitzenauer, C. Ahlers, B. Baumann, S. Michels, U. Schmidt-Erfurth, and C. K. Hitzenberger, "Retinal pigment epithelium segmentation bypolarization sensitive optical coherencetomography," Opt. Express **16**, 16410–16422 (2008).

[48] B. Cense, T. C. Chen, B. H. Park, M. C. Pierce, and J. F. de Boer, "Invivo depth-resolved birefringence measurements of the human retinal nerve fiber layer by polarization-sensitive optical coherence tomography," Opt. Lett. **27**, 1610–1612 (2002).

[49] M. Mujat, B. H. Park, B. Cense, T. C. Chen, and J. F. de Boer, "Autocalibration of spectral-domain optical coherence tomography spectrometers for in vivo quantitative retinal nerve fiber layer birefringence determination," Journal of Biomedical Optics **12**, 041205 (2007).

[50] M. Yamanari, M. Miura, S. Makita, T. Yatagai, and Y. Yasuno, "Phase retardation measurement of retinal nerve fiber layer by polarization-sensitive spectral-domain optical coherence tomography and scanning laser polarimetry," Journal of Biomedical Optics **13**, 014013 (2008).

[51] A. Unterhuber, B. Považay, B. Hermann, H. Sattmann, A. Chavez-Pirson, and W. Drexler, "In vivo retinal optical coherence tomography at 1040 nm - enhanced penetration into the choroid," Opt. Express **13**, 3252–3258 (2005).

[52] S. H. Yun, G. Tearney, J. de Boer, and B. Bouma, "Motion artifacts in optical coherence tomography with frequency-domain ranging," Opt. Express **12**, 2977–2998 (2004).

[53] B. Potsaid, B. Baumann, D. Huang, S. Barry, A. E. Cable, J. S. Schuman, J. S. Duker, and J. G. Fujimoto, "Ultrahigh speed 1050nm swept source / fourier domain oct retinal and anterior segment imaging at 100,000 to 400,000 axial scans per second," Opt. Express **18**, 20029–20048 (2010).

[54] W. Wieser, B. R. Biedermann, T. Klein, C. M. Eigenwillig, and R. Huber, "Multi-megahertz oct: High quality 3d imaging at 20 million a-scans and 4.5 gvoxels per second," Opt. Express **18**, 14685–14704 (2010).

[55] Y.-J. Hong, S. Makita, F. Jaillon, M. J. Ju, E. J. Min, B. H. Lee, M. Itoh, M. Miura, and Y. Yasunore, "High-penetration swept source doppler optical coherence angiography by fully numerical phase stabilization," Opt. Express **20**, 2740–2760 (2012).

[56] Y.-J. Hong, M. Miura, S. Makita, M. J. Ju, B. H. Lee, T. Iwasaki, and Y. Yasuno, "Noninvasive investigation of deep vascular pathologies of exudative macular diseases by high-penetration optical coherence angiography," Investigative Ophthalmology & Visual Science **54**, 3621–3631 (2013).

[57] Y. Lim, Y.-J. Hong, L. Duan, M. Yamanari, and Y. Yasuno, "Passive component based multifunctional jones matrix swept source optical coherence tomography for doppler and polarization imaging," Opt. Lett. **37**, 1958–1960 (2012).

[58] X. J. Wang, T. E. Milner, and J. S. Nelson, "Characterization of fluid flow velocity by optical doppler tomography," Opt. Lett. **20**, 1337–1339 (1995).

[59] Z. Chen, T. E. Milner, D. Dave, and J. S. Nelson, "Optical doppler tomographic imaging of fluid flow velocity in highly scattering media," Opt. Lett. **22**, 64–66 (1997).

[60] M. Wojtkowski, R. Leitgeb, A. Kowalczyk, T. Bajraszewski, and A. F. Fercher, "In vivo human retinal imaging by fourier domain optical coherence tomography," J. Biomed. Opt. **7**, 457–463 (2002).

[61] N. A. Nassif, B. Cense, B. H. Park, M. C. Pierce, S. H. Yun, B. E. Bouma, G. J. Tearney, T. C., Chen, and J. F. de Boer, "*In vivo* high-resolution video-rate spectral-domain optical coherence tomography of the human retina and optic nerve," Opt. Express **12**, 367–376 (2004).

[62] R. A. Leitgeb, L. Schmetterer, C. K. Hitzenberger, A. F. Fercher, F. Berisha, M. Wojtkowski, and T. Bajraszewski, "Real-time measurement of in vitro flow by fourier-domain color doppler optical coherence tomography." Opt. Lett. **29**, 171–173 (2004).

[63] S. Makita, Y. Hong, M. Yamanari, T. Yatagai, and Y. Yasuno, "Optical coherence angiography," Opt. Express **14**, 7821–7840 (2006).

[64] Y. Imamura, T. Fujiwara, R. Margolis, and R. F. Spaide, "Enhanced depth imaging optical coherence tomography of the choroid in central serous chorioretinopathy," Retina **29**, 1469–1473 (2009).

[65] U. Chakravarthy, J. Evans, and P. J. Rosenfeld, "Age related macular degeneration," BMJ **340** (2010).

[66] D. M. de Bruin, D. L. Burnes, J. Loewenstein, Y. Chen, S. Chang, T. C. Chen, D. D. Esmaili, and J. F. de Boer, "In vivo three-dimensional imaging of neovascular age-related macular degeneration using optical frequency domain imaging at 1050 nm," Invest. Ophthalmol. Vis. Sci. **49**, 4545–4552 (2008).

[67] Y. Yasuno, Y. Hong, S. Makita, M. Yamanari, M. Akiba, M. Miura, and T. Yatagai, "In vivo high-contrast imaging of deep posterior eye by 1-um swept source optical coherence tomography andscattering optical coherence angiography," Opt. Express **15**, 6121–6139 (2007).

[68] B. Povazay, B. Hermann, B. Hofer, V. Kaji, E. Simpson, T. Bridgford, and W. Drexler, "Wide-field optical coherence tomography of the choroid in vivo." Invest. Ophthalmol. Vis. Sci. **50**, 1856–1863 (2009).

[69] V. J. Srinivasan, D. C. Adler, Y. Chen, I. Gorczynska, R. Huber, J. S. Duker, J. S. Schuman, and J. G. Fujimoto, "Ultrahigh-speed optical coherence tomography for three-dimensional and en face imaging of the retina and optic nerve head," Invest. Ophthalmol. Vis. Sci. **49**, 5103–5110 (2008).

[70] Y. Yasuno, M. Miura, K. Kawana, S. Makita, M. Sato, F. Okamoto, M. Yamanari, T. Iwasaki, T. Yatagai, and T. Oshika, "Visualization of sub-retinal pigment epithelium morphologies of exudative macular diseases by high-penetration optical coherence tomography," Invest. Ophthalmol. Vis. Sci. **50**, 405–413 (2009).

[71] T. Klein, W. Wieser, C. M. Eigenwillig, B. R. Biedermann, and R. Huber, "Megahertz oct for ultrawide-field retinal imaging with a 1050nm fourier domain mode-locked laser," Opt. Express **19**, 3044–3062 (2011).

[72] B. Vakoc, S. Yun, J. de Boer, G. Tearney, and B. Bouma, "Phase-resolved optical frequency domain imaging," Opt. Express **13**, 5483–5493 (2005).

[73] J. Zhang and Z. Chen, "In vivo blood flow imaging by a swept laser source based fourier domain optical doppler tomography," Opt. Express **13**, 7449–7457 (2005).

[74] B. Baumann, B. Potsaid, M. F. Kraus, J. J. Liu, D. Huang, J. Hornegger, A. E. Cable, J. S. Duker, and J. G. Fujimoto, "Total retinal blood flow measurement with ultrahigh speed swept source/fourier domain oct," Biomed. Opt. Express **2**, 1539–1552 (2011).

[75] B. Braaf, K. A. Vermeer, V. A. D. Sicam, E. van Zeeburg, J. C. van Meurs, and J. F. de Boer, "Phase-stabilized optical frequency domain imaging at 1- μm for the measurement of blood flow in the human choroid," Opt. Express **19**, 20886–20903 (2011).

[76] A. N. S. Institute and L. I. of America, *American National Standard for safe use of lasers* (The Institute, Orlando, FL, 2000).

[77] S. Moon, S.-W. Lee, and Z. Chen, "Reference spectrum extraction and fixed-pattern noise removal in optical coherence tomography," Opt. Express **18**, 24395–24404 (2010).

[78] C. Kasai, K. Namekawa, A. Koyano, and R. Omoto, "Real-time two-dimensional blood flow imaging using an autocorrelation technique," Sonics and Ultrasonics, IEEE Transactions on **32**, 458 – 464 (1985).

[79] V. X. D. Yang, M. L. Gordon, A. Mok, Y. Zhao, Z. Chen, R. S. C. Cobbold, B. C. Wilson, and I. A. Vitkin, "Improved phase-resolved optical doppler tomography using the kasai velocity estimator and histogram segmentation," Optics Communications **208**, 209 – 214 (2002).

[80] B. Park, M. C. Pierce, B. Cense, S.-H. Yun, M. Mujat, G. Tearney, B. Bouma, and J. de Boer, "Real-time fiber-based multi-functional spectral-domain optical coherence tomography at 1.3 μm," Opt. Express **13**, 3931–3944 (2005).

[81] B. J. Vakoc, R. M. Lanning, J. A. Tyrrell, T. P. Padera, L. A. Bartlett, T. Stylianopoulos, L. L. Munn, G. J. Tearney, D. Fukumura, R. K. Jain, and B. E. Bouma, "Three-dimensional microscopy of the tumor microenvironment in vivo using optical frequency domain imaging," Nat. Med. **15**, 1219–1223 (2009).

[82] M. Miura, S. Makita, T. Iwasaki, and Y. Yasuno, "Three-dimensional visualization of ocular vascular pathology by optical coherence angiography in vivo," Investigative Ophthalmology & Visual Science **52**, 2689–2695 (2011).

[83] L. Feeney, "Lipofuscin and melanin of human retinal pigment epithelium. fluorescence, enzyme cytochemical, and ultrastructural studies." Investigative Ophthalmology & Visual Science **17**, 583–600 (1978).

[84] L. Feeney-Burns, E. S. Hilderbrand, and S. Eldridge, "Aging human rpe: morphometric analysis of macular, equatorial, and peripheral cells." Investigative Ophthalmology & Visual Science **25**, 195–200 (1984).

[85] C. Ahlers, E. Gtzinger, M. Pircher, I. Golbaz, F. Prager, C. Schtze, B. Baumann, C. K. Hitzenberger, and U. Schmidt-Erfurth, "Imaging of the retinal pigment epithelium in age-related macular degeneration using polarization-sensitive optical coherence tomography," Investigative Ophthalmology & Visual Science **51**, 2149–2157 (2010).

[86] B. Baumann, E. Gtzinger, M. Pircher, H. Sattmann, C. Schtze, F. Schlanitz, C. Ahlers, U. Schmidt-Erfurth, and C. K. Hitzenberger, "Segmentation and quantification of retinal lesions in age-related macular degeneration using polarization-sensitive optical coherence tomography." J Biomed Opt. **15**, 061704 (2010).

[87] B. Baumann, S. O. Baumann, T. Konegger, M. Pircher, E. Götzinger, F. Schlanitz, C. Schütze, H. Sattmann, M. Litschauer, U. Schmidt-Erfurth, and C. K. Hitzenberger, "Polarization sensitive optical coherence tomography of melanin provides intrinsic contrast based on depolarization," Biomed. Opt. Express **3**, 1670–1683 (2012).

[88] S. Jiao, W. Yu, G. Stoica, and L. Wang, "Optical-fiber-based mueller optical coherence tomography," Opt. Lett. **28**, 1206–1208 (2003).

[89] K. H. Kim, B. H. Park, Y. Tu, T. Hasan, B. Lee, J. Li, and J. F. de Boer, "Polarization-sensitive optical frequency domain imaging based on unpolarized light," Opt. Express **19**, 552–561 (2011).

[90] B. Baumann, W. Choi, B. Potsaid, D. Huang, J. S. Duker, and J. G. Fujimoto, "Swept source / fourier domain polarization sensitive optical coherence tomography with a passive polarization delay unit," Opt. Express **20**, 10229–10241 (2012).

[91] Y. Yasuno, V. D. Madjarova, S. Makita, M. Akiba, A. Morosawa, C. Chong, T. Sakai, K.-P. Chan, M. Itoh, and T. Yatagai, "Three-dimensional and high-speed swept-source optical coherence tomography for in vivo investigation of human anterior eye segments," Opt. Express **13**, 10652–10664 (2005).

[92] Y. Lim, M. Yamanari, S. Fukuda, Y. Kaji, T. Kiuchi, M. Miura, T. Oshika, and Y. Yasuno, "Birefringence measurement of cornea and anterior segment by office-based polarization-sensitive optical coherence tomography," Biomed. Opt. Express **2**, 2392–2402 (2011).

[93] S. Makita, M. Yamanari, and Y. Yasuno, "Generalized jones matrix optical coherence tomography: performance and local birefringence imaging," Opt. Express **18**, 854–876 (2010).

[94] M. Yamanari, S. Makita, Y. Lim, and Y. Yasuno, "Full-range polarization-sensitiveswept-source optical coherencetomography by simultaneous transversaland spectral modulation," Opt. Express **18**, 13964–13980 (2010).

[95] K. Kurokawa, K. Sasaki, S. Makita, Y.-J. Hong, and Y. Yasuno, "Three-dimensional retinal and choroidal capillary imaging by power doppler optical coherence angiography with adaptive optics," Opt. Express **20**, 22796–22812 (2012).